Université des Sciences et Technologies de Lille

Université de Wuhan

Laboratoire de Mécanique de Lille (UMR CNRS 8107)

Année : 2010 N° d'ordre :

THESE DE DOCTORAT

Pour obtenir le grade de

Docteur de L'Université des Sciences et Technologies de Lille

Discipline: Génie Civil

Présentée par

XUE Luanluan

Le 13 avril 2010

Element composite pour un couplage écoulement/contrainte dans les roches fracturées

Seepage and Stress Coupling Algorithm of Fractured Rock Mass by Composite Element Method

Jury :

Professeur SHAHROUR Isam, Université de Lille 1, Directeur de Thèse

Professeur CHEN Shenhong, Wuhan University, Directeur de Thèse

Professeur Ali ZAOUI, Université Lille1, Président

Professeur ROUAINIA Mohamed, University of Newcastle, Rapporteur
Professeur WU Aiqing, Yangtze River Research Institute, Rapporteur

Professeur LU Wenbo, Wuhan University

Examinateur Directeur de Thèse

Directeur de Thèse

Table of Content

Résumé

Le travail de thèse porte sur l'analyse du couplage écoulement – contrainte dans les roches fracturées et son application aux barrages. Le rapport de thèse est composé de 5 chapitres.

Le premier chapitre présente une synthèse des travaux réalisés sur les roches fracturées et plus particulièrement sur le couplage écoulement – contrainte. L'accent est mis sur la modélisation numérique.

Le second chapitre concerne la formulation de l'Élément Composite pour les roches fracturées. Il présente cet élément pour le problème mécanique ensuite pour le problème d'écoulement.

Le 3ème chapitre présente l'extension de l'Elément Composite aux roches fracturées en prenant en compte le couplage contrainte – écoulement. Après une présentation de la formulation mathématique, on décrit l'introduction de cet élément dans un code de calcul. Le chapitre décrit aussi le fonctionnement de cet élément pour une fracture soumise à une contrainte normale puis à un cisaillement.

Le 4ème chapitre traite de l'application de l'Elément Composite aux masses de roches fracturées contenant des drains. La performance de l'Elément Composite pour ce type d'applications est montrée à travers sa confrontation à la méthode des éléments finis classique.

Le dernier chapitre présente l'application de l'Elément Composite à l'analyse du barrage de Xiaowan ayant un système de fondation complexe. La fondation contient trois ensembles de fractures et des drains. Cet exemple montre les performances de l'Elément Composite pour l'analyse des projets à géomètrie complexe contenant des fractures.

Abstract

There is an important and complicated coupling between seepage and stress fields in the fractured rock mass. On the one hand, the stress field is influenced by the seepage load; on the other hand, the stress field affects the permeability characteristics and in turn the seepage field as well. Due to the West-East electricity transmission project and South-North water transmission project (the west line), the construction of the hydraulic and electricity engineering has been shifted to the high canyon area in the west in China, where the active tectonic movement, atrocious weather, well developed fractures, and high geostress are found playing important roles. Therefore, the control of rock seepage、deformation and stability mainly depends on the analysis level of seepage and stress coupling for fractured rock mass. European and American scholars also work hard on the seepage and stress coupling for fractured rock mass in order for the problems of nuclear waste deposit, deep oil exploitation, deep long tunnel and so on.

So far, there have been some accomplished researches on the seepage and stress coupling for fractured rock mass, mainly including experimental technology, hydraulic parameters, numerical models, numerical algorithm, and so on. However, there are still some difficulties to be overcome, such as how to actually and conveniently simulate the complicated configuration (fractures, drainage holes, bolts, etc.) with simplified preprocess work, how to consider the coupling mechanism for fractured rock mass as actual as possible, how to take the flow exchange between fracture and adjacent rock block into account, how to deal with the problem of fractured rock mass containing drainage holes, and so on.

As for the problems mentioned above, a composite element algorithm on the seepage and normal stress coupling for fractured rock mass firstly has been proposed in this dissertation. Then the coupling mechanism for fractured rock mass during the shear process has been established, as well as the coupling algorithm on the seepage and stress for fractured rock mass containing drainage holes. Finally the proposed algorithms have been taken into application to the Xiaowan arch dam foundation system with complicated configuration. The main work in this dissertation can be briefly summarized as follows:

At first, based on the composite element method (CEM), the seepage and normal stress coupling algorithm of fractured rock mass by the CEM has been presented, which is an important extension of CEM. The rock fractures are assumed as a filled medium, and it enables to treat the rock fractures with or without fillings in a unified way. The coupling mechanism has been carried out through iteration algorithm between the seepage and stress field, and the flow exchange between the fracture and adjacent rock block has been taken into consideration. The FORTRAN programs have been compiled for the proposed algorithm. And finally the proposed algorithm has been verified by one simple numerical example. The computation results have been compared to the conventional finite element method (FEM), where the advantages and reliability of the proposed algorithm have been well shown, and the obtained seepage velocities along the fracture are much closer to the actual ones than those obtained by the FEM.

Next, considering the different levels of normal stresses, the relationship between shear stress and shear deformation of rock fracture has been established. This relationship can be divided into three phases: shear shrink, shear dilation up to peak value, and residual shear strength. Then, based on the CEM, the seepage and stress coupling algorithm of fractured rock mass during shearing has been carried out, by which the variation and relationship among the shear deformation, fracture aperture, conductivity of rock fracture, seepage field as well as stress field are illustrated. Finally the numerical example indicates that, with the constant mechanical parameters of filled medium in the fracture, the seepage velocity of fracture remain stable with variable shear deformation and normal stress, but if the fracture aperture changes, the flow rate per unit width through the fracture will change accordingly.

And then, the CEM is formulated for the seepage and stress coupling algorithm of fractured rock mass containing drainage holes. Each fracture or drainage hole segment is considered as a special sub-element with definite seepage and deformation characteristics, which is located explicitly within the composite element. According to the variational principle the governing equation for the composite element containing both fractures and

drainage holes is established and implemented in the software. Based on the CEM developed in this dissertation, the fractures and drainage holes can be simulated explicitly but do not participate in the computation domain discrete, in this way the generation of the computation mesh is not restricted strongly by the position and the orientation of the fractures and drainage holes, which is of significance in the optimal design of seepage control system. If there are no fractures and drainage holes, the CEM will automatically be degenerated to the FEM. The coupling mechanism on the seepage and stress for fractured rock mass containing drainage holes has been carried out through the iteration algorithm between the seepage and stress field. The FORTRAN programs also have been compiled for the proposed algorithm. And finally the validity and reliability of the proposed algorithm have been verified by the numerical examples. The application and comparative study for the Baozhusi dam foundation have been presented also.

Finally, the proposed coupling algorithms based on the CEM have been taken into application to Xiaowan arch dam foundation system with complicated configuration, and their advantages and reliability of the proposed algorithms have been further proved. The proposed algorithms can be applied conveniently in the complicated engineering with simplified mesh generation preprocess, and the obtained seepage velocities through the fracture and drainage holes are much closer to the actual ones than those by the FEM. The uneven hydraulic behavior of the fractured rock mass resulting from the stress is remarkable when considering the seepage and stress coupling, and the importance of the coupling analysis has been further emphasized for fracture rock mass or fractured rock mass containing drainage holes.

The innovation of this dissertation can be briefly summarized as follows: Based on the CEM, the seepage and normal stress coupling algorithm of fractured rock mass has been proposed, which takes the flow exchange between the fracture and adjacent rock block into account, and can be used for both filled and unfilled fracture; The composite element algorithm on the seepage and stress coupling for fractured rock mass during the shear process has been established, and the shear process has been divided into three

phases, starting from the shear shrink phase, then into the shear dilation phase until the peak value phase, and ending with the residual shear strength phase; The seepage and stress coupling algorithm of fractured rock mass containing drainage holes has also been proposed by the CEM, where each fracture or drainage holes is considered as a special sub-element with definite seepage and deformation characteristics, and embedded explicitly into the composite element; The FORTRAN programs have been compiled for all the proposed algorithms; And finally all the proposed coupling algorithms have been taken into application to Xiaowan arch dam foundation system with complicated configuration, where the advantages and reliability of the coupling algorithms have been shown obviously.

Keywords: fractured rock mass; seepage; stress; coupling; drainage hole; composite element method

Chapter 1 Literature review

1.1 Introduction

There are many kinds of actions in the rock mass engineering, such as hydraulics, mechanics, thermal, chemical, etc, which influence and interact with each other, and it is called coupling effect. While the coupling effect between hydraulics and mechanics plays an important role in the underground cavern, ultra high slope, hydropower and unclear waste deposit projects, the coupling effect on the seepage and stress for fractured rock mass is especially important and remarkable (Tsang, 1990; Geng,1994; Wu, Zhang,1995; Zhang, 2005).

Until 1960s, the permeability characteristics of fractured rock mass were not clearly understood, and the coupling effect between the seepage and stress field for the fractured rock mass is ignored in the engineering design, which leads to some fatal and world shaking engineering accidents (P_{OMM}, 1966; Geng,1994; Zhang, 2005).

Malpasset arch dam is located on the Reyran Valley in the south of France. In December 1959, after a few days when it was up to the normal water level, the arch dam was broken suddenly, which killed hundreds of people (Jaeger,1979; Londe, 1987; Wittke, Leonards, 1987). The left part of the dam foundation was moved downstream, and some dam blocks swept 1.5 km away, with only the right part of the dam foundation remained, (see Fig.1.1). This is the first record and typical destruction of arch dam. The main reason for the accident is that, the left part of the dam foundation slid along the fault F1 by too large water pressure in the foundation fractured rock mass(Jaeger,1979; Wittke, Leonards, 1987; Ru, Jiang, 1995; Zhang, 2005).

The fractures are well developed in the Malpasset dam foundation, with dip angle of 30°～50°, inclined towards to the downstream. There are also two important fractures in the dam foundation, one is fracture F1 directs almost EW, with dip angle 45° inclining towards upstream; another on is fracture F2 directs almost SN, with dip angle 70°～80° inclining towards the left bank, as shown in the Fig.1.2(a). Based on the theory of incremental seepage load for rock mass(Wittke, Leonards, 1987; Zhang, 2005), the fractures around the dam heel have been opened by the big water thrust, and then the water flows into the fractures, which makes the fractures further split until to the fracture F1. Therefore, there is almost full water head on the fractures with huge water thrust, which results in the instability of foundation rock block between left abutment and fracture F1, further more, the instability of the whole arch dam, see the Fig.1.2(b).

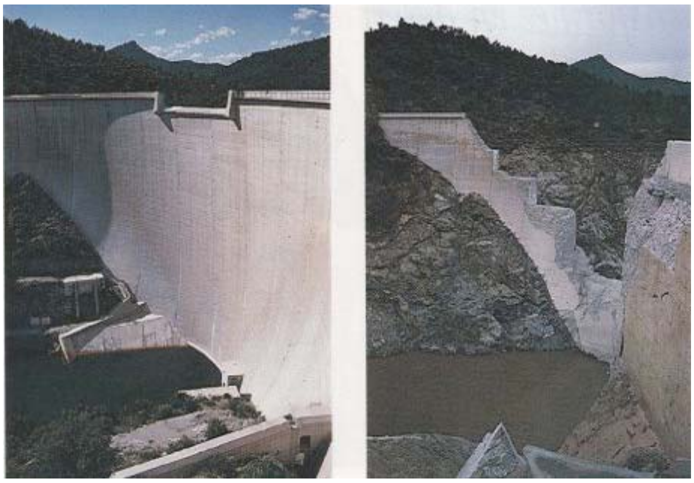

Fig.1.1 Contrast of Malpasset dam before and after the destruction
(http://en.structurae.de/structures/data/index.cfm?ID=s0000335)

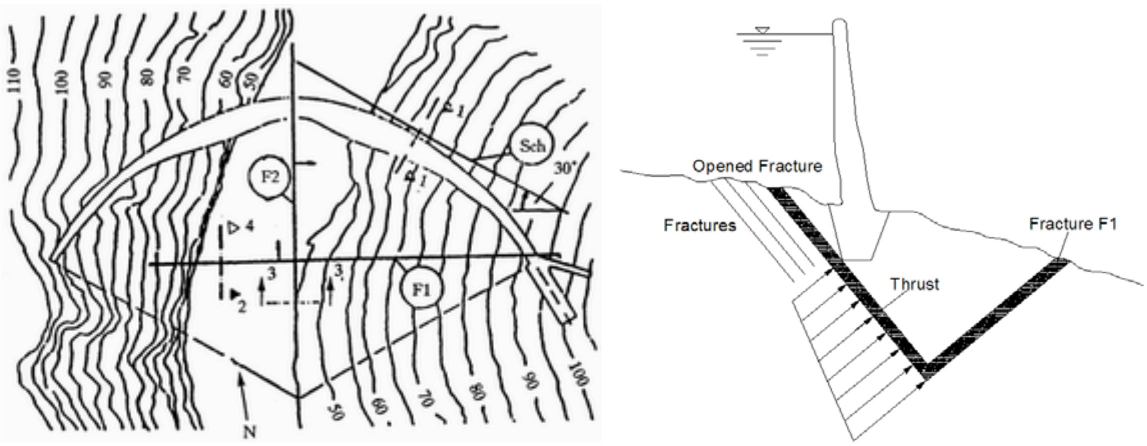

(a)geological layout of dam (b)Sketch for destroyed analysis

Fig.1.2 Main data for Malpasset arch dam (Wittke, Leonards, 1987)

Vajont arch dam is located on the Vajont river, the branch of Piave river in Italy. In 1963, the high-speed landslide at upstream left bank made the reservoir water get across the dam, flow into the downstream, which led to a great loss. Whereas the destruction experience on Malpasset arch dam, the left and right abutments have been reinforced before, and the arch dam remained stable with the great overloads, but the slide rock blocks have filled the whole reservoir, making the dam and reservoir been discarded. The main reason is that, after the rain, the fractures in the left and right banks are well developed, which makes the hydraulic potential of upstream slope increase synchronously as the increase of that of reservoir. When the hydraulic potential of reservoir increases, the volumetric weight of upstream slope changes from wet one to float one, and the slide resistance force decreases, the slide displacement tends to increase, even causing the slide (Jaeger, 1979; Hendron, Patton, 1985; Ru, Jiang, 1995; Zhang, 2005), see the Fig.1.3.

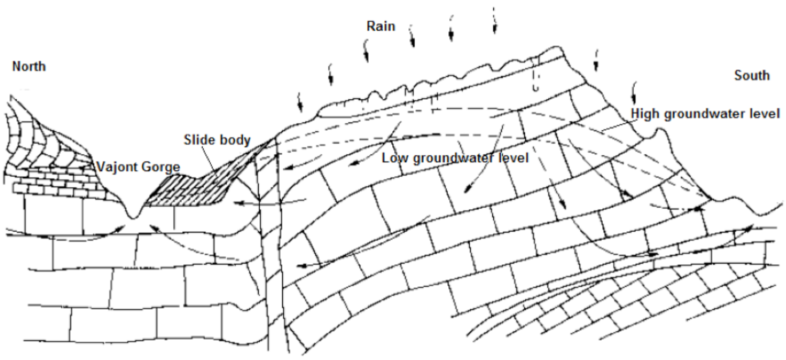

Fig.1.3 The influence of rain on the slope (Hendron, Patten, 1985)

Teton dam is located in the Teton river in Idaho, it is an earth-rock dam with core. In 1976, there were leakage hole and groove erosion at the bank dam section, leading to the damage of the dam(Chadwick, 1976; Zhang, 2005). The hydraulic potential of reservoir increased rapidly due to the rain, and the water flew into the well developed fractures in the right slope, which has brought about the further open behavior of fractures. Then there was almost full water head in the cogging, and the cogging had been split by the high water pressure, making the fractures extend to the downstream one, which caused the piping erosion (Chadwick, 1976; Seed, Duncan, 1987; Zhang, 2005).

The three serious accidents mentioned above bring about the naissance of rock hydraulics. Snow(1968) and Louis(1974) have taken the lead in the research on the rock hydraulics, and paid more attention to the permeability mechanism of fractured rock mass. After that, there are many more researchers working on the rock hydraulics, especially for the fractured rock mass.

In China, due to the West-East electricity transmission project and South-North water transmission project (the west line), the construction of the hydraulic and electricity engineering has shifted to the high canyon area in the west, and many great engineering projects have begun. And they have brought about a lot of rock hydraulics problems, especially the analysis of seepage、deformation and stability for the structures of extra-high abutment slide resistance block and slope, deep large span underground building, and deep long tunnel, and so on. Because there are active tectonic movement, atrocious weather, well developed fractures, and high geostress in the west in China, the control of rock seepage、deformation and stability strongly depends on the analysis level of seepage and stress coupling for fractured rock mass.

There is an important and complicated interaction between the seepage and stress field in the fractured rock mass: on the one hand, the stress field influences the permeability characteristics of fractured rock mass; on the other hand, the changed seepage loads lead to the change of the stress field. Since 1970s, some researchers have begun working hard on the seepage and stress coupling for fractured rock mass in the European and United States. Nowadays, it is still a hot topic, especially on the nuclear waste deposit, deep oil exploitation, deep long tunnel and so on(Wang, 1991). In China, the research on the seepage and stress coupling for fractured rock mass has begun since 1980s (Zhang, Zhang, 1982; Tian, 1984), and the research mainly depends on the projects of hydraulic electricity, mining, oil exploitation, tunnels and so on. The topic on the seepage and stress coupling for fractured rock mass is one critical problem in the rock hydraulics research. But due to its complexity, there is still much room for improvement of the efficiency and convenience of the practical engineering project.

1.2 Recent researches of fractured rock mass

Liquid is one of the most essential characteristics for fractured rock mass medium, the static and dynamic water pressures in the porous and fracture medium can change the whole stress field, sometimes they can influence the safety and stability of structures, even cause the destruction, for example, slope instability, arch dam collapse, hydraulic-induced earthquake, and so on. On the other hand, the changed stress field can lead to the change of fracture aperture, which brings the change of hydraulic conductivity, as well as the change of the whole seepage field.

The researches on the seepage and stress coupling for fractured rock mass mainly include experimental technology, numerical models, numerical algorithms, hydraulic parameters, etc. The research on the numerical models is the most important “bridge” between basic theory and engineering application, and it is always the hottest and most active topic. While concerning the numerical models, the study on the seepage and stress coupling for single fracture is the key topic.

1.2.1 Seepage and stress coupling analysis for single fracture

Due to the influence of the environment, rock fracture has very complicated geometric characteristics, and it is one important medium in the fractured rock mass, fracture deformation not only dominates the whole deformation of fractured rock mass, but also governs the whole seepage field of fractured rock mass. Concerning on the deformation characteristics and simulation for rock fracture, Goodman(1968) has proposed joint model without thickness, Zienkiewicz(1966), Desai(1976) have proposed joint model with thickness, and these two models are the well known and typical models for the single fracture, and also can be well applied in the practical engineering. Concerning on the permeability characteristics and simulation of rock fracture, Snow(1969) has proposed the parallel plate model, Louis(1970), Tsang, Witherspoon,(1981), Barton(1985) have improved and modified that model, which have been accepted widely at present.

There are also many scholars studying hard on the coupling relationship between normal stress and tangential seepage through the fracture, such as Snow(1969), Gale(1982), Barton, Bandis(1985), Raven, Gale(1985), Liu(1987,1988), Tao, Shen(1988), Chen, Wang, Xiong(1989), Chen, Zhang(1994), Wu, Zhang(1995), Su, Zhan, Wang(1997), Wang, Xu, Su(1998), Zhang, Zhang(1997), Liu, Chen, Fu(2002), Wang(2002), Chang, Zhao, Hu, etc.(2004), and all of them have taken further research and proposed some good numerical models.

There are a few researches on the coupling relationship between shear stress and tangential seepage through the fracture, but much more still need to be done to improve it. Teufel(1987) has found that the hydraulic conductivity coefficient of fracture decreases as the increase of shear deformation through the experiments; but Esaki (1992, 1999) has found that the normal displacement of fracture increases as the increase of shear deformation through the experiments, see the Fig1.4. Geng(1994) has made the similar experiments, and it is found that: at the beginning, when the shear displacement of fracture is very small, fracture aperture and hydraulic conductivity coefficient decrease as the increase of shear displacement, subsequently, as the increase of shear displacement, fracture aperture and hydraulic conductivity coefficient increase obviously, because of the shear dilation, see the Fig.1.5. Liu, Chen, Fu(2002) has made experiments for single fracture with sand during the shear process, and it is found that, the fracture aperture increases as the increase of shear displacement. But at the beginning of shear process, the seepage flow decreases as the increase of shear displacement, afterwards, it increases as the increase of shear displacement. There are also some other experiments and simulations done to the seepage and stress coupling during the shear process, such as Gale(1990), Makurat et al.(1990), Olsson, Brown(1993), Iwano, Einstein (1995), Yeo, De, Zimmerman(1998), Esaki et al.(1999), Chen, et al.(2000), Guvanasen, Chan (2000), Lee, Cho (2002), Mitani et al. (2003), Koyama, et al.(2006), Li, et al.(2007), Matsuki, et al.(2009), and so on.

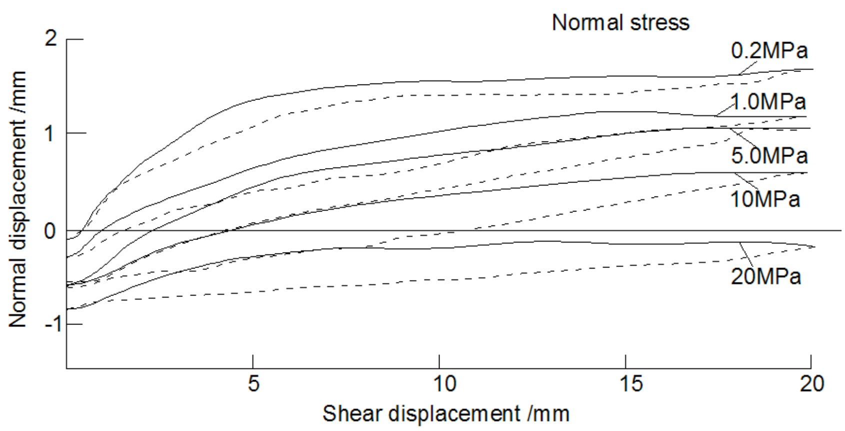

Fig.1.4 Relationship between shear and normal displacement (Esaki, 1992,1999)

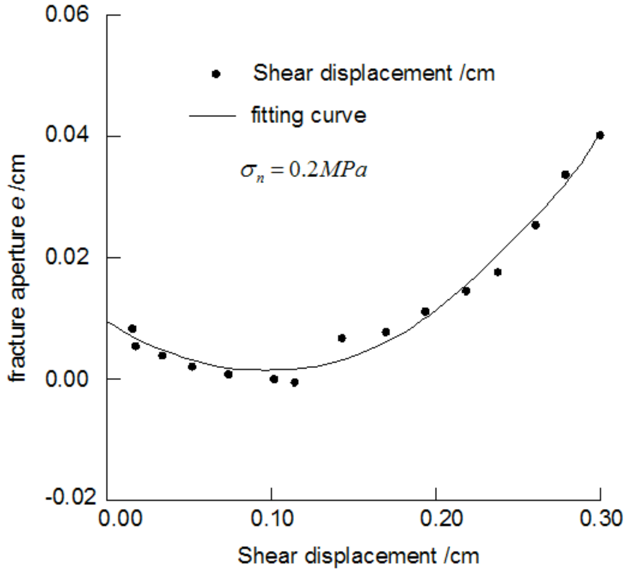

Fig.1.5 Relationship between shear and normal displacement (Geng, 1994)

In studying the numerical simulation of flow exchange among the rock porous, rock fracture, and rock block system, one of the most important and critical steps is, how to build the coupling relationship among normal deformation, shear deformation, and normal seepage flow along the fracture. However, there have been not sufficient researches done in these aspects yet.

1.2.2 Seepage and stress coupling model for fractured rock mass

So far, the numerical models on the seepage and stress coupling for fractured rock mass can be classified into three categories: equivalent continuum model, fracture network model, and fracture and porous media model.

The equivalent continuum model takes the fractured rock mass as one homogenous medium for its simplicity and convenience in the engineering. The deformation and permeability characteristics of rock fractures are taken into consideration in the equivalent continuum model, but the exact position and direction of fractures are neglected. Generally, the equivalent continuum model is only well used for some specific conditions, that is: the REV (Representative Element Volume) of the research region exists, which is much smaller than the dimension of the research region, and the time influence is not taken into consideration in the research.

The fracture network model is also called discrete fracture model, in which only the fracture deformation is taken into consideration, and water only flows along the fracture network, but the deformation and permeability characteristics of rock blocks are neglected. At present, the generation technology for fracture network has been well developed, and there are also some researches on the seepage and stress coupling for 2-D fracture network. For 3-D complicated fracture network, the research is only focus on the steady seepage (Dershowitz, Einstein, 1987; Mao, etc., 1991; Wang, Yang, 1992; Bai, Elsworth, 1994; Geng, etc., 1996; Feng, Chen, 2006), and the study on the seepage and stress coupling for 3-D complicated fracture network needs to be developed.

The fracture and porous media model is also called dual media model (Barenblatt, etc. 1960; Duiguid, Lee, 1977; Zimmerman, etc. 1996; Wu, 1996, 1998), which takes the flow exchange between fracture and porous into consideration, and is a more realistic numerical model. Generally, when the fracture network is distributed sparsely, and the seepage field is changed as the change of time, this model should be adopted. But when the fracture network is distributed a little complicatedly, the application is very difficult to carry out, and the flow exchange rule between the fracture and porous media is also very difficult to confirm.

In all these three models, only the flow along the fracture and porous media is taken into consideration, while the flow exchange among the fracture, porous and the adjacent rock blocks is neglected, which may cause a serious problem about flow exchange in the study of rock hydraulics.

1.2.3 Numerical model for drainage holes

The preprocess of exact numerical simulation for drainage holes is very important in the study of seepage field, usually it governs the whole seepage field, and plays an important role in designing the seepage control system. There are several numerical models for drainage holes, such as drainage hole replaced by point model, abandoned element model, boundary element model, equivalent bar element model, drainage substructure model, and so on.

The drainage hole replaced by point model can be used very conveniently with simplifying the drainage holes, but it neglects the radius influence of drainage holes. Because the size of drainage hole plays an important role in calculating the whole seepage field, therefore, this numerical model will produce big errors in the calculation, and the results are not reliable.

The abandoned element model is based on the finite element method, and it considers the hole-wall as inner boundary condition, and defines the boundary condition in order to simulate the actual drainage holes (Gureghian, Young, 1975). According to the abandoned element model, when the drainage holes locate under the water pressure, the hydraulic potential of hole-wall is defined to equal to the downstream water level. If the drainage holes locate higher than the downstream water level, the hydraulic potential of hole-wall is confined to equal to its position coordinates; when there is a free surface for the drainage holes, the hole-wall nodes are regarded as possible overflow points in the seepage calculation process. In order to simulate the size influence of drainage holes as precise as possible, the size of elements containing drainage holes needs to approach to the actual size of drainage holes as possible, which makes the mesh generation more difficult and more complicated.

The boundary element model has been proposed by Zhang(1982), which can calculate the seepage field conveniently and exactly with drainage holes. According to the boundary element model, only the boundary needs to be meshed. Every drainage holes boundary is independent, and the mesh size of every boundary can be confined independently with enough freedom. However, it is very difficult to solve the heterogeneous problem by applying this boundary element model.

The equivalent bar element model is also one practical model (Du, Xu, Han, 1991). Defining one suppositional bar element to simulate the drainage holes, the hydraulic potential of the bar element is confined as follows: at one end of the bar element, it is defined as the hydraulic potential of the drainage hole; at the another end of the bar element, it is defined as the average hydraulic potential of the drainage holes to be solved. The contribution to the relevant nodes by the bar element is taken into consideration in the calculation of hydraulic conductivity. The mesh size of the finite element containing bar element also needs to match the actual size of drainage holes, and it is still difficult to solve the heterogeneous problem by this model.

The drainage substructure model is proposed by Wang(1992). Defining one drainage element to cover the drainage holes, the drainage holes and the adjacent sub-domain are defined as substructures. The hole-wall is considered as confined boundary condition. The hydraulic conductivity is generated for every substructure firstly, and it can be transferred to the relevant nodes of drainage element through the inner function in the drainage element, then the seepage calculation can be carried out as usual. This model can be used efficiently for the structure with few drainage holes, but it is difficult and complicated to deal with the structure with many drainage holes, because it needs to pay attention to every different substructure.

Besides, there are many other analytical methods for drainage holes, but it is still difficult to handle the heterogeneous problems, especially with complicated boundary conditions.

1.2.4 Numerical algorithms for seepage and stress coupling analysis

Generally, the numerical algorithms for the seepage and stress coupling analysis can be classified into two categories: iterative algorithm and complete coupled algorithm (Wang, Xu, Su, 1998, 2000).

The iterative algorithm can be applied to solve the practical engineering very easily and conveniently. The seepage and stress coupling is carried out by iterative algorithm between the seepage and stress field. The changed stress field leads to the change of fracture aperture, which further influences the hydraulic conductivity, as well as the whole seepage field. On the other hand, the changed seepage load will lead to the change of stress field inversely. The whole coupling process will be finished when both the two fields satisfy the convergence precision. This algorithm is widely adopted in the practical engineering, and also satisfies the engineering precision.

The complete coupled algorithm is proposed by Wang, Xu, Su(1998, 2000). The proposed algorithm considers the seepage field and stress field as a whole, combining the seepage governing equation and the stress governing equation together, and taking the seepage and stress coupling into account. It has built a new governing equation with four freedom degrees to solve the displacements and hydraulic potential at the same time, see the eq.(1-1). However, it is very difficult to apply this algorithm into practical engineering, because it has one large, sparse, nonlinear, unsymmetrical "stiffness" matrix.

$$[M(\sigma)]\begin{Bmatrix} \delta_x \\ \delta_y \\ \delta_z \\ \phi \end{Bmatrix} = \{F(\sigma)\} \tag{1-1}$$

1.2.5 Permeability parameters of fractured rock mass

At present, there are several methods to obtain the permeability parameters of fractured rock mass, such as statistic method of geometrical shapes, back analysis method, situ test method, regressive analysis method, and so on.

The first method is basic and practical on the ground of geometrical shapes of rock fractures. Based on the equivalent continuum model, Po_{MM} (1966) has built the relationship between permeability tensor and geometrical parameters of rock fractures on the basis of cubic law. Because of the complicated distribution of rock fractures, Oda (1985, 1986) has proposed a new method to obtain the permeability tensor based on the statistical method, and it needs to define a new probability density function of fracture, depending on the statistical analysis of enough test data for fracture. This method has strict conditions, but it is difficult to be applied in the practical engineering. Zhang(2005) has modified the equivalent permeability tensor through the connectivity parameter, which is proposed by Oda, and the improved permeability tensor can be used for rock fractures extending infinitely.

The back analysis method is one numerical method based on the hydraulics of fracture network. According to the actual statistical data of rock fractures, several fracture network samples are built firstly. Based on the equivalent continuum model, the seepage calculation can be carried out, and the permeability parameters can be obtained through the seepage flow, according to the seepage ellipse theory. The seepage ellipse can be drawn by the permeability parameters at different directions, through the contrast among the different samples, and the optimal permeability parameters can be obtained.

There are several situ test methods for obtaining permeability parameters of fractured rock mass, such as conventional water pressure test with single hole, three-section water pressure test, cross holes test, and so on. For the fractured rock mass with complicated configuration, although it is difficult to show the actual permeability characteristics by the conventional water pressure test with single hole, which is still one important and practical method to obtain the permeability parameters in the engineering. In order to consider the non-isotropic permeability characteristics of fractured rock mass, American AD report (AD-AO21192) suggests that: concerning the mutual orthogonal fractures, the water pressure test can be taken at the different vertical directions of fracture surface, in order to obtain the permeability parameters of the other directions. The three-section water pressure test was proposed by Louis (1972). It is an advanced test of water pressure test with single hole, but it is very difficult to be applied for more than three sets of fractures, non-orthogonal fractures, and fractures with small space. In order to consider the complicated fracture with unconfined main direction, Hsieh, Neuman, and Simpson (1983) have proposed three dimensional cross holes test, Hsieh, Neuman, Hsieh et al.(1985) have developed the method to use for actual engineering, Aoki, et al.(1992) have put it into application in some projects. But for Three Gorge project and Xiaolangdi project in China, the obtained data are not very satisfactory by the cross holes test.

The regressive analysis method (Cooley, 1982, 1983, 1985; Sun, 1981; Du, 1991) is another back analysis method, according to the experimental data through bore-hole test with underground water level, based on the electro-network simulation and numerical method, the permeability parameters of fractured rock mass can be obtained by the regressive analysis and back analysis.

1.3 Main work of the dissertation

The seepage and stress coupling problem for fractured rock mass is a hot topic, especially in the southwest in China, where the geological and hydrological conditions are very complicated with high geo-stress, the seepage and stress coupling research plays an important role in estimating the safety and stability of extra-high abutment slide resistance block and slope, deep large span underground building, deep long tunnel, and so on.

Composite element method (CEM) is proposed by Chen, Egger, etc.(2002), it is a new numerical method for complicated structures with simple preprocess work, and has both the advantages of finite element method (FEM) and block element method (BEM). On the grant of nature science foundation of China (50679066) and the project of foundation treatment and safety estimation of Xiaowan arch dam (XW2006/D14-2-4), there are some researches on the seepage and stress coupling for fractured rock mass based on the CEM, and the main work of this dissertation can be briefly summarized as follows:

Based on the CEM, the seepage and normal stress coupling algorithm of fractured rock mass has been established firstly, in which the coupling mechanism has been carried out by the iterative algorithm between the seepage and stress field. After that, the seepage and stress coupling algorithm of fractured rock mass during the shear process also has been proposed by the CEM, in which the shear process has been divided into three phases: shear shrink phase, shear dilation up to peak value phase, and residual shear strength phase. The two proposed coupling algorithms can be used both for the filled and unfilled fractures, and also take the flow exchange between the fracture and adjacent rock block into consideration. The FORTRAN programs have been compiled for the proposed algorithms, and the proposed algorithms have been verified by simple numerical examples. Besides, taking comparison with the conventional equivalent continuum model, the obtained seepage velocities by the proposed algorithms are much closer to the actual ones, and the proposed algorithms are more useful and efficient in estimating the safety and stability in the practical engineering.

Because the drainage hole is also an important component in the seepage control system for fractured rock mass, the seepage and stress coupling algorithm of fractured rock mass containing drainage holes also has been established based on the CEM, in which the fracture and drainage hole are simulated explicitly by special elements, with considering the deformation and permeability characteristics. The hydraulic conductivity matrix of fractured rock mass containing drainage holes has been divided into five parts: rock mass sub-element, fracture sub-element, interface between rock block and fracture, interface between rock block and drainage hole, interface between the drainage holes. The FORTRAN programs also have been compiled for the proposed algorithm. The verification and application by the coupling algorithm has been presented compared to the FEM, in which the simple and convenient preprocess work can be well shown, since the fractures and drainage holes are embedded within the composite elements, the mesh construction will not be limited them strongly. The application and comparative study for the Baozhusi dam foundation have been presented also.

The last part of the dissertation is the application to Xiaowan arch dam with complicated foundation system. The proposed coupling algorithm is used for the four important fractures firstly, in which the validity and reliability of the algorithm has been well shown. Then the proposed coupling algorithm is further applied for the fractured rock mass containing three sets of fractures and drainage holes. The advantages of the algorithm are further verified and well shown in comparison with the FEM, due to its simpler preprocess work and more attention to the detailed structure configuration.

Chapter 2 Composite element method for fractured rock mass

Fracture is an important and basic medium in the fractured rock mass. Fluid mainly flows along the fractures, and most deformation of fractured rock mass is dependent on the fracture deformation. Therefore, the numerical simulation for fractures is the most important part in the characteristics study of fractured rock mass, and it is also a difficult problem. Many numerical methods and theories have been proposed in the last 3 decades, and they mainly focus on the hydraulic and deformation behavior of fractures, in order to illustrate the characteristics of fractures more precisely, such as finite element method (FEM), block element method (BEM), discontinuous deformation analysis method, numerical manifold method, and so on. Among these methods, the FEM is the most popular, especially in the practical engineering.

The numerical methods used in the study of rock fractures fall into two categories: the implicit (or equivalent continuum) approach, in which the influence of fractures is treated equivalently, and the rock mass containing fractures is considered as one homogeneous medium, neglecting the exact position and direction of fractures; the other one is the explicit (or discrete) approach, in which the fractures are simulated discretely by one special element with considering the exact position and direction. The former approach is used to simulate fractures of small sizes and large quantity, while the latter is applied for large-scaled fractures.

In theory, the explicit approach pays more attention on the characteristics of fractures, and the solutions are closer to the actual results, because the fractures are simulated more explicitly and exactly. However, in the practical engineering, it is very difficult to simulate fractures discretely, which demands enormous time, patience, energy, and so on. On the one hand, the distribution of fractures is very complicated, they intersect with each other, or the fracture shape is sinuous. Further more, fracture aperture is very small, and there are some nodes shared with the around rock masses, thus makes the mesh generation more difficult, even makes the generated mesh with bad shape, the calculation precision will be decreased.

Composite element method (CEM) proposed by Chen, Egger, etc.(2002), is a new numerical method, which can simulate the fractures, bolts, and drainages holes explicitly by the composite elements with considering the exact positions. The CEM has the advantages of FEM and BEM: defining the composite elements to cover the fractures, bolts, and drainages holes of different characteristics, generating the sub-elements by topology automatically, and then building the governing equations for every sub-element, finally assembling the sub-matrix to the matrix of the mapped element for the solution. The CEM can show the actual characteristics of every fractures, bolts, and drainages holes, but avoid taking more time on the complicated and inconvenient preprocess work.

2.1 Principle of composite element method

The notable characteristics of the CEM are that: it is able to contain one or more sets of discontinuities of specified characteristics, such as fractures, faults, bolts, drainage holes and so on, and all the preprocess work for these media are automatically disposed.

One composite element is defined to cover sub-domains of different shapes and characteristics, and these sub-domains are named as sub-elements. Two typical composite elements are shown in the Fig.2.1, in which Fig.2.1(a) shows one sub-element enclosed by another sub-element, which is used for bolts, drainages holes, and so on, and the sub-elements are related with each other through the interface; Fig.2.1(b) shows one composite element divided into several sub-elements by discontinuities, such as fractures, faults, and so on, and the neighbor sub-elements are related with each other through the discontinuities.

Unknown variables within each sub-element (e.g. ϕ, $\{\Delta u\}$) can be interpolated from the mapped nodal variables defined on the composite elements (e.g. $\{\phi\}$, $\{\Delta\delta\}$), and the shape function $[N]$ is the same to that of conventional FEM defined over the whole composite element, see the Eq.(2-1):

$$\begin{cases} \phi = [N]\{\phi\} \\ \{\Delta u\} = [N]\{\delta\} \end{cases} \tag{2-1}$$

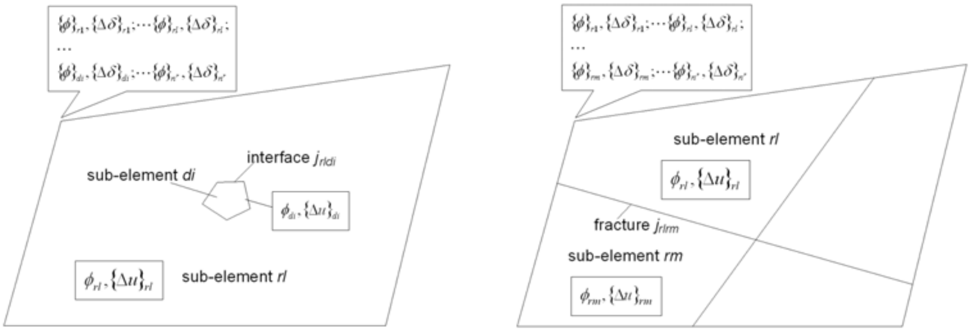

(a) **(b)**

Fig.2.1 Composite element containing sub-elements

The governing equation for the solution of the mapped nodal variables can be established by applying Virtual Work Principle or Variational Principle, and then the sub-matrix can be assembled into the whole matrix. The known variables of the sub-elements can be transferred to the mapped nodal variables on the composite element. The governing equation of one composite element containing n_r sub-elements can be obtained by that:

$$\begin{bmatrix} [K]_{1} & [K]_{2} & \cdots & [K]_{n_r} \\ [K]_{21} & [K]_{22} & \cdots & [K]_{2n_r} \\ \cdots & \cdots & \cdots & \cdots \\ [K]_{n_r 1} & [K]_{n_r 2} & \cdots & [K]_{n_r n_r} \end{bmatrix} \begin{Bmatrix} \{\bar{\phi}\}_1 \\ \{\bar{\phi}\}_2 \\ \cdots \\ \{\bar{\phi}\}_{n_r} \end{Bmatrix} = \begin{Bmatrix} \{f\}_1 \\ \{f\}_2 \\ \cdots \\ \{f\}_{n_r} \end{Bmatrix} \tag{2-2}$$

Where the diagonal components of the matrix are composed by the self sub-matrix and the sub-matrix resulted from the related interface:

$$[K]_{lrl} = [K]_{l} + \sum_{rl=1, rl\neq rm}^{n_r} A(rl,rm)[k]_{lrm} \tag{2-3}$$

And the non-diagonal components of the matrix only result from the related interface:

$$[K]_{lrm} = -A(rl,rm)[k]_{lrm} \tag{2-4}$$

In which $A(rl,rm) = \begin{cases} 1, \text{if } rl \text{ and } rm \text{ are neighbour sub-elements} \\ 0, \text{if } rl \text{ and } rm \text{ are not neighbour sub-elements} \end{cases}$, $[K]_{lrl}$ is the self sub-matrix of the sub-element *rl*, $[K]_{lrm}$ is the relevant part resulted from the interface between the sub-elements *rl* and *rm*, it shows the effect of interface on the sub-elements, and it is also one symmetrical matrix, that is $[K]_{lrm} = [K]_{mrl}$.

With the solved variables on the mapped nodes of composite elements, the unknown variable of the relevant sub-element can be solved through the shape function, thus the other variables of the sub-element can be further obtained.

2.2 Coordinate system and its transformation

The global coordinate system is defined as: the axis *x* is in the direction of east, the axis *y* is toward to north, and the axis *z* is upturned. In order to build governing equations conveniently, each fracture has its own local coordinate system, the axis $y_{j_{rlrm}}$ is along the fracture surface and points to the dip direction of fracture, the axis $z_{j_{rlrm}}$ is perpendicular to the fracture and points upwards, and the axis $x_{j_{rlrm}}$ is defined by right-hand rule (Fig.2.2). The subscript j_{rlrm} will be used to indicate the fracture sub-element between rock sub-element rl and rm.

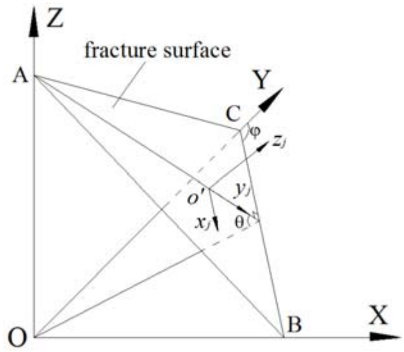

Fig.2.2 Local coordinate system of fracture

Eq.(2-5) defines the transformation of vector $\{A\}$ from the global coordinate system to the local coordinate system.

$$\{a\}_{j_{rlrm}} = [L]_{j_{rlrm}}(\{A\} - \{X\}_{j_{rlrm}}) \tag{2-5}$$

Where matrix $[L]_{j_{rlrm}}$ is defined by the dip direction $\varphi_{j_{rlrm}}$ and dip angle $\theta_{j_{rlrm}}$ of the fracture, and vector $[X]_{j_{rlrm}}$ is the central coordinate of the fracture in the global coordinate system.

$$[L]_{j_{rlrm}} = \begin{bmatrix} \cos\varphi_{j_{rlrm}} & -\sin\varphi_{j_{rlrm}} & 0 \\ \sin\varphi_{j_{rlrm}}\cos\theta_{j_{rlrm}} & \cos\varphi_{j_{rlrm}}\cos\theta_{j_{rlrm}} & -\sin\theta_{j_{rlrm}} \\ \sin\varphi_{j_{rlrm}}\sin\theta_{j_{rlrm}} & \cos\varphi_{j_{rlrm}}\sin\theta_{j_{rlrm}} & \cos\theta_{j_{rlrm}} \end{bmatrix} \tag{2-6}$$

2.3 Composite element method for stress problem

According to the elastic viscoplastic theory, the constitutive equation at the moment *t* is given by:

$$\begin{cases} \{\Delta\sigma\} = [D](\{\Delta\varepsilon\} - \{\varepsilon^{vp}\}\Delta t) \\ or \\ \{\Delta\varepsilon\} = [S]\{\Delta\sigma\} + \{\varepsilon^{vp}\}\Delta t \end{cases} \tag{2-7}$$

Where Δt is the step length, $[D]$ and $[S]$ are the elasticity matrix and flexibility matrix respectively, and the viscoplastic strain rate is:

$$\{\varepsilon^{vp}\} = \gamma < F > \left\{ \frac{\partial Q}{\partial\{\sigma\}} \right\} \tag{2-8}$$

Where γ is flow parameter, F and Q are yield function and potential function respectively, and the function <F> is defined as:

$$< F >= \begin{cases} F \quad if \quad F > 0 \\ 0 \quad if \quad F < 0 \end{cases} \tag{2-9}$$

Take one composite element containing two fractures for example, see Fig.2.3. The composite element is divided into four parts by the fractures, then there are four sub-elements, and every sub-element has its own mapped nodes for interpolating the displacement. The subscript *r* and *j* are used to indicate the rock and fracture sub-elements respectively, and * indicates the virtual variables.

$$\{\Delta u\}_{rl} = [N]\{\Delta\delta\}_{rl} \tag{2-10}$$

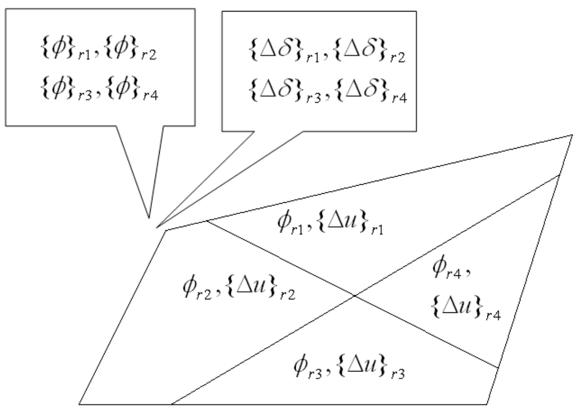

Fig.2.3 Composite element containing four sub-elements

2.3.1 Stiffness matrix of the rock sub-element

The elastic matrix of intact rock mass is given by:

$$[D]_{rl} = \begin{bmatrix} \lambda+2G & \lambda & \lambda & 0 & 0 & 0 \\ & \lambda+2G & \lambda & 0 & 0 & 0 \\ & & \lambda+2G & 0 & 0 & 0 \\ & & & G & 0 & 0 \\ & SYM & & & G & 0 \\ & & & & & G \end{bmatrix} \tag{2-11}$$

Defined the virtual displacement of rock sub-element as:

$$(\{\Delta u\}_{rl})^* = [N](\{\Delta\delta\}_{rl})^* \tag{2-12}$$

Then the virtual strain can be given by:

$$(\{\Delta\varepsilon\}_{rl})^* = [B]_{rl}(\{\Delta\delta\}_{rl})^* \tag{2-13}$$

Where

$$[B]_{ri} = \begin{bmatrix} \frac{\partial N_i}{\partial X} & 0 & 0 \\ 0 & \frac{\partial N_i}{\partial Y} & 0 \\ 0 & 0 & \frac{\partial N_i}{\partial Z} \\ 0 & \frac{\partial N_i}{\partial Z} & \frac{\partial N_i}{\partial Y} \\ \frac{\partial N_i}{\partial Z} & 0 & \frac{\partial N_i}{\partial X} \\ \frac{\partial N_i}{\partial Y} & \frac{\partial N_i}{\partial X} & 0 \end{bmatrix} \tag{2-14}$$

According to the Virtual Work Principle, it can be obtained that:

$$\sum_{rl=1}^{4} W_{rl} + \sum_{j=1}^{4} W_j = \sum_{rl=1}^{4} (\{\Delta\delta\}_{rl})^{*T}\{\Delta F\}_{rl} \tag{2-15}$$

Where $\{\Delta F\}_{rl}$ is the nodal displacement increment of composite element, resulting from the load increment of rock sub-element *rl*.

The virtual work of the rock sub-element can be obtained by:

$$W_{rl} = \iiint_{\Omega_{rl}} (\{\Delta\varepsilon\}_{rl})^{*T}\{\Delta\sigma\}_{rl}\, d\Omega \tag{2-16}$$

Substituting the Eqs.(2-7)(2-13) into the Eq.(2-16), the virtual work of rock sub-element can be written by:

$$W_{rl} = \iiint_{\Omega_{rl}} (\{\Delta\delta\}_{rl})^{*T}[B]_{rl}^T[D]_{rl}([B]_{rl}\{\Delta\delta\}_{rl} - \{\varepsilon^{vp}\}_{rl}\Delta t)\, d\Omega \tag{2-17}$$

The governing equation for the rock sub-element *rl* can be obtained:

$$[K]_{rl}\{\Delta\delta\}_{rl} = \{\Delta F\}_{rl} + \{\Delta f^{vp}\}_{rl} \tag{2-18}$$

Where

$$[K]_{rl} = \iiint_{\Omega_{rl}} [B]_{rl}^{T}[D]_{rl}[B]_{rl}\, d\Omega \tag{2-19}$$

$$\{\Delta f^{vp}\}_{rl} = \iiint_{\Omega_{rl}} [B]_{rl}^{\mathrm{T}}[D]_{rl}[\varepsilon^{\mathrm{vp}}]_{rl}\, \Delta t \mathrm{d}\Omega \tag{2-20}$$

2.3.2 Stiffness matrix of the fracture sub-element

The elastic matrix of fracture is given by in the local coordinate system:

$$[D]_j = \begin{bmatrix} k_s & 0 & 0 \\ 0 & k_s & 0 \\ 0 & 0 & k_n \end{bmatrix} \tag{2-21}$$

Where k_n and k_s are the normal and tangential stiffness respectively.

Taking the fracture segment j_{r1r2} for example, strain increment $\{\Delta\varepsilon\}_j$ is substituted by the relative displacement increment $\{\Delta u\}_j$, which results from the displacement increment of rock mass, and then the relative displacement increment can be given by in the local coordinate system:

$$\{\Delta u\}_{j_{r1r2}} = [L]_j(\{\Delta u\}_{r1} - \{\Delta u\}_{r2}) = [L]_j[N](\{\Delta\delta\}_{r1} - \{\Delta\delta\}_{r2}) \tag{2-22}$$

Where $r1, r2$ are the rock sub-elements neighboring with the fracture segment j_{r1r2}.

The virtual work of fracture can be obtained by:

$$W_j = \iint_{\Gamma_{j_{rlrm}}} (\{\Delta u\}_{j_{r1r2}})^{*T}\{\Delta\sigma\}_j\, d\Gamma \tag{2-23}$$

Substituting the Eqs.(2-7)(2-22) into the Eq.(2-23), the virtual work of fracture can be written by:

$$W_j = \iint_{\Gamma_{j_{r1r2}}} ((\{\Delta\delta\}_{r1})^{*T} - (\{\Delta\delta\}_{r2})^{*T})[N]^T[L]_j^{\ T}[D]_j[L]_j([N](\{\Delta\delta\}_{r1} - \{\Delta\delta\}_{r2}) - \{\varepsilon^{vp}\}_j\Delta t)d\Gamma \tag{2-24}$$

The governing equation for fracture sub-element j_{r1r2} can be obtained:

$$\begin{cases} [k]_{r1r2}\{\Delta\delta\}_{r1} - [k]_{r1r2}\{\Delta\delta\}_{r2} = \{\Delta f^{vp}\}_{r1r2} \\ -[k]_{r2r1}\{\Delta\delta\}_{r1} + [k]_{r2r1}\{\Delta\delta\}_{r2} = \{\Delta f^{vp}\}_{r2r1} \end{cases} \tag{2-25}$$

Where $[k]_{r1r2}$, $[k]_{r2r1}$ are the stiffness matrixes of interface between rock sub-element *r1* and *r2*.

$$[k]_{r1r2} = [k]_{r2r1} = \iint_{\Gamma_{j_{r1r2}}} [N]^T [L]_j^{\ T} [D]_j [L]_j [N] d\Gamma \tag{2-26}$$

$$\{\Delta f^{\mathrm{vp}}\}_{r1r2} = \{\Delta f^{\mathrm{vp}}\}_{r2r1} = \iint_{\Gamma_{j_{r1r2}}} [N]^T [L]_j^T [D]_j \{\varepsilon^{vp}\}_j \Delta t \mathrm{d}\Gamma \tag{2-27}$$

Substituting the Eqs.(2-17)(2-24) into Eq.(2-15), the governing equation according to the Virtual Work Principle can be obtained by (Qiang, Chen, 2004):

$$\begin{bmatrix} [K]_{r1r1} & -[k]_{r1r2} & 0 & -[k]_{r1r4} \\ -[k]_{r2r1} & [K]_{r2r2} & -[k]_{r2r3} & 0 \\ 0 & -[k]_{r3r2} & [K]_{r3r3} & -[k]_{r3r4} \\ -[k]_{r4r1} & 0 & -[k]_{r4r3} & [K]_{r4r4} \end{bmatrix} \begin{Bmatrix} \{\Delta\delta\}_{r1} \\ \{\Delta\delta\}_{r2} \\ \{\Delta\delta\}_{r3} \\ \{\Delta\delta\}_{r4} \end{Bmatrix} = \begin{Bmatrix} \{\Delta F\}_{r1} + \{\Delta F^{vp}\}_{r1} \\ \{\Delta F\}_{r2} + \{\Delta F^{vp}\}_{r2} \\ \{\Delta F\}_{r3} + \{\Delta F^{vp}\}_{r3} \\ \{\Delta F\}_{r4} + \{\Delta F^{vp}\}_{r4} \end{Bmatrix} \tag{2-28}$$

Where

$$[K]_{r1r1} = [K]_{r1} + [k]_{r1r2} + [k]_{r1r4};\ [\Delta F^{vp}]_{r1} = [\Delta f^{vp}]_{r1} + [\Delta f^{vp}]_{r1r2} + [\Delta f^{vp}]_{r1r4} \tag{2-29}$$

$$[K]_{r2r2} = [K]_{r2} + [k]_{r2r1} + [k]_{r2r3};\ [\Delta F^{vp}]_{r2} = [\Delta f^{vp}]_{r2} + [\Delta f^{vp}]_{r2r1} + [\Delta f^{vp}]_{r2r3} \tag{2-30}$$

$$[K]_{r3r3} = [K]_{r3} + [k]_{r3r2} + [k]_{r3r4};\ [\Delta F^{vp}]_{r3} = [\Delta f^{vp}]_{r3} + [\Delta f^{vp}]_{r3r2} + [\Delta f^{vp}]_{r3r4} \tag{2-31}$$

$$[K]_{r4r4} = [K]_{r4} + [k]_{r4r1} + [k]_{r4r3};\ [\Delta F^{vp}]_{r4} = [\Delta f^{vp}]_{r4} + [\Delta f^{vp}]_{r4r1} + [\Delta f^{vp}]_{r4r3} \tag{2-32}$$

Where the component is equal to zero, it is indicated that this fracture segment has no relationship with the main rock sub-element *rl*, such as the rock sub-element *r2* is only neighbored with fracture segments j_{r2r1} and j_{r2r3}.

2.4 Composite element method for seepage problem

Denote the hydraulic potential function as $\phi = Z + p/\gamma$, where Z is the vertical coordinate of the position concerned, p is the hydraulic pressure, γ is the volumetric weight of water. The governing equation of the seepage flow in perfectly saturated rock under the assumptions that both rock grains and pore water are incompressible and that the rock skeleton is rigid, and it is given by:

$$L\phi = f \tag{2-33}$$

Where f is the inner source density. The Eq.(2-33) is subject to appropriate boundary conditions:

$$\phi\big|_{\Gamma_1} = \phi_0 \qquad \text{(first type)} \tag{2-34}$$

$$\{n\}^T[k]\{S\}\phi\big|_{\Gamma 2} = -g \qquad \text{(second type)} \tag{2-35}$$

Where ϕ_0 is the specified hydraulic potential at the first type boundary, and g is the flow rate through the second type boundary. Free surface is a special boundary on which the following two conditions should be satisfied:

$$\begin{cases} \phi = Z \\ \{n\}^T[k]\{S\}\phi = 0 \end{cases} \tag{2-36}$$

in which $\{n\}$ is the unit normal vector of the boundary surface:

$$\{n\}^T = \lfloor l_x \quad l_y \quad l_z \rfloor \tag{2-37}$$

In the Eqs.(2-33)~(2-37) L and $\{S\}$ are the differential operators and $[k]$ is the permeability matrix:

$$L = \{S\}^T[k]\{S\} \tag{2-38}$$

$$\{S\} = \left[\frac{\partial}{\partial X}\ \frac{\partial}{\partial Y}\ \frac{\partial}{\partial Z}\right] \tag{2-39}$$

$$[k] = \begin{bmatrix} k_X & k_{XY} & k_{XZ} \\ k_{YX} & k_Y & k_{YZ} \\ k_{ZX} & k_{ZY} & k_Z \end{bmatrix} \tag{2-40}$$

The corresponding governing equation comes from the minimization of the following variational function:

$$I(\phi) = \iiint_{\Omega}\left(\frac{1}{2}(\{S\}\phi)^T[k](\{S\}\phi) + f\phi\right)dR + \iint_{\Gamma} g\phi d\Gamma \tag{2-41}$$

The variational function in the Eq.(2-41) can be discretized using the conventional finite element algorithm, and the "residual flow" iteration method (Desai, 1976) can be used to solve the unconfined seepage field.

2.4.1 Conductivity matrix of rock sub-element

Take one composite element containing two fractures for example, see the Fig.2.3. Like the stress problem, every sub-element also has its own mapped nodes for interpolating the hydraulic potential.

For the rock sub-element, according to the variational function (2-41), it can be obtained that:

$$I(\phi)_{rl} = \iiint_{\Omega_{rl}} \left(\frac{1}{2}(\{S\}\phi_{rl})^T [k]_{rl}(\{S\}\phi_{rl}) + f\phi_{rl}\right) d\Omega + \iint_{\Gamma_{rl}} g\phi_{rl} d\Gamma \qquad (rl = r1, r2, r3, r4) \qquad (2\text{-}42)$$

Based on the Variational Principle, and substituting the Eq.(2-1), the Eq.(2-42) can be written by:

$$\begin{aligned}\delta I_{rl} &= \iiint_{\Omega_{rl}} \left((\{S\}[N])^T [k]_{rl} \{S\}[N]\{\phi\}_{rl} + f[N]\right) d\Omega + \iint_{\Gamma_{rl}} g[N] d\Gamma \\ &= 0\end{aligned} \qquad (rl = r1, r2, r3, r4) \qquad (2\text{-}43)$$

Denote the Eq.(2-43) as:

$$[h]_{rl}\{\phi\}_{rl} = \{f\}_{rl} \qquad (rl = r1, r2, r3, r4) \qquad (2\text{-}44)$$

Where $[h]_{rl}$ and $\{f\}_{rl}$ are the conductivity matrix and equivalent nodal flow rate of the sub-element *rl* respectively.

$$[h]_{rl} = \iiint_{\Omega_{rl}} (\{S\}[N])^T [k]_{rl} (\{S\}[N]) d\Omega \qquad (rl = r1, r2, r3, r4) \qquad (2\text{-}45)$$

$$\{f\}_{rl} = -\iiint_{\Omega_{rl}} [N] f d\Omega - \iint_{\Gamma_{rl}} [N] g d\Gamma \qquad (rl = r1, r2, r3, r4) \qquad (2\text{-}46)$$

2.4.2 Conductivity matrix of fracture sub-element

Concerning the fracture (see Fig.2.4), there are some assumptions (Feng, Chen, 2006): ①There are some filled materials in the fracture, fracture aperture is $e_{j_{rlrm}}$, and the permeability coefficient of fracture can be obtained by experiments; ②fracture aperture $e_{j_{rlrm}}$ is relatively quite small compared with the element size and fracture length, and the vertical seepage velocity of fracture $v_{z_{j_{rlrm}}}$ keeps constant, that is the hydraulic potential of fracture keeps linear variety in the normal direction of fracture surface.

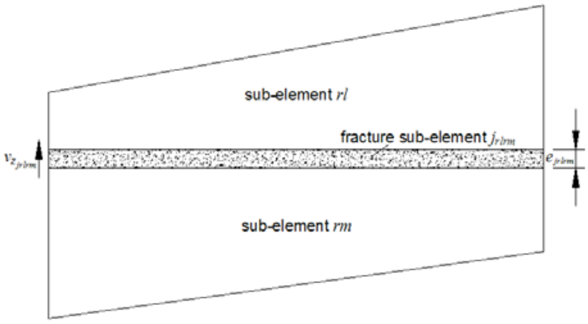

Fig.2.4 Sketch of fracture with some assumptions

Taking the fracture segment j_{r1r2} for example, according to the assumption ◯,2, the hydraulic potential and seepage gradient of fracture can be written by:

$$\phi_j = \frac{\phi_{r1} + \phi_{r2}}{2} \tag{2-47}$$

$$J_{z_{j_{r1r2}}} = \frac{\phi_{r1} - \phi_{r2}}{e_{j_{r1r2}}} \tag{2-48}$$

According to the Eq.(2-41), the variational function of fracture can be obtained that:

$$I(\phi)_{j_{r1r2}} = \iiint_{\Omega_{j_{r1r2}}} \left(\frac{1}{2} (\{S\}\phi)^T [k]_{j_{r1r2}} (\{S\}\phi) \right) d\Omega \tag{2-49}$$

Because the fracture aperture $e_{j_{r1r2}}$ is much smaller compared to the dimension of the composite element, then it can be assumed that the hydraulic potential gradient keeps constant in the normal direction of fracture surface, and the volumetric infinitesimal can be written as:

$$d\Omega = dx_j dy_j \cdot e_{j_{r1r2}} \tag{2-50}$$

Then the Eq.(2-49) can be written by:

$$I(\phi)_{j_{r1r2}} = e_{j_{r1r2}} \iint_{j_{r1r2}} \frac{1}{2} \left(\{S_j\}\phi)^T [k]_{j_{r1r2}} (\{S_j\}\phi \right) dx_j dy_j \tag{2-51}$$

According to the assumptions, the Eq.(2-47) can be written by:

$$\begin{cases} \dfrac{\partial \phi}{\partial x_j} = \dfrac{\lfloor N_{x_j} \rfloor}{2} (\{\phi\}_{r1} + \{\phi\}_{r2}) \\ \dfrac{\partial \phi}{\partial y_j} = \dfrac{\lfloor N_{y_j} \rfloor}{2} (\{\phi\}_{r1} + \{\phi\}_{r2}) \\ \dfrac{\partial \phi}{\partial z_j} = \lfloor N \rfloor \dfrac{(\{\phi\}_{r1} - \{\phi\}_{r2})}{e_{j_{r1r2}}} \end{cases} \tag{2-52}$$

Where

$$[N_{x_j}] = [\frac{\partial N}{\partial x_j}];\ [N_{y_j}] = [\frac{\partial N}{\partial y_j}] \tag{2-53}$$

Combining the Eqs.(2-51)(2-52), the governing equations for the fracture sub-elements can be obtained:

$$\begin{cases} [h]_{r1r1}\{\phi\}_{r1} + [h]_{r1r2}\{\phi\}_{r2} = 0 \\ [h]_{r2r1}\{\phi\}_{r1} + [h]_{r2r2}\{\phi\}_{r2} = 0 \end{cases} \tag{2-54}$$

Where $[h]_{r1r1}$, $[h]_{r2r2}$, $[h]_{r1r2}$, $[h]_{r2r1}$ are the conductivity matrixes of interface between rock sub-element *r1* and sub-element *r2*.

$$\begin{cases} [h]_{r1r1} = [h]_{r2r2} = \dfrac{e_{j_{r1r2}}}{2}\iint\limits_{j_{r1r2}}\left(\dfrac{k_{x_j}}{2}[N_{x_j}]^T[N_{x_j}] + \dfrac{k_{y_j}}{2}[N_{y_j}]^T[N_{y_j}] + \dfrac{2k_{z_j}}{e_{j_{r1r2}}^{\ 2}}[N]^T[N]\right)dx_j dy_j \\ [h]_{r1r2} = [h]_{r2r1} = \dfrac{e_{j_{r1r2}}}{2}\iint\limits_{j_{r1r2}}\left(\dfrac{k_{x_j}}{2}[N_{x_j}]^T[N_{x_j}] + \dfrac{k_{y_j}}{2}[N_{y_j}]^T[N_{y_j}] - \dfrac{2k_{z_j}}{e_{j_{r1r2}}^{\ 2}}[N]^T[N]\right)dx_j dy_j \end{cases} \tag{2-55}$$

The other fracture segments can be taken into consideration as the same of j_{r1r2}, and then assembling the governing equations for sub-elements, the whole governing equations of one composite element containing four rock sub-elements and four fracture sub-elements can be obtained:

$$\begin{bmatrix} [H]_{r1r1} & [h]_{r1r2} & 0 & [h]_{r1r4} \\ [h]_{r2r1} & [H]_{r2r2} & [h]_{r2r3} & 0 \\ 0 & [h]_{r3r2} & [H]_{r3r3} & [h]_{r3r4} \\ [h]_{r4r1} & 0 & [h]_{r4r3} & [H]_{r4r4} \end{bmatrix} \begin{Bmatrix} \{\phi\}_{r1} \\ \{\phi\}_{r2} \\ \{\phi\}_{r3} \\ \{\phi\}_{r4} \end{Bmatrix} = \begin{Bmatrix} \{f\}_{r1} \\ \{f\}_{r2} \\ \{f\}_{r3} \\ \{f\}_{r4} \end{Bmatrix} \tag{2-56}$$

Where

$$[H]_{r1r1} = [h]_{r1} + [h]_{r1r2} + [h]_{r1r4} \tag{2-57}$$

$$[H]_{r2r2} = [h]_{r2} + [h]_{r2r1} + [h]_{r2r3} \tag{2-58}$$

$$[H]_{r3r3} = [h]_{r3} + [h]_{r3r2} + [h]_{r3r4} \tag{2-59}$$

$$[H]_{r4r4} = [h]_{r4} + [h]_{r4r3} + [h]_{r4r1} \tag{2-60}$$

Where the component is equal to zero, it is also indicated that this fracture segment has no relationship with the main rock sub-element *rl*, like the governing equation for the stress problem.

Chapter 3 Seepage and stress coupling for fractured rock mass

Composite element method (CEM) is a new numerical simulation method, proposed by Chen, Egger, etc.(2002), Chen, Qiang, Chen, (2003). It includes advantages of both finite element method (FEM) and block element method (BEM), and also can be applied for the analysis on the deformation, seepage and thermal for continuous and discontinuous medium. In the practical engineering project, due to some natural or artificial reasons, there are always many kinds of media in the rock mass, such as faults, fractures, bolts, drainage holes and so on. For the large scale micro fractures and systematic bolts, they need be simulated equivalently, while for the large-scale faults and fractures, they need be simulated discretely generally. Concerning the enormous rock mass projects and much complicated geological structures, it is much more difficult in the mesh generation based on the FEM, because the discontinuities staggered cut each other. Even if the mesh has been generated constrainedly, the topological structure of element might be abnormal evidently, shown distortedly, which would bring unfavorable error for the calculation. In addition, the construction condition, and the scheme of reinforced bolts and seepage control system are changed frequently, they lead to pay much more time and energy on the mesh modification. It is also very difficult to make discrete simulation for the engineering with much complicated configuration, especially for some micro or intersected fractures, even in virtue of present popular software with powerful function for preprocess. How to simplify the mesh generation work? It becomes a critical problem, and is always concerned in the academic and engineering field. Therefore, the CEM is emerged as the times require. The mesh based on CEM can treat the research region as a homogeneous medium, without considering the exact position and direction of fractures, bolts and drainage holes, because the discontinuities and structural bodies can be embedded into the composite elements automatically through the preprocess of CEM, which makes the preprocess work much easier and more efficient.

There is an important and complicated coupling between the seepage and stress field in fractured rock mass. On the one hand, the stress field is influenced by the seepage loads; on the other hand, the stress field affects the permeability characteristics and in turn the seepage field as well. The stress acting on the fracture surface leads to the change of fracture aperture, which causes the change of conductivity matrix of the fractured rock mass and the seepage field. According to this coupling mechanism, the seepage and stress coupling analysis for fractured rock mass can be achieved by applying the iterative algorithm. It is also widely recognized that in the geological engineering, the influence of fracture shear stress is less important than that of the fracture tension or compression.

The research on the seepage and normal stress coupling for fractured rock mass includes experimental technology, mechanics parameters, numerical models, and numerical algorithms. Snow(1968) has built the relationship between permeability coefficient and fracture aperture for horizontal fracture. Louis(1974) has obtained a famous semi-empirical formula between permeability coefficient and normal stress through the packer test in borehole with different depth for the homogeneous fractured rock mass. Gale (1982) has proposed experiential formula between permeability coefficient and normal stress through the laboratory experiments on the three kinds of rock mass. Barton(1976), Barton, Choubey(1977) have proposed joint roughness coefficient (JRC), and founded one empirical formula for seepage and stress coupling. Malama, Kulatilake(2003) have proposed a general exponential model by defining half-closure stress $\sigma_{1/2}$, in which fracture deformation is a function of maximum fracture closure and $\sigma_{1/2}$. Tsang, Witherspoon(1981), Chen, Wang, Xiong(1989) have proposed physical models to simulate the coupling behavior between seepage and normal stress.

The numerical methods used in the study of rock fractures fall into two categories: the implicit (or equivalent continuum) approach (Zienkiewicz, 1966, 1977; Hsieh, Neuman, 1985; Oda, 1985, 1986), which takes into account the deformation and permeability characteristics of fractures but neglects their exact positions; and the explicit (or discrete) approach (Schwartz, etc. 1985; Andersson, Dverstorp, 1987; Dershowitz, Einstein 1987; Cacas, etc. 1990), which considers the geological and mechanical properties of each fracture deterministically. The former model is used to simulate fractures of small size and large quantity, while the latter is adopted for large-scaled fractures.

The CEM proposed by Chen, Egger, etc.(2002) can discrete the fractured rock region concerned as one homogeneous medium, the fractures, bolts and drainage holes can be embedded within the elements but be simulated explicitly. In this way the computation mesh generation based on the CEM is more simple and convenient, especially for the complicated fractured rock problems.

This chapter develops the composite element algorithm to cover seepage and normal stress coupling cases firstly, and then it further develops the composite element algorithm for the seepage and stress coupling during the shear process. The proposed algorithm has the advantages of simplicity in the preprocess work, and be adaptive for both the filled and non-filled fractures. Further more, the flow exchange between the fractures and adjacent rock mass can be taken into consideration. The proposed coupling algorithm has been verified by simple numerical examples, and will be applied to the Xiaowan arch dam foundation in the chapter 5.

3.1 Governing equation for stress problem with complicated fractures

Assume that there are n_r sub-elements in one composite element, and then there are n_r sets of mapped nodal displacement on this composite element, which is used to interpolate the displacement of each sub-element through the shape function. According to the Virtual Work Principle, the governing equation of complicated fractured rock mass for stress problem based on the CEM can be expressed as:

$$[K]_{rlrl}\{\Delta\delta\}_{rl} + \sum_{rm=1,rm\neq rl}^{n_r} H_1(rl,rm)[k]_{rlrm}\{\Delta\delta\}_{rm} = \{\Delta F\}_{rl} + \{\Delta F^{vp}\}_{rl} \qquad rl = 1,2\cdots,n_r \quad (3\text{-}1)$$

Where

$$\begin{cases} [k]_{rlrm} = -\iint_{\Gamma_{j_{rlrm}}} [N]^{\mathrm{T}}[L]^{\mathrm{T}}_{j_{rlrm}}[D]_{j\,rlrm}[L]_{j\,rlrm}[N]\mathrm{d}\Gamma \\ [K]_{rlrl} = \iiint_{\Omega_{rl}} [B]^{\mathrm{T}}_{rl}[D]_{rl}[B]_{rl}\,\mathrm{d}\Omega - \sum_{rm=1,rm\neq rl}^{n_r} H_1(rl,rm)[k]_{rlrm} \\ H_1(rl,rm) = \begin{cases} 1, \text{if } rl \text{ and } rm \text{ are the adjacent sub-elements} \\ 0, \text{if } rl \text{ and } rm \text{ are not the adjacent sub-elements} \end{cases} \end{cases} \quad (3\text{-}2)$$

$$\begin{cases} \{\Delta F^{\mathrm{vp}}\}_{rl} = \iiint_{\Omega_{rl}} [B]^{\mathrm{T}}_{rl}[D]_{rl}[\varepsilon^{\mathrm{vp}}]_{rl}\,\Delta t\mathrm{d}\Omega + \sum_{rm=1,rm\neq rl}^{n_r} H_2(rl,rm)[\Delta f^{\mathrm{vp}}]_{rlrm} \\ \{\Delta f^{\mathrm{vp}}\}_{rlrm} = \iint_{\Gamma_{j_{rlrm}}} [N]^{T}[L]^{T}_{j_{rlrm}}[D]_{j\,rlrm}[\varepsilon^{vp}]_{j\,rlrm}\Delta t\mathrm{d}\Gamma \\ H_2(rl,rm) = \begin{cases} 1, rl > rm\,; -1, rl < rm \\ 0, \text{if } rl \text{ and } rm \text{ are not the adjacent sub-elements} \end{cases} \end{cases} \quad (3\text{-}3)$$

3.2 Governing equation for seepage problem with complicated fractures

Assume that there are n_r sub-elements in one composite element, and then there are n_r sets of mapped nodal hydraulic potential on this composite element, which is used to interpolate the hydraulic potential of each sub-element through the shape function. According to the Variational Principle, the governing equation of complicated fractured rock mass for seepage problem based on the CEM can be expressed as:

$$\begin{cases} ([h]_{rl} + \sum\limits_{rm=1,\ rm\neq rl}^{n_r} H_3(rl,rm)[h]_{rlrl})\{\phi\}_{rl} + \sum\limits_{rm=1,rm\neq rl}^{n_r} H_3(rl,rm)[h]_{rlrm}\{\phi\}_{rm} = \{f\}_{rl} \qquad rl = 1,2\cdots,n_r \\ H_3(rl,rm) = \begin{cases} 1, \text{if } rl \text{ and } rm \text{ are the adjacent sub-elements} \\ 0, \text{if } rl \text{ and } rm \text{ are not the adjacent sub-elements} \end{cases} \end{cases} \tag{3-4}$$

Where

$$\begin{cases} [h]_{rlrl} = \dfrac{e}{2}\iint\limits_{\Gamma_{j_{rlrm}}} \left(\dfrac{k_{x_{j_{rlrm}}}}{2}[N_{x_{j_{rlrm}}}]^{\mathrm{T}}[N_{x_{j_{rlrm}}}] + \dfrac{k_{y_{j_{rlrm}}}}{2}[N_{y_{j_{rlrm}}}]^{\mathrm{T}}[N_{y_{j_{rlrm}}}] + \dfrac{2k_{z_{j_{rlrm}}}}{e^2}[N]^{\mathrm{T}}[N] \right) dx_{j_{rlrm}} y_{j_{rlrm}} \\ [h]_{rlrm} = \dfrac{e}{2}\iint\limits_{\Gamma_{j_{rlrm}}} \left(\dfrac{k_{x_{j_{rlrm}}}}{2}[N_{x_{j_{rlrm}}}]^{\mathrm{T}}[N_{x_{j_{rlrm}}}] + \dfrac{k_{y_{j_{rlrm}}}}{2}[N_{y_{j_{rlrm}}}]^{\mathrm{T}}[N_{y_{j_{rlrm}}}] - \dfrac{2k_{z_{j_{rlrm}}}}{e^2}[N]^{\mathrm{T}}[N] \right) dx_{j_{rlrm}} y_{j_{rlrm}} \end{cases} \tag{3-5}$$

$$\begin{cases} [h]_{rl} = \iiint\limits_{\Omega_{rl}} (\{S\}[N])^{\mathrm{T}}[k]_{rl}(\{S\}[N])\mathrm{d}\Omega \\ \{f\}_{rl} = -\iiint\limits_{\Omega_{rl}} [N]f\,\mathrm{d}\Omega - \iint\limits_{\Gamma_{rl}} [N]g\,\mathrm{d}\Gamma \end{cases} \tag{3-6}$$

Where variable e is denoted as fracture aperture, $k_{x_{j_{rlrm}}}$, $k_{y_{j_{rlrm}}}$, $k_{z_{j_{rlrm}}}$ represent hydraulic conductivity of the fracture in the direction $x_{j_{rlrm}}, y_{j_{rlrm}}$, $z_{j_{rlrm}}$ respectively.

3.3 Seepage velocity

Fracture is the main seepage channel for fractured rock mass, and it also brings about remarkable anisotropy characteristics on permeability in the fractured rock mass. For the fractured rock mass with well developed fractures, the permeability characteristics of fractures have been treated with uniform distribution in the rock mass, that is to say, the fractured rock mass has been considered as an integral seepage medium with anisotropy characteristics. Concerning the permeability characteristics for fractured rock mass, according to Darcy's law, one component of seepage velocity is not only proportional to the component of hydraulic gradient at the same direction, but also proportional to the ones at the other directions:

Seepage velocity can be obtained by:

$$\{V\}_{rl} = -k_{ij}\{S\}\{\phi\}_{rl} \tag{3-7}$$

Where k_{ij} is permeability tensor, denoted by $[k]$.It is written in the Cartesian coordinates system as:

$$[k] = \begin{bmatrix} k_{xx} & k_{xy} & k_{xz} \\ k_{yx} & k_{yy} & k_{yz} \\ k_{zx} & k_{zy} & k_{zz} \end{bmatrix} \tag{3-8}$$

Due to the symmetry characteristics, there are 6 independent components for 3-D permeability tensor, and only 3 independent components for 2-D. Where *x*, *y*, *z* represent the three main flow directions. In calculating the seepage velocity, for rock mass, k_x, k_y, k_z represent k_{rlx}, k_{rly}, k_{rlz} respectively, and for rock fractures, they represent $k_{x_{jrlrm}}$, $k_{y_{jrlrm}}$, $k_{z_{jrlrm}}$ respectively.

3.4 Seepage load

Denote the hydraulic potential function as $\phi = Z + p/\gamma_w$, where Z is the vertical coordinate of the position concerned, p is the hydraulic pressure, γ_w is the volumetric weight of the water. Water load is considered as seepage volume load, and it can be obtained as:

$$\{F\}_{rl} = -\{S\}\{p\}_{rl} = \begin{cases} -\gamma_w \dfrac{\partial\{\phi\}_{rl}}{\partial x} \\ -\gamma_w \dfrac{\partial\{\phi\}_{rl}}{\partial y} \\ -\gamma_w \dfrac{\partial\{\phi\}_{rl}}{\partial z} + \gamma_w \end{cases} \tag{3-9}$$

3.5 Seepage and normal stress coupling mechanism

Since flow rate depends on the third power of fracture aperture, and most deformation of fractured rock mass is generated by fracture deformation, therefore, fracture deformation governs the flow capability of fractured rock mass. Because the behavior of fracture is more dependent on the normal stress than on the shear stress, only the seepage and normal stress coupling is taken into consideration first.

3.5.1 Effect of seepage on deformation

Rock fracture can be classified as filled fracture and non-filled fracture. Non-filled fracture can be represented as two parallel plates in contact with convex parts, and the asperities are considered as a layer of granular material which has high porosity and is clipped by the two parallel plates. Accordingly, Chen, Wang, Xiong(1989) have proposed "filled model", which considers the asperities as an evenly "filled" medium, with deformation and permeability characteristics. In this way, a uniform model for both the filled and non-filled fractures can be established.

Assuming that there are normal stress σ_{z_j} and shear stress $\tau_{z_j x_j}$, $\tau_{z_j y_j}$ on the fracture surface, as shown in the Fig.3.1. Because fracture aperture is very small, the strain of fracture can be restricted as follows:

$$\left.\begin{aligned} \varepsilon_{x_j} = \varepsilon_{y_j} = 0 \\ \gamma_{x_j y_j} = \gamma_{y_j x_j} = 0 \end{aligned}\right\} \tag{3-10}$$

Therefore constitutive relationship for fracture is built:

$$\begin{Bmatrix} \mathrm{d}\sigma_{z_j} \\ \mathrm{d}\tau_{z_j x_j} \\ \mathrm{d}\tau_{z_j y_j} \end{Bmatrix} = \begin{bmatrix} \lambda + 2G & 0 & 0 \\ 0 & G & 0 \\ 0 & 0 & G \end{bmatrix} \begin{Bmatrix} \mathrm{d}\varepsilon_{z_j} \\ \mathrm{d}\gamma_{z_j x_j} \\ \mathrm{d}\gamma_{z_j y_j} \end{Bmatrix} \tag{3-11}$$

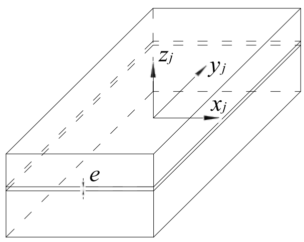

Fig.3.1 Rock mass containing single fracture

The corresponding displacement of the axes *x*, *y*, *z* are denoted respectively by u_{x_j}, u_{y_j} , u_{z_j}, then fracture aperture can be expressed, $e = e_0 + u_{z_\mathrm{j}}$, where e_0 is the original fracture aperture.

Thus Eq.(3-11) can be written as:

$$\begin{Bmatrix} \mathrm{d}\sigma_{z_\mathrm{j}} \\ \mathrm{d}\tau_{z_\mathrm{j}x_\mathrm{j}} \\ \mathrm{d}\tau_{z_\mathrm{j}y_\mathrm{j}} \end{Bmatrix} = \begin{bmatrix} k_\mathrm{n} & 0 & 0 \\ 0 & k_\mathrm{s} & 0 \\ 0 & 0 & k_\mathrm{s} \end{bmatrix} \begin{Bmatrix} \mathrm{d}u_{z_\mathrm{j}} \\ \mathrm{d}u_{x_\mathrm{j}} \\ \mathrm{d}u_{y_\mathrm{j}} \end{Bmatrix} \tag{3-12}$$

Where $k_\mathrm{n} = \dfrac{\lambda + 2G}{e}, k_\mathrm{s} = \dfrac{G}{e}$ (3-13)

k_n, k_s are shown respectively for normal and tangent stiffness coefficient of the fracture. According to Eq.(3-13), it is assumed that parameters λ and *G* are keeping constant, k_n, k_s can be as a function of normal stress, because aperture *e* has a relation with normal deformation $u_{z_{jrlrm}}$, which is depended on normal stress $\sigma_{z_{jrlrm}}$.

From (3-12) it can be obtained:

$$\mathrm{d}\sigma_{z_{jrlrm}} = k_\mathrm{n} du_{z_{jrlrm}} = \frac{\lambda + 2G}{e} du_{z_{jrlrm}} = \frac{\lambda + 2G}{e_0 + u_{z_{jrlrm}}} \mathrm{d}u_{z_{jrlrm}} \tag{3-14}$$

After integral, normal deformation can be given by:

$$u_{z_{jrlrm}} = e_0 \left[\exp\left(\frac{\sigma_{z_{jrlrm}}}{\lambda + 2G} \right) - 1 \right] \tag{3-15}$$

Denoting $\xi = \dfrac{1}{\lambda + 2G}$, combining Eq.(3-15), fracture aperture is written as:

$$e = e_0 + u_{z_j} = e_0 \exp(\xi \sigma_{z_{jrlrm}}) \tag{3-16}$$

Considering the pore water pressure acting on the fracture surface $\sigma_\mathrm{w} = \gamma_\mathrm{w}\phi$, where ϕ is hydraulic potential on the fracture surface, thus the effective normal stress on the fracture surface is given by: $\sigma_n = \sigma_{z_{jrlrm}} + \gamma_\mathrm{w}\phi$, where tension is positive, pressure is negative.

Then Eq.(3-16) becomes:

$$e = e_0 \exp[\xi(\sigma_{z_{jrlrm}} + \gamma_w \phi)] \tag{3-17}$$

In the Eq.(3-17), relationship between fracture aperture and effective normal stress is found to provide the best fit to the experimental data. And the coupling coefficient ξ can be obtained from experimental tests or numerical back analysis. In the Eq.(3-17), the effect of seepage on the fracture deformation can be shown clearly, and the function of fracture aperture is found to agree the experimental data well.

3.5.2 Effect of normal stress on seepage

3.5.2.1 Equivalent permeability tensor based on FEM

Supposing there are *n* sets of fractures spreading infinitely, where for the set *m*, fracture aperture is e_m , and fracture spacing is b_m, cosine values for included angle between the normal direction and axes *x*, *y*, *z* are denoted as n_x^m , n_y^m, n_z^m respectively. The permeability tensor for rock block is $[K_R]$. 3-D equivalent permeability tensor for fractured rock mass is deduced by Darcy's law:

$$[K]=[K_R]+\sum_{m=1}^{n}\frac{ge_m^3}{12b_m v}\begin{bmatrix}1-(n_x^m)^2 & -n_x^m n_y^m & -n_x^m n_z^m\\ -n_y^m n_x^m & 1-(n_y^m)^2 & -n_y^m n_z^m\\ -n_z^m n_x^m & -n_z^m n_y^m & 1-(n_z^m)^2\end{bmatrix} \tag{3-18}$$

Where v is kinematic viscosity coefficient of fluid.

Substituting Eq.(3-17) into (3-18), the 3-D equivalent permeability tensor for fractured rock mass can be obtained with considering seepage and normal stress coupling based on the FEM:

$$[K]=[K_R]+\sum_{m=1}^{n}\frac{ge_0^3\exp[3\xi_{FEM}(\sigma_{z_{jrlrm}}+\gamma_w\phi)]}{12b_m v}\begin{bmatrix}1-(n_x^m)^2 & -n_x^m n_y^m & -n_x^m n_z^m\\ -n_y^m n_x^m & 1-(n_y^m)^2 & -n_y^m n_z^m\\ -n_z^m n_x^m & -n_z^m n_y^m & 1-(n_z^m)^2\end{bmatrix} \tag{3-19}$$

Where ξ_{FEM} is the coupling coefficient by the FEM.

3.5.2.2 Equivalent permeability tensor based on CEM

The hydraulic conductivity $k_{x_{jrlrm}}$, $k_{y_{jrlrm}}$, $k_{z_{jrlrm}}$ of fracture with aperture *e* are often assumed as constant coefficients, and can be gained from experiments. Fracture transmissivity along the axes x_{jrlrm} , y_{jrlrm} , z_{jrlrm} are denoted as $k_{f_{x_{jrlrm}}}$, $k_{f_{y_{jrlrm}}}$,

$k_{f_{z_{jrlrm}}}$ respectively, according to the Eq.(3-5), it can be written as:

$$\begin{cases} k_{f_{x_{jrlrm}}} = k_{x_{jrlrm}} e = k_{x_{jrlrm}} e_0 \exp[\xi_{CEM}(\sigma_{z_{jrlrm}} + \gamma_w \phi)] \\ k_{f_{y_{jrlrm}}} = k_{y_{jrlrm}} e = k_{y_{jrlrm}} e_0 \exp[\xi_{CEM}(\sigma_{z_{jrlrm}} + \gamma_w \phi)] \\ k_{f_{z_{jrlrm}}} = k_{z_{jrlrm}} / e = k_{z_{jrlrm}} \exp[-\xi_{CEM}(\sigma_{z_{jrlrm}} + \gamma_w \phi)] / e_0 \end{cases} \tag{3-20}$$

Where $k_{f_{z_{jrlrm}}}$ represents the flow exchange capability between the fracture and adjacent rock mass, and it can be gained from experiments. ξ_{CEM} is the coupling coefficient by the CEM.

Combine the Eqs. (3-19)(3-20), it can be obtained that:

$$\xi_{CEM} = 3\xi_{FEM} \tag{3-21}$$

Substituting Eq.(3-20) into Eq.(3-5), it can be seen that the change of normal stress acting on the fracture surface results in the change of fracture transmissivity, which leads to the alteration of seepage field. It also can be seen that fracture transmissivity $k_{f_{jrlrm}}$ is the only one parameter in the conductivity matrices $[h]_{rlrl}$, $[h]_{rlrm}$, in which fracture aperture is implicit. Therefore, the CEM model can be used for both filled and non-filled fracture during the calculation program for seepage and normal stress coupling.

3.5.3 Process of seepage and normal stress coupling analysis

Assume that there is an alteration to the boundary at one certain time (e.g. excavation, reservoir storage). Seepage and normal stress iteration can be evaluated by the following processes (see Fig.3.2):

(1) Calculating the initial stress field $\{\sigma\}^{(0)}$ and initial seepage field $\{\phi\}^{(0)}$ respectively;

(2) Generating the stiffness matrix;

(3) Calculating the initial fracture transmissivity $k_{f_{x_{jrlrm}}}{}^{(0)}$, $k_{f_{y_{jrlrm}}}{}^{(0)}$, $k_{f_{z_{jrlrm}}}{}^{(0)}$ under the initial stress field, according to the Eq.(3-20), then generating the conductivity matrix;

(4) Solving the new seepage field, with the changed seepage boundary condition;

(5) Calculating the increment of seepage load $\{\Delta F\}_{rl}^{(i+1)}$ and obtaining the new hydraulic potential ϕ;

(6) Solving the new stress field with the changed stress boundary condition and the new increment of seepage load, then obtaining the new stress field $\{\sigma\}_{rl}^{(i+1)} = \{\sigma\}_{rl}^{(i)} + \{\Delta\sigma\}_{rl}^{(i)}$;

(7) If it does not satisfy the convergence precision of seepage and stress field, calculating fracture aperture *e* according to the Eq.(3-17), and then obtaining the new transmissivity $k_{f_{x_{j_{rlrm}}}}$, $k_{f_{y_{j_{rlrm}}}}$, $k_{f_{z_{j_{rlrm}}}}$.

(8) Repeating the process (3)~(7), until satisfying the convergence precision of seepage and stress field.

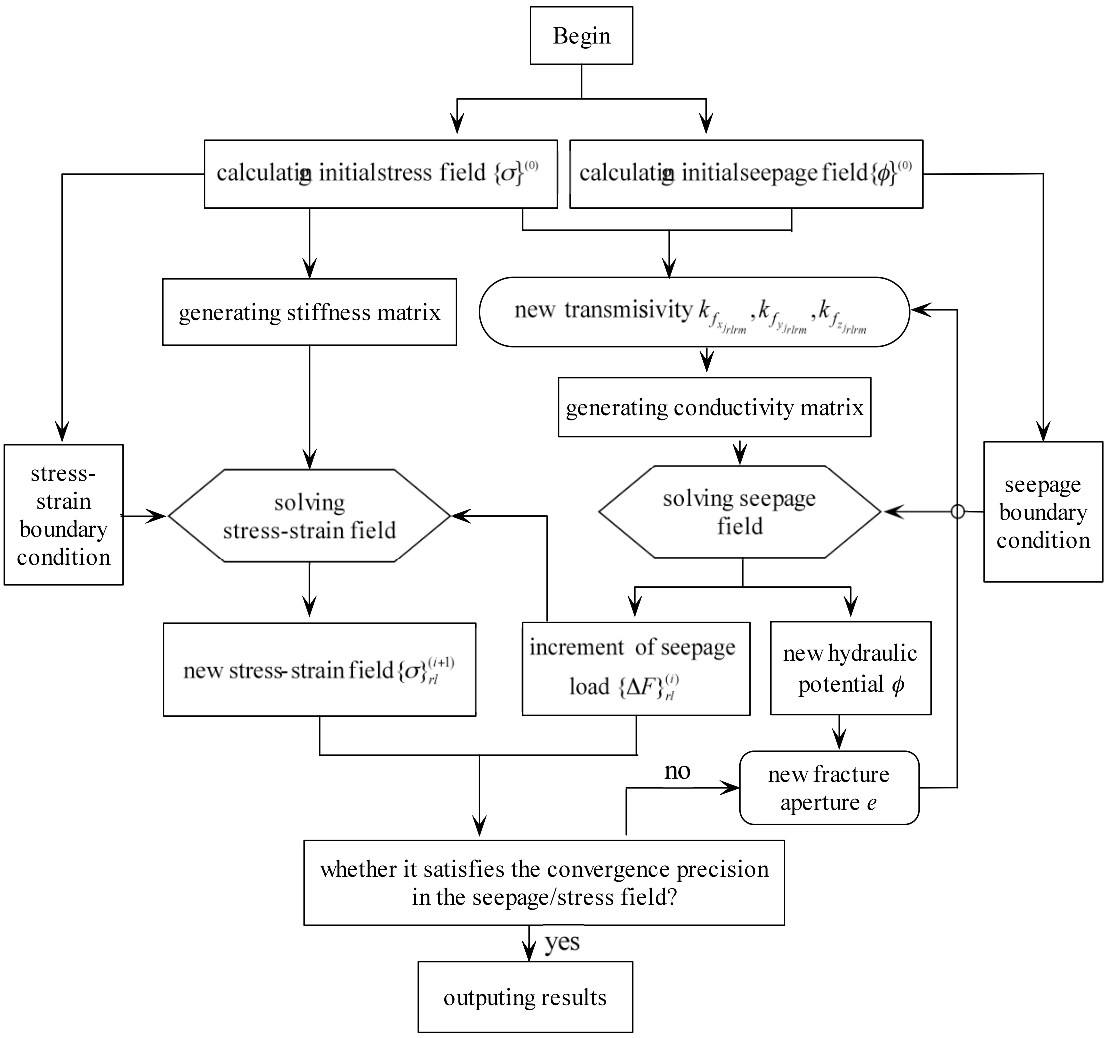

Fig.3.2 Flow chart for the seepage and stress coupling analysis

3.5.4 Numerical verification

3.5.4.1 Computation conditions

There are two numerical models having same size: *x*=0.5m, *y*=0.1m, *z*=0.2m. The first model is composite element model, with 4896 nodes and 3750 elements, of which 250 are composite elements containing one horizontal fracture with original aperture e_0 =0.001m lies at the position *z*=0.1m, (see Fig.3.3(a) the dashed line). Another model is finite element model, with 5508 nodes and 4250 elements, containing 250 fracture elements with 0.001m in thickness (Fig.3.3(b)), in this way, fractured rock mass is simulated discretely with fracture elements.

Both the models have the same boundary conditions and load. Water level is 10.0m at left, 5.0m at right, and there is no flow exchange with external system for the other boundaries. Concentrated force *F* (Fig.3.3) and seepage load are considered, weight of rock mass is neglected. The computation parameters of the two models are given in the Tab.3.1~3.3.

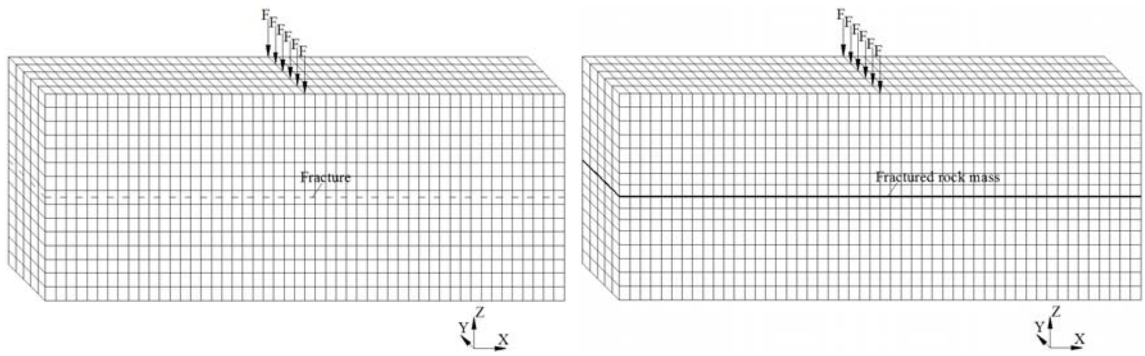

(a) Mesh of CEM **(b) Mesh of FEM**

Fig.3.3 Computaion meshes

Tab.3.1 Parameters of rock mass

Young's modulus *E*/MPa	Poisson's ratio ν	Volumetric weight γ/(kN·m^{-3})	k_{rl}/(m·s^{-1})
5 000	0.32	24	1.0×10^{-5}

Tab.3.2 Parameters of fractures for the CEM

φ_j/(°)	θ_j/(°)	e_0/m	Normal stiffness k_n/(MPa·m^{-1})	Shear stiffness k_s/(MPa·m^{-1})	ξ	$k_{j_{rl,rm}}$ /(m·s^{-1})
0	0	0.001	5 000	3 000	changeable	0.5382

Tab.3.3 Parameters of fractures for the FEM

φ_j /(°)	θ_j /(°)	e_0/m	b/m	Normal stiffness k_n/(MPa·m^{-1})	Shear stiffness k_s/(MPa·m^{-1})	ξ
0	0	0.001	0.001	5 000	3 000	changeable

3.5.4.2 Computation results

Rock mass and fractures are treated as elastic media, and three cases are considered as follows.

Case 1 Without considering the seepage and normal stress coupling, that is $\xi = 0$;

Case 2 Considering the coupling, with concentrated force F=-0.004MN;

Case 3 Considering the coupling, with concentrated force F=-0.02MN;

Fig.3.4 shows hydraulic potential contour at the vertical section *x-o-z*. The hydraulic potentials obtained from the CEM agree exactly with those obtained from the FEM. When considering the coupling mechanism, as the concentrated force increases, the hydraulic potential contour lines concentrate gradually to the zone on which the concentrated forces act. The hydraulic potential of the upstream zone has tendency to approach the upstream water level, and that of the downstream zone has tendency to approach the downstream water level.

The hydraulic potential along the fracture as a function of concentrated force is shown in the Fig.3.5, in which the results obtained by the CEM and the FEM give nearly the identical hydraulic potential.

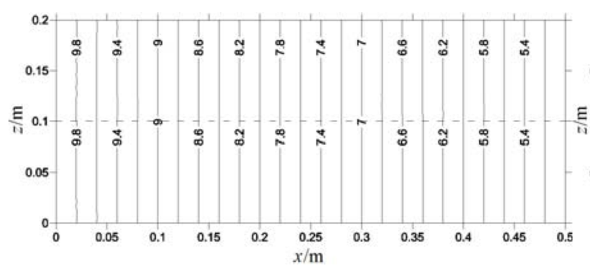

By CEM

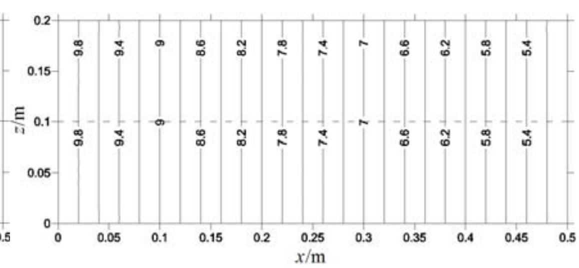

By FEM

(a) $\xi = 0$

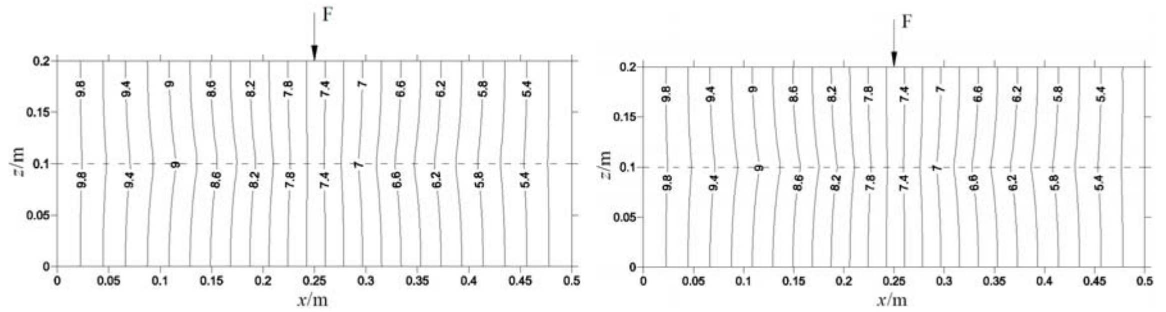

By CEM By FEM

(b) F= -0.004MN

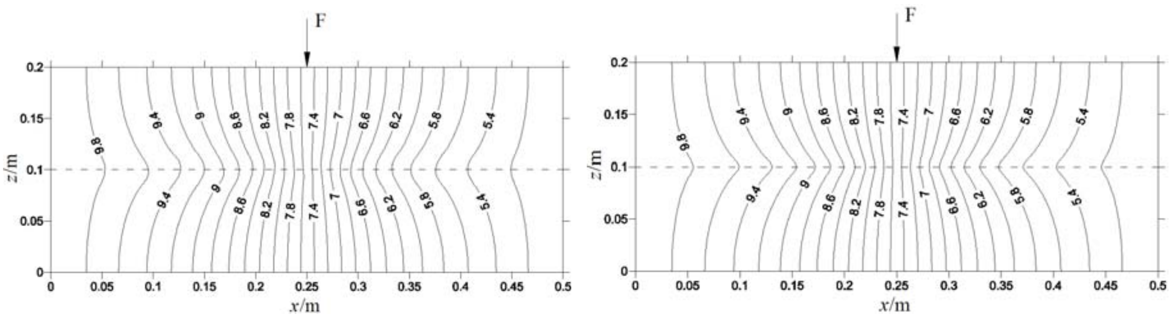

By CEM By FEM

(c) F= -0.02MN

Fig.3.4 Hydraulic potential contour

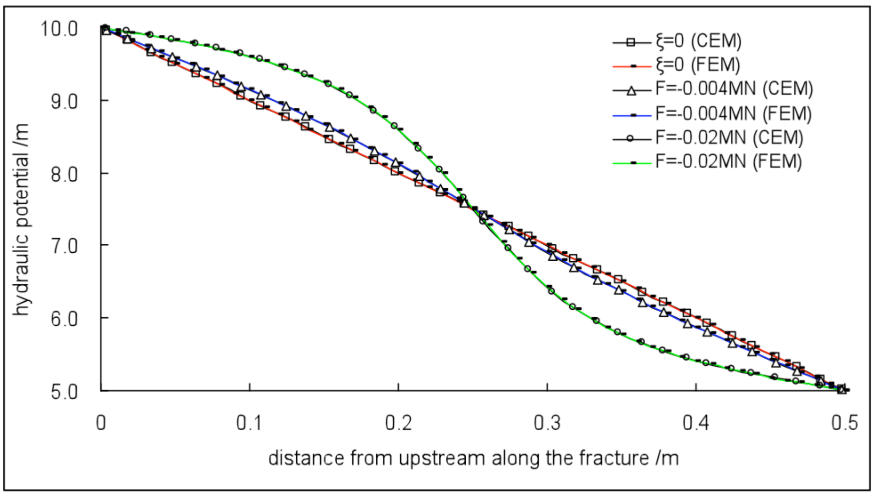

Fig.3.5 Hydraulic potential along the fracture as a function of concentrated force

The flow rate per unit width through the fracture by the CEM is given by:

$$q_C = V_C \bullet e \tag{3-22}$$

The flow rate per unit width through the fractured rock mass by the FEM is given by:

$$q_F = V_F \bullet b \tag{3-23}$$

Because the permeability coefficient of the intact rock is far less than that of the fracture, and the flow of the intact rock can be ignored, it can be obtained:

$$q_C = q_F \tag{3-24}$$

Then combining Eqs.(3-22)~(3-24), it is written as:

$$V_C / V_F = b / e \tag{3-25}$$

Where V_C represents the seepage velocity along the fracture by CEM, V_F represents Darcy velocity through the fractured rock mass by FEM, and b is denoted as width of fractured rock mass.

Generally, magnitude of actual seepage velocity along the fracture is much higher than that of Darcy velocity for equivalent continuum medium, because the magnitude of width of fractured rock mass is much higher than that of fracture aperture, except the fracture simulated discretely by fracture element (see Fig.3.3). For the equivalent continuum medium, only when $b = e$ the actual seepage velocities along the fracture can be obtained. In that case, it is very difficult for the mesh generation with density increasing, especially for the model with complicated configuration. However, the seepage velocities along the fractures by CEM are obtained more easily.

In order to compare the computation results conveniently, for the FEM, all the equivalent seepage velocities through the fractures have been given in this paper:

$$V_F^{'} = V_F \bullet b / e \tag{3-26}$$

Fig.3.6 shows seepage velocity vector at the vertical section *x-o-z* with different computational conditions. It can be seen that, the results based on the CEM and the FEM are agreed with each other. When considering the coupling, in the zone on which the concentrated forces act, seepage velocities along the fracture increase as the increase of concentrated force, the main reason is that the seepage gradient increases, which is indicated in the Fig.3.5. Nevertheless the seepage velocities decrease in the other zone.

From the Fig.3.7, it is shown that, the CEM and the FEM give nearly the same seepage velocities along the fracture under the same concentrated force.

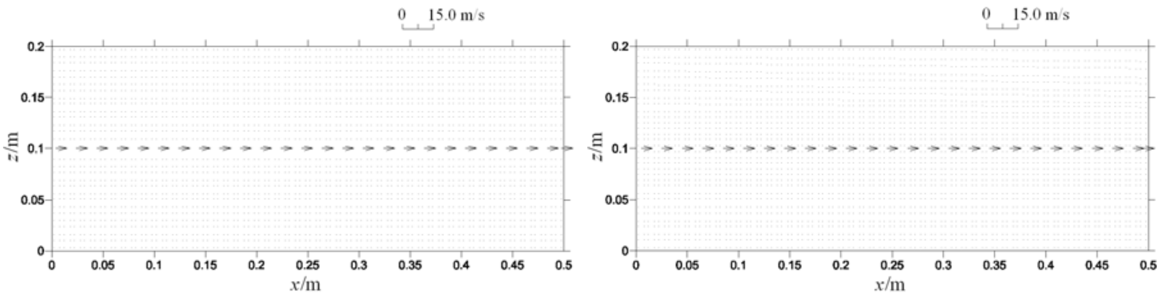

By CEM By FEM

(a) $\xi = 0$

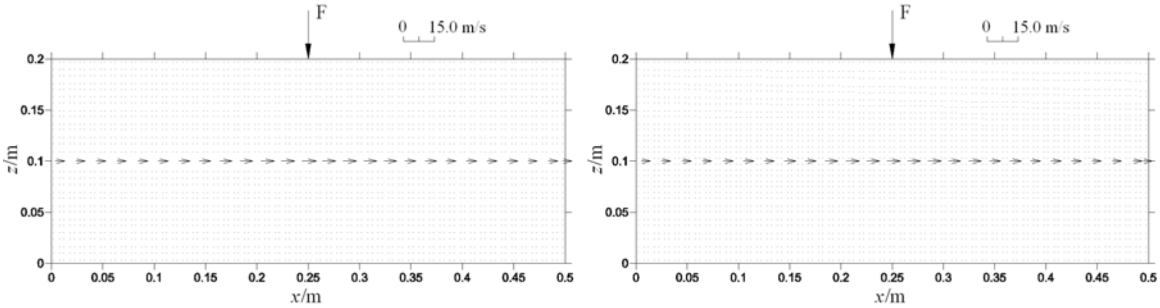

By CEM By FEM

(b) F= -0.004MN

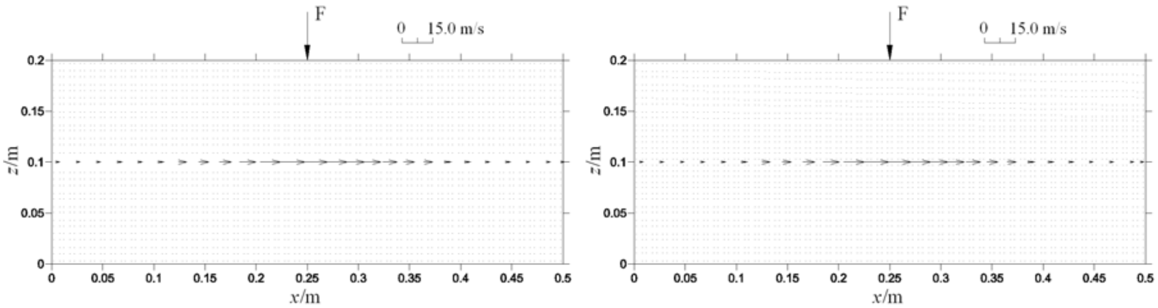

By CEM By FEM

(c) F= -0.02MN

Fig.3.6 Seepage velocity vector

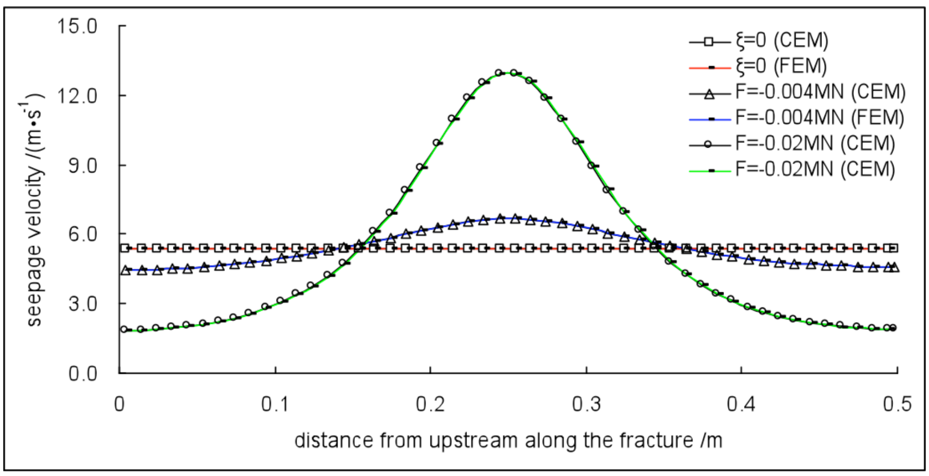

Fig.3.7 Seepage velocity along the fracture as a function of concentrated force

The flow rate of the fracture per unit width (along *y* direction) as a function of concentrated force is shown in the Fig.3.8. Again, it can be found that CEM and FEM close to each other. As the increase of concentrated force *F*, the flow rate per unit width reduces with exponential decrease. Fig.3.9 shows the effective normal stress on the fracture by the two methods, which give nearly the identical values.

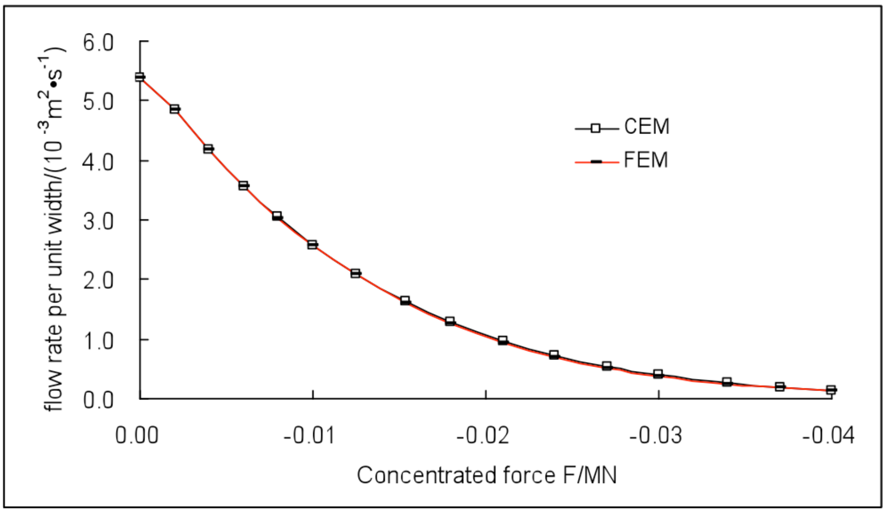

Fig.3.8 Flow rate per unit width of the fracture as a function of concentrated force

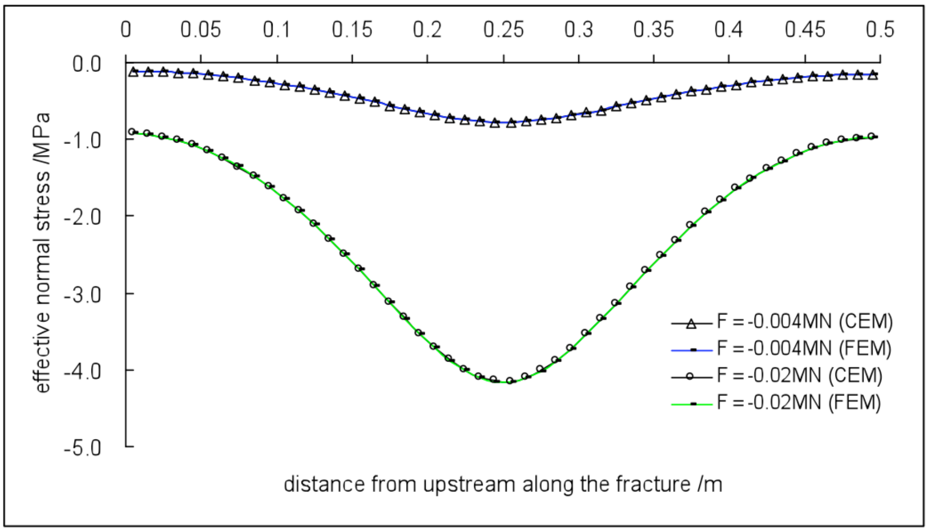

Fig.3.9 Effective normal stress along the fracture

3.6 Seepage and stress coupling mechanism during the shear process

Stress plays an important role in the fracture deformation and the variety of fracture roughness, which further leads to the change of permeability characteristics of rock fractures. So far, there have been many researches on the seepage and normal stress coupling, but a few researches on the seepage and stress coupling during the shear process. The main reason is that fracture deformation dependent on the shear stress is more complicated than that dependent on the normal stress. And it is also very difficult to take experiment during the shear process.

Recently, some scholars have done some researches on the seepage and stress coupling during the shear process for rock fractures: Barton(1976), Barton, Choubey(1977) have proposed fracture roughness coefficient (JRC), and fracture shear strength has relationship with friction angel φ, JRC, fracture compressive strength (JCS), and the normal stress σ_n acted on the fracture surface; Bandis, Lumsden, Barton(1981) have presented that the relationship between fracture shear strength and shear deformation depends on the size of fracture; Barton, Bandis(1982) have analyzed on 650 groups data on the shear tests, and given the empirical equation of peak shear deformation under the peak shear strength; Barton, Bandis, Bakhtar(1985) have built dimensionless model for shear stress-displacement modeling, according to the results on the fracture characteristics for several years; Olsson, Barton(2001) have presented an improved model of seepage and stress coupling during the shear process for rock fractures.

Based on the theories listed above, the seepage and stress coupling for rock fractures during the shear process has been taken into consideration. According to the mechanism of rock fractures during the shear process, combining the fracture shape, the relationship between shear stress and shear deformation has been built firstly, with considering the different levels of normal stress. The relationship between shear stress and shear deformation is divided into three phases: shear shrink, shear dilation up to peak value, residual shear strength. Then, with the application of the composite element algorithm, the coupling mechanism of seepage and stress for rock fractures during the shear process is carried out, by which the variation and relationship among shear deformation, fracture aperture, conductivity of rock fracture, seepage field as well as stress field are illustrated.

3.6.1 Shear process of rock fracture

When rock fractures are not acted by outer loads, the asperities of fracture surface can be classified into the following three conditions, see Fig.3.10. Fig.3.10(a) shows the steady balance condition of fracture, Fig.3.10(b)~(c) show the unsteady balance condition of fracture. Generally, natural fracture is under the condition of steady balance (Fig.3.10 (a)), because it is acted by the geo-stress for a long time.

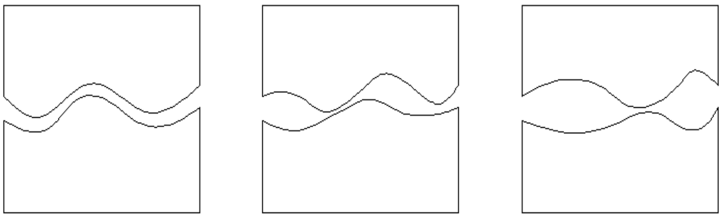

(a) (b) (c)

Fig.3.10 Sketch of initial states of rock fracture

When the fracture is under the condition of initial steady balance, see Fig.3.11(a), at the beginning of the shear process, there is not relative slide because of the friction action between the up and down fracture surfaces. But the shear stress leads to the shear deformation, therefore, the fracture is shrunk, see Fig.3.11(b), the dashed lines show the condition before deformation. With the increase of shear loads, there is relative slide between the fracture surfaces, and the fracture slides along the asperity. But the increment of aperture resulting from the slide is still smaller than the decreased value resulting from the initial shear shrink. That is the recent fracture aperture is still smaller than the initial one, under the shear shrink condition, see Fig.3.11(c). The shear loads keep increasing, as well as the slide of fracture. When the fracture aperture is bigger than the initial one, shear dilation begins until up to the peak value, see Fig.3.11(d). Then, the fracture begins to be yielded, even be destroyed, and the fracture is still in the shear dilation condition. This phase is residual shear strength, see Fig.3.11(e)~(f).

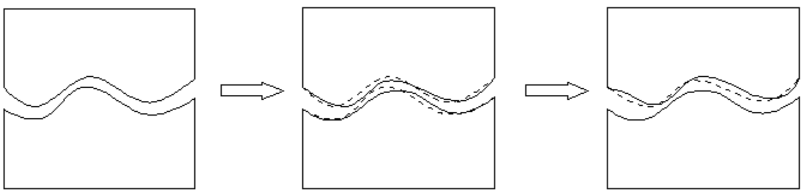

(a) (b) (c)

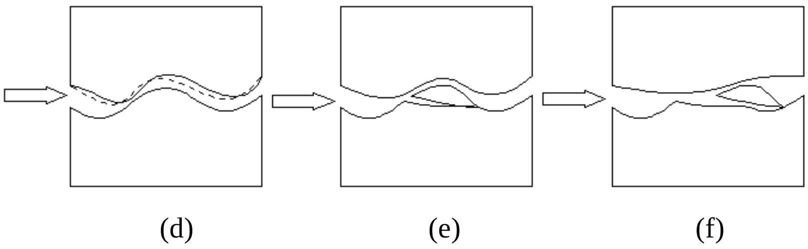

Fig.3.11 Fracture deformation during the shear process

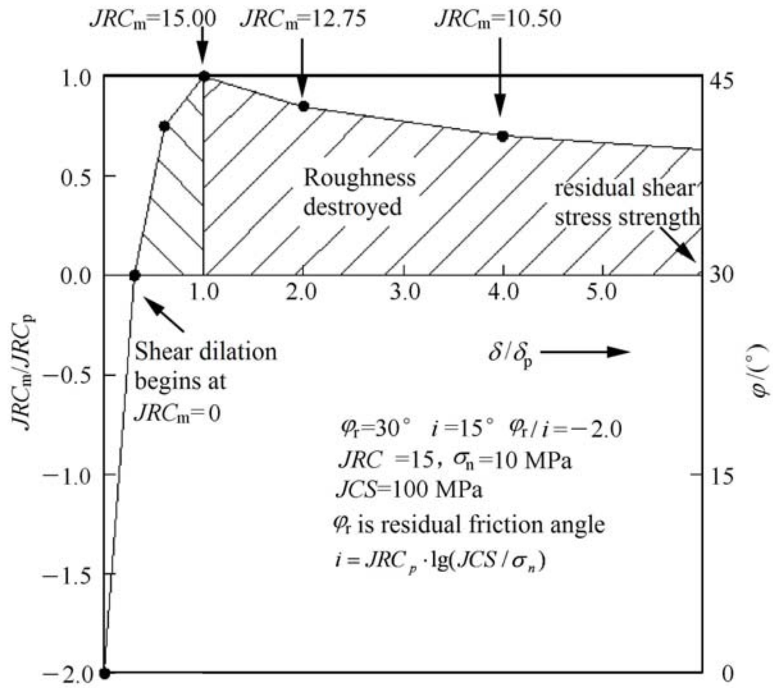

Fig.3.12 Curve of shear stress vs. shear deformation without relation with dimension

Fig.3.12 shows the curve of shear stress vs. shear deformation without relation with dimension (Barton, Bandis, Bakhtar, 1985), where δ is shear deformation, φ is friction angel, and φ_r is friction angle under the residual shear strength, and the subscript *m*, *p*, *r* represent variable value, peak value and residual value respectively. It can be seen in the Fig.3.12, when $0<\delta/\delta_p<0.3$, $JRC_m/JRC_p\leqslant 0$, it is the shear shrink phase, and the friction angel increases; when $0.3<\delta/\delta_p<1$, it is the shear dilation phase, and JRC keeps increasing, until up to the peak value when $\delta=\delta_p$; when $\delta/\delta_p>1$, fracture asperity begins to be yielded even to be destroyed, JRC decreases to zero. The relevant shear stress is residual shear strength, in the residual shear strength phase.

3.6.1.1 Shear shrink phase

Shear shrink phase indicates that shear deformation of rock fracture leads to the decrease of fracture aperture, and the change of aperture is related not only with normal stress, but also with shear stress. In this dissertation, only under the same level normal stress, the relationship between shear deformation and shear stress is taken into consideration.

Shear deformation can lead to the change of normal deformation, and it can be obtained that:

$$\Delta e = \Delta\delta \tan d_{\mathrm{nm}} \tag{3-27}$$

Where Δe is the increment of fracture aperture, $\Delta\delta$ is the increment of shear deformation, and d_{nm} is changeable dilation angle, and

$$d_{\mathrm{nm}} = \frac{1}{M} JRC_{\mathrm{m}} \lg(JCS/\sigma_{\mathrm{n}}) = \frac{1}{M} JRC_{\mathrm{m}} \lg[JCS/(\sigma_{z_{jrlrm}} + \gamma_{\mathrm{w}}\phi) \tag{3-28}$$

Where M is destroy coefficient, and is equal to 2 and 1 respectively when shear stress is under high and low normal stress.

According to the Fig.3.12, when $0 < \delta/\delta_{\mathrm{p}} < 0.3$, the relationship between $JRC_{\mathrm{m}} / JRC_{\mathrm{p}}$ and $\delta_{\mathrm{m}}/\delta_{\mathrm{p}}$ can be given by:

$$JRC_{\mathrm{m}} = JRC_{\mathrm{p}} \times (\phi_{\mathrm{r}}/i) \times (10\delta/3\delta_{\mathrm{p}} - 1) \tag{3-29}$$

Substituting the Eqs.(3-28)(3-29) into eq.(3-27), it can be obtained that:

$$\Delta e = \Delta\delta \tan\left\{\frac{1}{M} JRC_{\mathrm{p}}(\phi_{\mathrm{r}}/i)(10\delta/3\delta_{\mathrm{p}} - 1)\cdot \lg[JCS/(\sigma_{z_{jrlrm}} + \gamma_{\mathrm{w}}\phi)]\right\} \tag{3-30}$$

Increment of fracture aperture resulting from normal stress is given by:

$$\Delta e = e_0 \exp[\xi(\sigma_{z_{jrlrm}} + \gamma_{\mathrm{w}}\phi)] \tag{3-31}$$

Combining the Eqs.(3-30)(3-31), when the normal stress keeps constant, it can be obtained that:

$$e = e_0 \exp[\xi(\sigma_{z_{jrlrm}} + \gamma_{\mathrm{w}}\phi)] + \Delta\delta \tan\left\{\frac{1}{M} JRC_{\mathrm{p}}(\phi_{\mathrm{r}}/i)(10\delta/3\delta_{\mathrm{p}} - 1)\lg[JCS/(\sigma_{z_{jrlrm}} + \gamma_{\mathrm{w}}\phi)]\right\} \tag{3-32}$$

3.6.1.2 Shear dilation up to peak value phase

According to the Fig.3.12, it can be seen that, shear dilation begins when the shear deformation is up to 30% of the peak value, that is $\delta/\delta_{\mathrm{p}} = 0.3$. With the increase of shear deformation, JRC keeps increasing, and when $\delta/\delta_{\mathrm{p}} = 1$, JRC is up to the peak value JRC_{p}. At the same time, the shear stress τ is also up to the peak shear strength τ_p.

Barton, Bandis, Bakhtar(1985) has proposed fracture roughness coefficient (*JRC*), and fracture shear strength has relationship with friction angel φ, *JRC*, fracture compressive strength (*JCS*), and the normal stress σ_n acted on the fracture surface. The peak value of shear strength can be obtained by:

$$\tau_{\mathrm{p}} = (\sigma_{z_{jrlrm}} + \gamma_{\mathrm{w}}\phi)\tan\{JRC_{\mathrm{p}}\lg[JCS/(\sigma_{z_{jrlrm}} + \gamma_{\mathrm{w}}\phi)] + \varphi_{\mathrm{r}}\} \tag{3-33}$$

Where *JCS*, φ_{r}, JRC_p can be obtained by the shear experiments of rock fractures.

Barton, Bandis(1982) have proposed the empirical equation of the peak shear deformation, according to 650 groups of shear tests data:

$$\delta_{\mathrm{p}} = \frac{L_{\mathrm{n}}}{500}\left(\frac{JRC_{\mathrm{p}}}{L_0}\right)^{0.33} \tag{3-34}$$

Where L_n is the field-scale length, and L_0 is the laboratory-scale fracture sample length, generally $L_n = L_0$, and in the Eq.(3-34), the units of L_n, L_0, and δ_p are meters.

According to the Fig.3.12, when $0.3 \leqslant \delta/\delta_{\mathrm{p}} < 1$, it can be obtained that:

$$JRC_{\mathrm{m}} = JRC_{\mathrm{p}}[1.13(\delta/\delta_{\mathrm{p}} - 0.3)^{0.34}] \tag{3-35}$$

Combining the Eqs.(3-31), (3-28), (3-31), (3-35), it can be obtained that:

$$e = e_0\exp[\xi(\sigma_{z_{jrlrm}} + \gamma_{\mathrm{w}}\phi)] + \Delta\delta\tan\left\{\frac{1}{M}JRC_{\mathrm{p}}[1.13(\delta/\delta_p - 0.3)^{0.34}]\lg[JCS/(\sigma_{z_{jrlrm}} + \gamma_{\mathrm{w}}\phi)]\right\} \tag{3-36}$$

3.6.1.3 Residual shear strength phase

According to the Fig.3.12, when $\delta/\delta_{\mathrm{p}} > 1.0$, as the increase of shear deformation, shear stress decrease until the residual shear strength, and the asperity is yielded or destroyed.

Also based on the Fig.3.12, when $\delta/\delta_{\mathrm{p}} > 1.0$, it can be obtained that:

$$JRC_{\mathrm{m}} = JRC_{\mathrm{p}}[1.000\ 4 - 0.217\ 2\ln(\delta/\delta_{\mathrm{p}})] \tag{3-37}$$

Substituting the Eqs.(3-28), (3-31), (3-37) into eq.(3-27), it can be obtained that:

$$e = e_0 \exp[\xi(\sigma_{z_{jrlrm}} + \gamma_{\mathrm{w}}\phi)] - \Delta\delta \tan\{\frac{1}{M} JRC_{\mathrm{p}}[1.0004 - 0.2172\ln(\delta/\delta_p)]\lg[JCS/(\sigma_{z_{jrlrm}} + \gamma_{\mathrm{w}}\phi)]\} \tag{3-38}$$

3.6.2 Process of the coupling analysis during shearing

Substituting the Eqs.(3-32)(3-36)(3-38) for Eq.(3-20), it can be seen that, the change of stress on the fracture surface leads to the change of fracture aperture, which further leads to the change of permeability conductivity, as well as the seepage field; on the other hand, the changed seepage loads leads to the change of stress field inversely. The interaction between the seepage and stress field can be shown obviously. The process of the coupling analysis during the shearing is almost the same to that of for the normal stress coupling analysis, see the Fig.3.2. The only difference is that, evaluating the value of $\delta/\delta_{\mathrm{p}}$ before calculating the new fracture aperture *e* according to the Eqs. (3-32)(3-36)(3-38), due to different levels of $\delta/\delta_{\mathrm{p}}$ having different fracture apertures during shear process.

3.6.3 Numerical verification

3.6.3.1 Computation conditions

Fig.3.13(a) shows one rock block containing 10 composite elements, having the size: *x*=1.0m, *y*=0.1m, *z*=3.0m. There is one horizontal fracture with aperture *e*=0.001m locating at the position z=1.05m. Water level is 10.0m at left, 5.0m at right, and there is no flow exchange with external system for the other boundaries. The concentrated force F_x at the *x*-direction and the top normal surface force σ_n have been taken into consideration, and the weight of rock mass is neglected.

There are 10 composite elements containing the fracture, and the composite element ◯,5 is located in the middle, see Fig.3.13(c). For the element ◯,5, there are three cases with normal stress σ_n is equal to 0.5, 1.0, and 5.0 MPa respectively. Parameters for rock mass and fracture are shown in the Tabs.3.4~3.5 respectively.

Concerning the composite element ◯,5, under the three different levels of normal stress, the variables of fracture aperture, shear stress, seepage velocity and flow per unit width along the fracture as a function of shear deformation have been analyzed respectively. The concentrated force F_x keeps linear increasing until shear stress to τ_p, after then the shear stress is considered as residual shear strength τ_r. In order to make the normal stress σ_n keep constant, there is a surface stress (see Fig.3.13(b)) to balance the increment of normal stress resulting from the shear loads,.

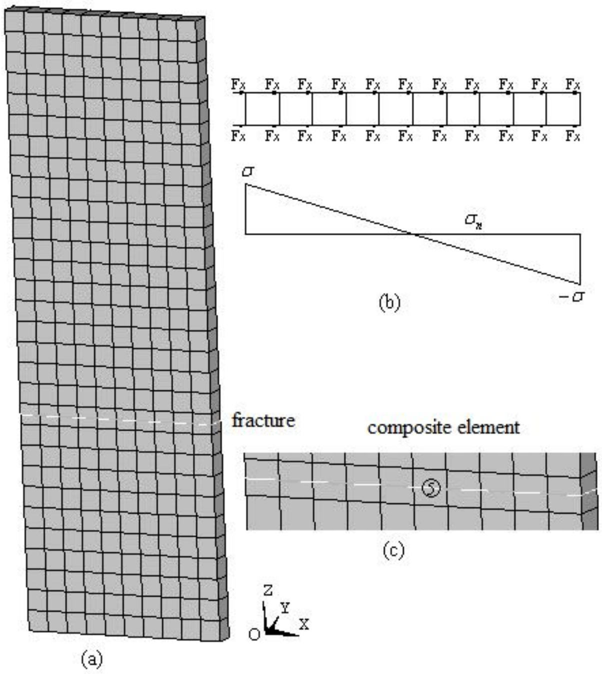

Fig.3.13 Mesh of composite element method

Tab.3.4 Physico-mechanical parameters of rock mass

Young's modulus E/MPa	Poisson's ratio ν	Volumetric weight γ/(kN·m^{-3})	k_{rl}/(m·s^{-1})
14 000	0.28	25	1.0×10^{-8}

Tab.3.5 Geometrical and mechanics parameters of fracture

Normal stiffness k_{n}/(MPa·m^{-1})	Shear stiffness k_{s}/(MPa·m^{-1})	JRC_p	JCS /MPa	φ_r /($^{\mathrm{o}}$)	$k_{j_{rlrm}}$ /(m·s^{-1})
10 000	448	8	200	53.47	1.0×10^{-5}

3.6.3.2 Computation results

Rock mass and fracture are considered as elastic media, and the mechanics parameters of rock mass and the “filled” medium in the fracture keep constant.

Fig.3.14 shows the fracture aperture as a function of shear deformation for the composite element ◯,5. It can be seen that, when $0 < \delta/\delta_p < 0.3$, the fracture is in the shear shrink phase, after the fracture aperture decreases to the minimum one, it begins to increase back to the initial value. When $\delta/\delta_p = 0.3$, the shear dilation begins, and when $\delta/\delta_p > 1.0$, the fracture aperture increases gently. It can also be seen that, the normal stress is smaller, the effect of shear dilation is bigger, which agrees with the empirical curve by Barton, Bandis(1985), Olsson, Barton(2001).

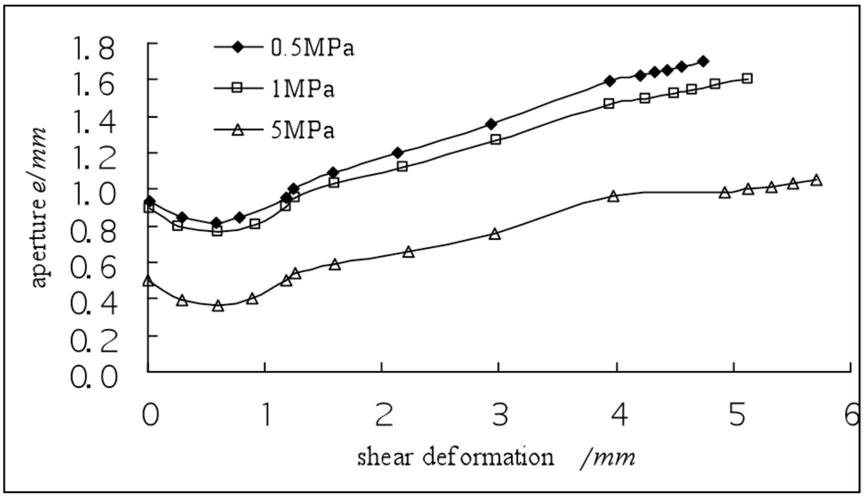

Fig.3.14 fracture aperture as a function of shear deformation

Fig.3.15 shows shear stress vs. shear deformation for the composite element ◯,5. Fig.3.16 shows seepage velocity along the fracture as a function of shear deformation, and Fig.3.17 shows flow per unit width along the fracture as a function of shear deformation.

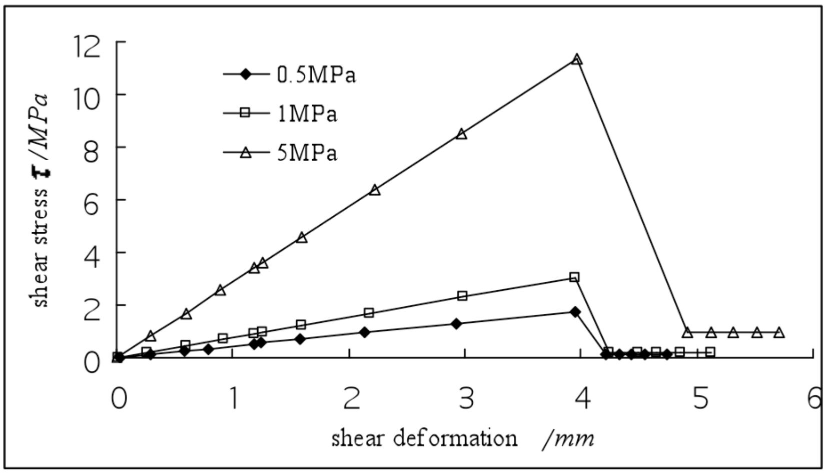

Fig.3.15 Shear stress vs. shear deformation on the fracture

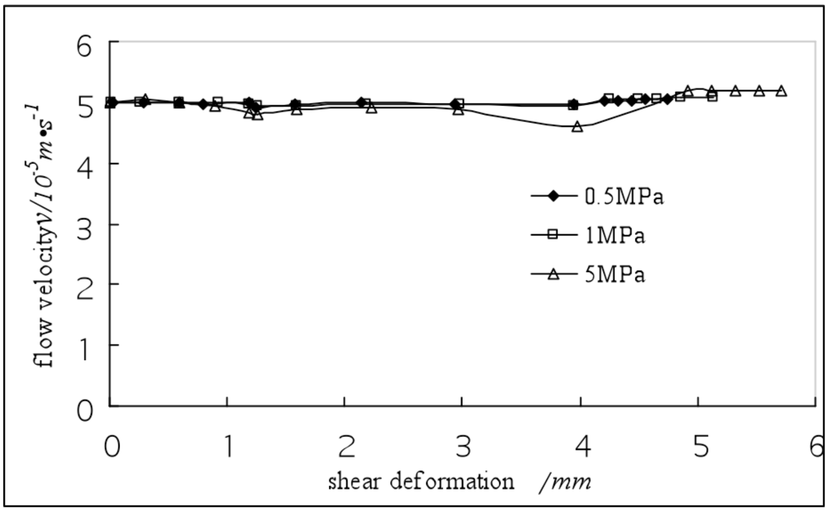

Fig.3.16 Seepage velocity along the fracture as a function of shear deformation

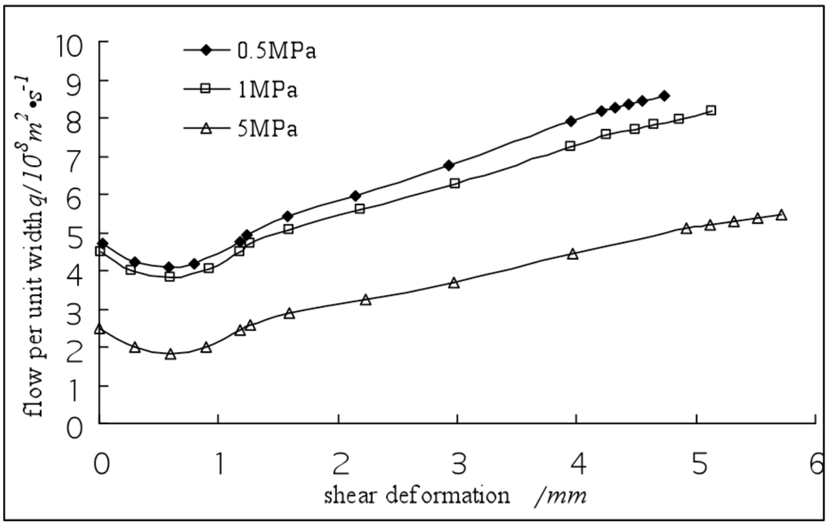

Fig.3.17 Flow per unit width along the fracture as a function of shear deformation

In the Fig.3.16, it can be seen that, the seepage velocity almost keeps stable, even if the shear deformation and the normal stress are changed, but the flow per unit width changes because of the change of fracture aperture, see Fig.3.17.

The curves shape in the Fig.3.17 is similar to that in the Fig.3.14, the bigger the normal stress is, the smaller the fracture aperture and flow per unit width are, but the seepage velocities are almost not influenced by the normal stress. Therefore, it is indicated that, the flow per unit width along the fracture is more dependent on the fracture aperture during the shear process.

When the normal stress $\sigma_n = 1.0MPa$, the shear deformation of the composite element ◯,5 $\delta / \delta_p = 0.3$, the aperture along the fracture is shown in the Fig.3.18. Because of the uneven distribution of shear stress, the shear stress at the two ends of the fracture is equal to zero, and at the middle of the fracture it is up to the peak value. Therefore, the shear deformation at the middle part is the biggest one, when the fracture shear dilation in the composite element ◯,5 begins, the fracture segments at the two ends is still in the shear shrink phase, that is the aperture of the two ends is much smaller than that of the other parts, which can be verified in the Fig.3.18.

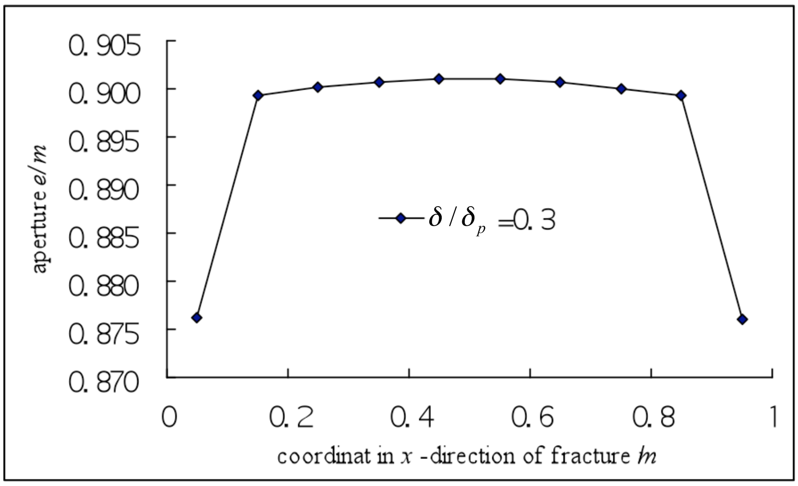

Fig.3.18 aperture along the fracture ($\delta / \delta_p = 0.3$)

3.7 Summary of the chapter

Based on the CEM, the seepage and stress coupling algorithm of fractured rock mass has been proposed, which is an important extension for the CEM. The coupling mechanism has been carried out by applying the iterative algorithm between the seepage and stress field. The proposed coupling algorithm has been verified by one simple numerical example, by comparison with the FEM, the brief conclusion is shown that:

(1) The results of the proposed coupling algorithm agree exactly with those obtained by FEM, where the reliability and advantages of the algorithm are well verified.

(2) The proposed coupling algorithm has the advantages of simplicity in the preprocess work. Because the existence of the fractures is not taken into consideration in the computation mesh generation, but it will be simulated

explicitly in each composite element. In addition, the coupling algorithm considers not only the flow in the fractures, but also the flow exchange between the fractures and the adjacent rock mass, and it also can be used for both the filled and non-filled fractures.

(3) The proposed coupling algorithm emphasizes on the detailed characteristics of fractures better than the FEM. The obtained seepage velocities of the fractures by the CEM are much closer to the actual ones.

(4) The uneven hydraulic behavior of fractured rock mass resulting from the stress is remarkable when considering the seepage and stress coupling. Therefore, the importance of the coupling analysis for fractured rock mass is emphasized.

Chapter 4 Seepage and stress coupling for fractured rock mass containing drainage holes

Fractures (faults, joints, etc.) dominate the seepage and stability of rock mass. To improve the stability of rock mass, drainage technique is widely used. The seepage and stress coupling analysis for the rock mass containing both fractures and drainage holes is essential for the design of drainage system.

The finite element method (FEM) (Zienkiewicz, Mayer, Cheung, 1966) is a popular tool for seepage and stress analysis. Nowadays, the models proposed to treat the fractures can be classified into two catalogues: one is the implicit (equivalent) model which takes the influences of the fractures into the permeability tensor and the stiffness matrix but neglects their exact positions (Barenblatt, Zheltov, Kochina, 1960; Duiguid, Lee, 1977; Streltsova,1976; Long et al. 1982; Dershowitz, et al. 1985; Hsieh, Neuman,1985; Long, Gilmour, Witherspoon,1985; Oda, 1985, 1986); another one is the explicit (distinct) model which uses special elements to simulate exactly the geological and mechanical properties of the fractures (Schwartz, Smith, Crowe, 1983; Andersson, Dverstorp,1987; Dershowitz, Einstein,1987; Cacas et al., 1990). The models proposed to treat the drainage holes can also be classified as implicit and explicit. The former looks at rock mass as equivalent continuous media whose hydraulic conductivity can be decided by the equivalent principle of flow rate which has relationship with the rock conductivity, and with the diameter, orientation and spacing of the drainage holes (Du, Xu, Huang,1984; Guan, Liu, Zhu, 1984; Du, Xu, Han, 1991); The latter includes some well known models such as the point well model, sub-structure model, and semi-analytical model (Zhu,1982; Fipps, Skaggs, Nieber, 1986; Wang, Liu,Z hang, 1992; Wang, Wang, Deng, 2001). Implicit model can be applied to the very complicated engineering problems with a large number of fractures and drainage holes, whereas the explicit model has the potentiality to describe the fractures and drainage holes in much more detail and consequently gives more precise solution.

From the point view of practitioners, main disadvantage of the explicit simulation of fracture and drainage hole systems lies in the pre-process to discrete the calculation domain. This difficulty arises from two aspects:

- Usually there are large quantity of fractures with different sizes, large quantity of drainage holes with small diameter (e.g. 10cm) and deployed within a small width and large stretch zone (e.g. 3m in distance between holes);

- The special elements at hand have definite nodes deployed along the fractures and drainage holes, and some of these nodes should be the common nodes of the nearby surrounding rock elements. This difficulty combined with the complicated configuration of the structures such as dam foundation, rock slope and underground cavern, will make the pre-process work time costly and tedious.

A composite element method (CEM) has been proposed to solve the difficulty discussed above, and has been implemented separately for rock fractures, rock bolts and drainage holes respectively (Chen, Qiang, Chen, 2003; Chen, et al. 2004; Chen, Qiang, 2004; Chen, Xu, Hu, 2004; Chen, Feng, 2006; Chen, et al. 2008; Chen, Feng, Shahrour, 2008; Chen, Shahrour, 2008). The most remarkable feature of this method is to locate the fractures, or bolts, or drainage holes within the elements. In this way less restraints is imposed on the mesh generation for complicated rock structures with considerable number of fractures, bolts and drainage holes.

This chapter presents the comprehensive formulation of the composite element model for the seepage and stress coupling analysis in the rock mass containing both fractures and drainage holes. Since the fractures and drainage holes are all embedded within the elements, they can be simulated explicitly without special elements deployed along them. The algorithm is verified by a numerical example firstly, and then it is applied to the Baozhusi gravity dam located on a complicated rock foundation. The comparative study using both the FEM and CEM is presented.

4.1 Hydraulic potential in sub-elements

Firstly, the FE mesh should be generated to discrete the structure concerned firstly. The deployment and sizes of the finite elements are dependent on the structure configuration and flow rate gradient. Then the presence of fractures and drainage holes transfers some finite elements into composite elements through geometrical computation.

Fig.4.1 shows a composite element containing n_r rock sub-elements, n_d drainage sub-elements and n_j fracture sub-elements.

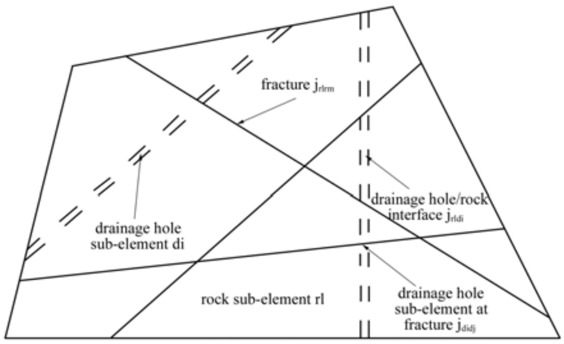

Fig.4.1 Composite element containing discontinuities and drainage holes

The local coordinate system for the fracture segment is also the same, see Fig2.2. For the drainage a Cartesian local system is needed to simplify the deduction. It is defined as follows (Fig.4.2a): the z_d-axis is along the drainage hole and upright, the y_d-axis is perpendicular to the drainage hole and points in the direction of dip and the x_d-axis is formed by the right hand rule. On the basis of the local Cartesian coordinate system, the local Cylindrical coordinate system is further defined (Fig.4.2b). The subscript j_{rldi} will be used to indicate the interface sub-element between rock sub-element rl and drainage sub-element di, the subscripts j_{didj} will be used to indicate the drainage at their intersecting point on the fracture sub-element j_{rlrm}. If necessary, the superscripts ca or cy are used to denote the quantity in the Cartesian or Cylindrical local coordinate system.

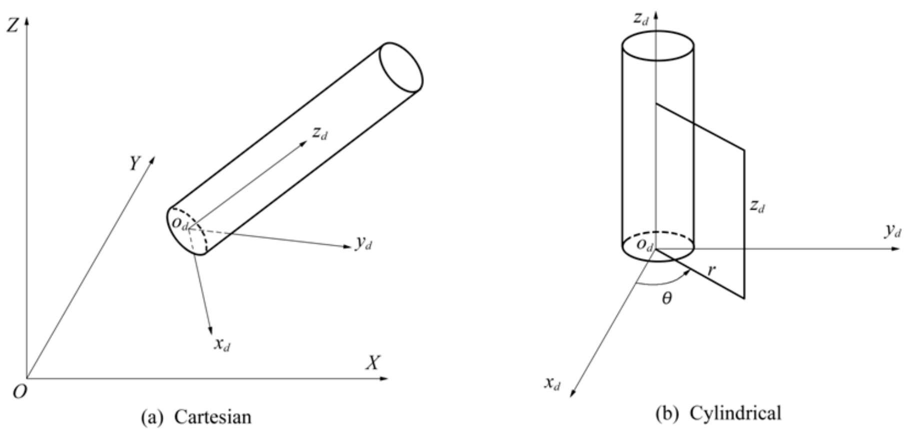

Fig.4.2 Local coordinate system of drainage

There are independent nodal hydraulic potentials for rock and drainage hole sub-elements denoted as $\{\phi\} = [\ \{\phi\}_{r1}, \{\phi\}_{r2}, \ldots.\ \{\phi\}_{nr}, \{\phi\}_{d1}, \{\phi\}_{d2}, \ldots\ldots \{\phi\}_{nd}\ ]^T$, which can be used directly in the following interpolations of the composite element (Fig.4.3):

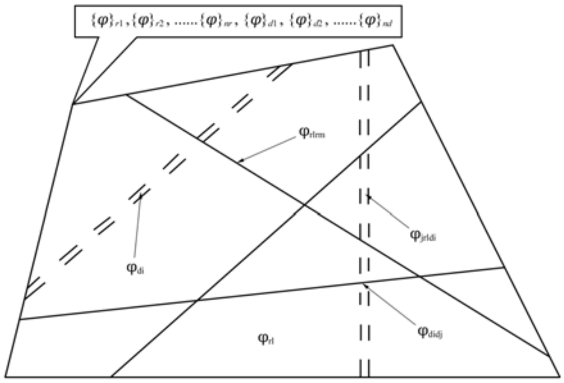

Fig.4.3 Hydraulic potential interpolation in composite element

$$\phi_{ri} = [N]\{\phi\}_{ri}, \quad (i = 1,2,\ldots,n_r) \tag{4-1}$$

$$\phi_{di} = [N]\{\phi\}_{di}, \quad (i = 1,2,\ldots,n_d) \tag{4-2}$$

Where [N] stands for the interpolation matrix (shape function matrix) defined in the whole composite element.

$$[N] = [N_1 \quad N_2 \quad \ldots\ldots N_n] \tag{4-3}$$

4.2 Composite element analysis

4.2.1 Conductivity matrix of the rock sub-element rl

With or without drainage holes, the conductivity matrix of the rock sub-element is still the same, see the Eq.(3-6) in the chapter 3.

4.2.2 Conductivity matrix of the fracture sub-element j_{rlrm}

With or without drainage holes, the conductivity matrix of the fracture sub-element is also still the same, see the Eq.(3-5) in the chapter 3.

4.2.3 Conductivity matrix of the drainage hole sub-element

Generally it is supposed that drainage hole is hollow and filled with air or water. In the explicit modeling, the wall of the drainage hole is taken as boundary with conditions defined in the Eq.(2-34) or Eq.(2-35), and the empty hole itself will not be included in the variational function Eq.(2-41) (Fipps, Skaggs, Nieber,1986). This treatment is correct but, as can be anticipated, will impose very strong restraint on the computation mesh generation, and a large freedom equation will be produced which will impose very strong restraint on the computer capacity. Furthermore, when the free surface intersected by the drainage holes, the iteration procedure will become very complicated.

From the practical point of view, it can be understood that an empty hole makes no essential difference with the hole filled by a kind of material having much larger permeability compared to the surrounding rock. In this way the drainage hole can be included in the variational function Eq.(2-41), consequently no boundary condition should be imposed on the wall of the holes. This conceptualized drainage hole element is named as "air element" (Hu, Chen, 2003). Hu and Chen also proposed the appropriate permeability for the imagined material within the hole: the proportion $P = k_d / k_r$ ranges between 10^3 to 10^4 can ensure the solution precision, where k_d and k_r are the permeability coefficients of the drainage hole and rock respectively.

According to the concept of the air element, the drainage hole is then looked at as a solid sub-element located within composite element, the hydraulic conductivity matrix and the corresponding right side item of the drainage hole sub-element can be given through the application of variational principle as:

$$[h]_{di}\{\phi\}_{di} = \{f\}_{di} \tag{4-4}$$

$$[h]_{di} = \iiint_{\Omega_{di}} (\{S\}[N])^T [k]_{di} (\{S\}[N]) d\Omega \tag{4-5}$$

$$\{f\}_{di} = \iiint_{\Omega_{di}} [N] f \, d\Omega - \iint_{\Gamma_{di}} [N] g \, d\Gamma \tag{4-6}$$

4.2.4 Conductivity matrix of the drainage hole/rock interface sub-element

There is no independent nodal hydraulic potential for the drainage hole/rock interface sub-element. The differential of the hydraulic potential within the interface in the variational function (Eq.(2-41)) is expressed by the different of the nodal value corresponding to the rock and drainage hole respectively.

Since hydraulic potential is a scalar, the variational function (Eq.(2-41)) in the interface can be expressed in the local Cylindrical coordinate system as:

$$I(\phi)^{cl}_{j_{rldi}} = \iiint_{\Omega_{j_{rldi}}} \left(\frac{1}{2}(\{S\}\phi)^T [k]_{j_{rldi}} (\{S\}\phi) \right) d\Omega \tag{4-7}$$

The inner source item and the boundary source item are neglected for the interface element. Since the thickness of the interface should be much smaller compared to the diameter of the drainage hole, it can assume that along the thickness:

$$(\{S\}\phi) = const. \tag{4-8}$$

So Eq.(4-7) is changed into:

$$I(\phi)^{cl}_{j_{rldi}} = \mathrm{Re} \iint_{\Gamma_{j_{rldi}}} \left(\frac{1}{2}(\{S\}_{j_{rldi}}\phi)^{\ T} [k]_{j_{rldi}} (\{S\}_{j_{rldi}}\phi) \right) d\omega dz \tag{4-9}$$

In which R is the diameter of the drainage hole and e is the thickness of the interface. The assumption is further made that at the local cylindrical coordinate system, the differential of the hydraulic potential within the interface will be:

$$\begin{cases} \dfrac{\partial \phi}{\partial r} = \dfrac{\phi_{rl} - \phi_{di}}{e} \\ \dfrac{\partial \phi}{\partial \omega} = 0 \\ \dfrac{\partial \phi}{\partial z} = 0 \end{cases} \tag{4-10}$$

In this way Eq.(4-9) becomes:

$$I(\phi)^{cl}_{j_{rldi}} = \frac{R}{e} \iint_{\Gamma_{j_{rldi}}} \left(\frac{1}{2}(\begin{Bmatrix} \phi_{rl} - \phi_{di} \\ 0 \\ 0 \end{Bmatrix})^T [k]_{j_{rldi}} (\begin{Bmatrix} \phi_{rl} - \phi_{di} \\ 0 \\ 0 \end{Bmatrix}) \right) d\omega dz \tag{4-11}$$

Considering the interpolation Eqs.(4-1)-(4-2)

$$I(\phi)^{cl}_{j_{rldi}} = \frac{R}{e} \iint_{\Gamma_{j_{rldi}}} \left(\frac{1}{2}([N](\{\phi\}_{rl} - \{\phi\}_{di}))^T k_{j_{rldi}} ([N](\{\phi\}_{rl} - \{\phi\}_{di})) \right) d\omega dz \tag{4-12}$$

The final form of the left side of the variational function for the rock/drainage hole interface is:

$$\begin{aligned} I(\phi)^{cl}_{j_{rldi}} = \frac{Rk_{j_{rldi}}}{e} \iint_{\Gamma_{j_{rldi}}} \frac{1}{2}(&\{\phi\}^T_{rl}[N]^T[N]\{\phi\}_{rl} - \{\phi\}^T_{rl}[N]^T[N]\{\phi\}_{di} \\ &- \{\phi\}^T_{di}[N]^T[N]\{\phi\}_{rl} + \{\phi\}^T_{di}[N]^T[N](\{\phi\}_{di}) d\omega dz \end{aligned} \tag{4-13}$$

The minimum condition of the Eq.(4-13) gives the hydraulic conductivity matrix of the rock/drainage hole interface sub-element as follows:

$$\begin{cases} [h]_{di,di} = \dfrac{Rk_{j_{rldi}}}{e} \iint_{\Gamma_{j_{rldi}}} [N]^T [N] d\omega dz \\ [h]_{rl,di} = [h]_{di,rl} = -\dfrac{Rk_{j_{rldi}}}{e} \iint_{\Gamma_{j_{rldi}}} [N]^T [N] d\omega dz \end{cases} \tag{4-14}$$

The permeability coefficient of interface $k_{j_{rldi}}$ can be set as equal to the permeability coefficient of the imagined drainage hole material k_d, and $R/t = 100$ will lead to precision satisfactory solution of the problem.

4.2.5 The interface j_{didj} between drainage hole sub-element di and dj

This interface is only considered when the drainage hole sub-element di and dj belong to the same drainage hole and is intersected by the fracture sub-element j_{rlrm}. The variational function (Eq.(2-41)) in this interface can be expressed in the local Cylindrical coordinate system as:

$$I(\phi)_{j_{didj}} = \iiint_{\Omega_{didj}} \left(\frac{1}{2} (\{S\}\phi)^T [k]_{j_{didj}} (\{S\}\phi) \right) d\Omega \tag{4-15}$$

The thickness e of this interface is the same as that of the fracture sub-element j_{rlrm}, and should be much smaller compared to the diameter of the drainage hole, therefore it can be assumed that the velocity is constant in the normal direction of fracture surface. It also can be obtained:

$$\begin{aligned} I(\phi)_{j_{didj}} &= \iint_{\Gamma_{didj}} \left(\frac{1}{2} \{S_j\}\phi)^T [k]_{didj} (\{S_j\}\phi \right) e dx_{j_{rlrm}} dy_{j_{rlrm}} \\ &= e \iint_{\Gamma_{didj}} \frac{1}{2} \left((\{S_j\} \frac{1}{2}(\phi_{di} + \phi_{dj}))^T [k]_{didj} (\{S_j\} \frac{1}{2}(\phi_{di} + \phi_{dj})) \right) dx_{j_{rlrm}} dy_{j_{rlrm}} \end{aligned} \tag{4-16}$$

$$\begin{cases} \dfrac{\partial \phi}{\partial x_{j_{rlrm}}} = \dfrac{\partial [\frac{1}{2}(\phi_{di} + \phi_{dj})]}{\partial x_{j_{rlrm}}} = \dfrac{1}{2} \dfrac{\partial (\phi_{di} + \phi_{dj})}{\partial x_{j_{rlrm}}} \\ \dfrac{\partial \phi}{\partial y_{j_{rlrm}}} = \dfrac{\partial [\frac{1}{2}(\phi_{di} + \phi_{dj})]}{\partial y_{j_{rlrm}}} = \dfrac{1}{2} \dfrac{\partial (\phi_{di} + \phi_{dj})}{\partial y_{j_{rlrm}}} \\ \dfrac{\partial \phi}{\partial z_{j_{rlrm}}} = \dfrac{\partial [\frac{1}{2}(\phi_{di} + \phi_{dj})]}{\partial z_{j_{rlrm}}} = \dfrac{1}{2} \dfrac{\partial (\phi_{di} + \phi_{dj})}{\partial z_{j_{rlrm}}} \end{cases} \tag{4-17}$$

Because

$$\phi_{di} = [N]\{\bar{\phi}\}_{di}\ ;\ \phi_{dj} = [N]\{\bar{\phi}\}_{dj} \tag{4-18}$$

Then

$$\frac{\partial \phi_{di}}{\partial x_{j_{rlrm}}} = \frac{\partial([N]\{\bar{\phi}\}_{di})}{\partial x_{j_{rlrm}}} = [N_{x_{j_{rlrm}}}]\{\bar{\phi}\}_{di}\ ;\ \frac{\partial \phi_{dj}}{\partial x_{j_{rlrm}}} = [N_{x_{j_{rlrm}}}]\{\bar{\phi}\}_{dj} \tag{4-19}$$

$$\frac{\partial \phi_{di}}{\partial y_{j_{rlrm}}} = \frac{\partial([N]\{\bar{\phi}\}_{di})}{\partial y_{j_{rlrm}}} = [N_{y_{j_{rlrm}}}]\{\bar{\phi}\}_{di}\ ;\ \frac{\partial \phi_{dj}}{\partial y_{j_{rlrm}}} = [N_{y_{j_{rlrm}}}]\{\bar{\phi}\}_{dj} \tag{4-20}$$

$$\frac{\partial \phi_{di}}{\partial z_{j_{rlrm}}} = \frac{\partial([N]\{\bar{\phi}\}_{di})}{\partial z_{j_{rlrm}}} = [N_{z_{j_{rlrm}}}]\{\bar{\phi}\}_{di}\ ;\ \frac{\partial \phi_{dj}}{\partial z_{j_{rlrm}}} = [N_{z_{j_{rlrm}}}]\{\bar{\phi}\}_{dj} \tag{4-21}$$

Denoting

$$[N_{x_{j_{rlrm}}}] = [\frac{\partial N}{\partial x_{j_{rlrm}}}]\ ;\ [N_{y_{j_{rlrm}}}] = [\frac{\partial N}{\partial y_{j_{rlrm}}}]\ ;\ [N_{z_{j_{rlrm}}}] = [\frac{\partial N}{\partial z_{j_{rlrm}}}] \tag{4-22}$$

Eq.(4-16) can be re-written as:

$$\begin{aligned}
I(\phi)_{j_{didj}} &= e\iint_{\Gamma_{didj}} \left(\frac{1}{2}(\begin{Bmatrix} \frac{1}{2}\frac{\partial(\phi_{di}+\phi_{dj})}{\partial x_{j_{rlrm}}} \\ \frac{1}{2}\frac{\partial(\phi_{di}+\phi_{dj})}{\partial y_{j_{rlrm}}} \\ \frac{1}{2}\frac{\partial(\phi_{di}+\phi_{dj})}{\partial z_{j_{rlrm}}} \end{Bmatrix})^T \begin{bmatrix} k_1 & 0 & 0 \\ 0 & k_2 & 0 \\ 0 & 0 & k_3 \end{bmatrix} (\begin{Bmatrix} \frac{1}{2}\frac{\partial(\phi_{di}+\phi_{dj})}{\partial x_{j_{rlrm}}} \\ \frac{1}{2}\frac{\partial(\phi_{di}+\phi_{dj})}{\partial y_{j_{rlrm}}} \\ \frac{1}{2}\frac{\partial(\phi_{di}+\phi_{dj})}{\partial z_{j_{rlrm}}} \end{Bmatrix}) \right) dx_{j_{rlrm}} dy_{j_{rlrm}} \\
&= \frac{e}{2}\iint \left(\frac{k_1}{4}(\frac{\partial(\phi_{di}+\phi_{dj})}{\partial x_{j_{rlrm}}})^2 + \frac{k_2}{4}(\frac{\partial(\phi_{di}+\phi_{dj})}{\partial y_{j_{rlrm}}})^2 + k_3(\frac{\partial(\phi_{di}+\phi_{dj})}{\partial z_{j_{rlrm}}})^2 \right) dx_{j_{rlrm}} dy_{j_{rlrm}} \\
&= \frac{e}{2}\iint \left(\begin{aligned} &\frac{k_1}{4}((\frac{\partial\phi_{di}}{\partial x_{j_{rlrm}}})^2 + 2\frac{\partial\phi_{di}}{\partial x_{j_{rlrm}}}\frac{\partial\phi_{dj}}{\partial x_{j_{rlrm}}} + (\frac{\partial\phi_{dj}}{\partial x_{j_{rlrm}}})^2) + \frac{k_2}{4}((\frac{\partial\phi_{di}}{\partial y_{j_{rlrm}}})^2 + 2\frac{\partial\phi_{di}}{\partial y_{j_{rlrm}}}\frac{\partial\phi_{dj}}{\partial y_{j_{rlrm}}} + (\frac{\partial\phi_{dj}}{\partial y_{j_{rlrm}}})^2) + \\ &\frac{k_3}{4}((\frac{\partial\phi_{di}}{\partial z_{j_{rlrm}}})^2 + 2\frac{\partial\phi_{di}}{\partial z_{j_{rlrm}}}\frac{\partial\phi_{dj}}{\partial z_{j_{rlrm}}} + (\frac{\partial\phi_{dj}}{\partial z_{j_{rlrm}}})^2) \end{aligned} \right) dx_{j_{rlrm}} dy_{j_{rlrm}} \\
&= \frac{e}{2}\iint \left(\begin{aligned} &\frac{k_1}{4}(\{\bar{\phi}\}_{di}^T[N_{x_{j_{rlrm}}}]^T[N_{x_{j_{rlrm}}}]\{\bar{\phi}\}_{di} + 2\{\bar{\phi}\}_{di}^T[N_{x_{j_{rlrm}}}]^T[N_{x_{j_{rlrm}}}]\{\bar{\phi}\}_{dj} + \{\bar{\phi}\}_{dj}^T[N_{x_{j_{rlrm}}}]^T[N_{x_{j_{rlrm}}}]\{\bar{\phi}\}_{dj}) + \\ &\frac{k_2}{4}(\{\bar{\phi}\}_{di}^T[N_{y_{j_{rlrm}}}]^T[N_{y_{j_{rlrm}}}]\{\bar{\phi}\}_{di} + 2\{\bar{\phi}\}_{di}^T[N_{y_{j_{rlrm}}}]^T[N_{y_{j_{rlrm}}}]\{\bar{\phi}\}_{dj} + \{\bar{\phi}\}_{dj}^T[N_{y_{j_{rlrm}}}]^T[N_{y_{j_{rlrm}}}]\{\bar{\phi}\}_{dj}) + \\ &\frac{k_3}{4}(\{\bar{\phi}\}_{di}^T[N_{z_{j_{rlrm}}}]^T[N_{z_{j_{rlrm}}}]\{\bar{\phi}\}_{di} + 2\{\bar{\phi}\}_{di}^T[N_{z_{j_{rlrm}}}]^T[N_{z_{j_{rlrm}}}]\{\bar{\phi}\}_{dj} + \{\bar{\phi}\}_{dj}^T[N_{z_{j_{rlrm}}}]^T[N_{z_{j_{rlrm}}}]\{\bar{\phi}\}_{dj}) \end{aligned} \right) dx_{j_{rlrm}} dy_{j_{rlrm}}
\end{aligned}$$

(4-23)

Take the minimum value of the function of Eq.(4-23) for $\{\bar{\phi}\}_{di}, \{\bar{\phi}\}_{dj}$, then it can be obtained that:

$$\frac{\partial I(\phi)_{didj}}{\partial\{\bar{\phi}\}_{di}} = \frac{e}{2}\iint_{\Gamma_{didj}}\begin{pmatrix}\frac{k_1}{4}(2[N_{x_{jrlrm}}]^T[N_{x_{jrlrm}}]\{\bar{\phi}\}_{di} + 2[N_{x_{jrlrm}}]^T[N_{x_{jrlrm}}]\{\bar{\phi}\}_{dj}) + \\ \frac{k_2}{4}(2[N_{y_{jrlrm}}]^T[N_{y_{jrlrm}}]\{\bar{\phi}\}_{di} + 2[N_{y_{jrlrm}}]^T[N_{y_{jrlrm}}]\{\bar{\phi}\}_{dj}) + \\ \frac{k_3}{4}(2[N_{z_{jrlrm}}]^T[N_{z_{jrlrm}}]\{\bar{\phi}\}_{di} + 2[N_{z_{jrlrm}}]^T[N_{z_{jrlrm}}]\{\bar{\phi}\}_{dj}))\end{pmatrix} dx_{jrlrm}\,dy_{jrlrm}$$

$$= \frac{e}{4}\iint\begin{pmatrix}(k_1[N_{x_{jrlrm}}]^T[N_{x_{jrlrm}}] + k_2[N_{y_{jrlrm}}]^T[N_{y_{jrlrm}}] + k_3[N_{z_{jrlrm}}]^T[N_{z_{jrlrm}}])\{\bar{\phi}\}_{di} + \\ (k_1[N_{x_{jrlrm}}]^T[N_{x_{jrlrm}}] + k_2[N_{y_{jrlrm}}]^T[N_{y_{jrlrm}}] + k_3[N_{z_{jrlrm}}]^T[N_{z_{jrlrm}}])\{\bar{\phi}\}_{dj}\end{pmatrix} dx_{jrlrm}\,dy_{jrlrm}$$

$$= 0 \tag{4-24}$$

$$\frac{\partial I(\phi)_{didj}}{\partial\{\bar{\phi}\}_{dj}} = \frac{e}{4}\iint\begin{pmatrix}(k_1[N_{x_{jrlrm}}]^T[N_{x_{jrlrm}}] + k_2[N_{y_{jrlrm}}]^T[N_{y_{jrlrm}}] + k_3[N_{z_{jrlrm}}]^T[N_{z_{jrlrm}}])\{\bar{\phi}\}_{di} + \\ (k_1[N_{x_{jrlrm}}]^T[N_{x_{jrlrm}}] + k_2[N_{y_{jrlrm}}]^T[N_{y_{jrlrm}}] + k_3[N_{z_{jrlrm}}]^T[N_{z_{jrlrm}}])\{\bar{\phi}\}_{dj}\end{pmatrix} dx_{jrlrm}\,dy_{jrlrm}$$

$$= 0 \tag{4-25}$$

It can be obtained that:

$$\begin{cases}[h]_{lidi}\{\bar{\phi}\}_{di} + [h]_{lidj}\{\bar{\phi}\}_{dj} = 0 \\ [h]_{ljdi}\{\bar{\phi}\}_{di} + [h]_{ljdj}\{\bar{\phi}\}_{dj} = 0\end{cases} \tag{4-26}$$

Where

$$[h]_{lidi} = [h]_{ljdj} = [h]_{lidj} = [h]_{ljdi}$$

$$= \frac{e}{4}\iint_{\Gamma_{didj}}(k_1[N_{x_{jrlrm}}]^T[N_{x_{jrlrm}}] + k_2[N_{y_{jrlrm}}]^T[N_{y_{jrlrm}}] + k_3[N_{z_{jrlrm}}]^T[N_{z_{jrlrm}}])dx_{jrlrm}\,dy_{jrlrm} \tag{4-27}$$

4.2.6 Assemblage of the composite element

Assembles all the conductivity matrices for sub-elements, the variational principle for the whole domain concerned will lead to the following governing equation for the composite element containing fractures and drainage holes:

$$\begin{bmatrix}[H]_{1,1} & [H]_{1,2} & \cdots & [H]_{1,n_r} & [H]_{1,n_r+1} & \cdots & [H]_{1,n_r+n_d} \\ [H]_{2,1} & [H]_{2,2} & \cdots & [H]_{2,n_r} & [H]_{2,n_r+1} & \cdots & [H]_{2,n_r+n_d} \\ \cdots & \cdots & \cdots & \cdots & \cdots & \cdots & \cdots \\ [H]_{n_r,1} & [H]_{n_r,2} & \cdots & [H]_{n_r,n_r} & [H]_{n_r,n_r+1} & \cdots & [H]_{n_r,n_r+n_d} \\ [H]_{n_r+1,1} & [H]_{n_r+1,2} & \cdots & [H]_{n_r+1,n_r} & [H]_{n_r+1,n_r+1} & \cdots & [H]_{n_r+1,n_r+n_d} \\ \cdots & \cdots & \cdots & \cdots & \cdots & \cdots & \cdots \\ [H]_{n_r+n_d,1} & [H]_{n_r+n_d,1} & \cdots & [H]_{n_r+n_d,n_r} & [H]_{n_r+n_d,n_r+1} & \cdots & [H]_{n_r+n_d,n_r+n_d}\end{bmatrix}\begin{Bmatrix}\{\phi\}_1 \\ \{\phi\}_2 \\ \ldots \\ \{\phi\}_{n_r} \\ \{\phi\}_{n_r+1} \\ \ldots \\ \{\phi\}_{n_r+n_d}\end{Bmatrix} = \begin{Bmatrix}\{f\}_1 \\ \{f\}_2 \\ \ldots \\ \{f\}_{n_r} \\ \{f\}_{n_r+1} \\ \ldots \\ \{f\}_{n_r+n_d}\end{Bmatrix} \tag{4-28}$$

In which

$$
\begin{cases}
[H]_{rl,rl} = [h]_{rl} + \sum\limits_{rm=1,rm\neq rl}^{n_r} A(rl,rm)[h]_{rl,rl} + \sum\limits_{di=1}^{n_d} B(rl,di)[h]_{di,di}, & (rl = 1,\ldots n_r) \\
[H]_{rl,rm} = A(rl,rm)[h]_{rl,rm}, & (rl \neq rm \quad rl,rm = 1,\ldots n_r) \\
[H]_{rl,n_r+di} = B(rl,di)[h]_{rl,di}, & (di = 1,n_d \quad rl = 1,\ldots n_r) \\
A(rl,rm) = \begin{cases} 1, \text{ if } rl \text{ and } rm \text{ are neighbour sub-elements} \\ 0, \text{ if } rl \text{ and } rm \text{ are not neighbour sub-elements} \end{cases} \\
B(rl,di) = \begin{cases} 1, \text{ if sub-element } di \text{ is within sub-element } rl \\ 0, \text{ if sub-element } di \text{ is not within sub-element } rl \end{cases}
\end{cases}
\tag{4-29}
$$

$$
\begin{cases}
[H]_{n_r+di,n_r+di} = [h]_{di} + \sum\limits_{dj=1,dj\neq di}^{n_d} C(di,dj)[h]_{di,di} + \sum\limits_{rl=1}^{n_r} B(di,rl)[h]_{di,di}, & (di = 1,\ldots n_d) \\
[H]_{n_r+di,n_r+dj} = C(di,dj)[h]_{di,dj}, & (di \neq dj \quad di,dj = 1,\ldots n_d) \\
[H]_{n_r+di,rl} = B(di,rl)[h]_{di,rl}, & (di = 1,n_d \quad rl = 1,\ldots n_r) \\
C(di,dj) = \begin{cases} 1, \text{ if } di \text{ and } dj \text{ are connexted drainage hole sub-elements} \\ 0, \text{ if } di \text{ and } dj \text{ are not connexted drainage hole sub-elements} \end{cases} \\
B(di,rl) = \begin{cases} 1, \text{ if sub-element } di \text{ is within sub-element } rl \\ 0, \text{ if sub-element } di \text{ is not within sub-element } rl \end{cases}
\end{cases}
\tag{4-30}
$$

Substituting Eq.(3-17) into Eqs(4-14)(4-27), then combining Eq.(4-30), it can be seen that, the change of fracture aperture would lead to the change of the whole seepage field, and the changed seepage load force will lead to the change of the stress field accordingly, this is the coupling mechanism of seepage and stress coupling for fractured rock mass containing drainage holes, which is the same to that of the seepage and stress coupling for fractured rock mass without drainage holes.

4.3 Verification and application

4.3.1 Verification

The verification of the proposed algorithm is carried out on the rock block (length 0.76m×width 0.10m×height 0.20m) illustrated in the Fig.4.4(a), with 2592 nodes and 1950 elements, containing a horizontal fracture of aperture e=0.001m and a vertical drainage hole of diameter 0.02m. The finite element model is at the same size, the fracture is simulated discretely into joint elements (Goodman, Taylor, Brekke, 1968), and the drainage hole is simulated through implicit method, with 5148 nodes and 3990 elements (see Fig.4.4(b)).

Both the two models have the same boundary conditions and load cases. At the upstream face (X=0.00m) the hydraulic potential is fixed to be 10.0m, at the top surface of the drainage hole it is fixed to be 5.0m, and the down stream face (X=0.76m) with hydraulic potential 7.5m, and there is no flow exchange with external system for the other boundaries. The concentrated force F (Fig.4.4) and water pressure are considered, weight of rock mass is assumed as zero. Bottom Z-axis displacement is restricted, as well as the right-and-left boundary nodes in the direction X, Y.

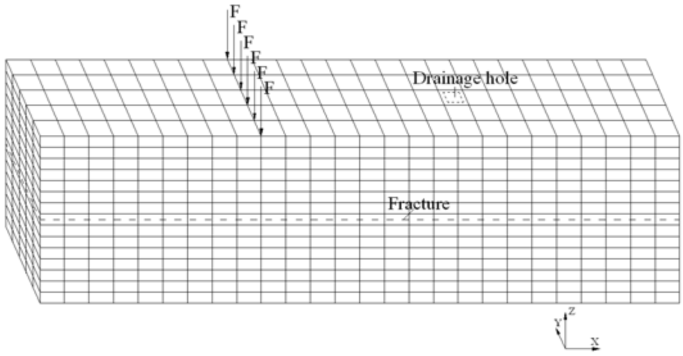

(a) Mesh of composite element method (CEM)

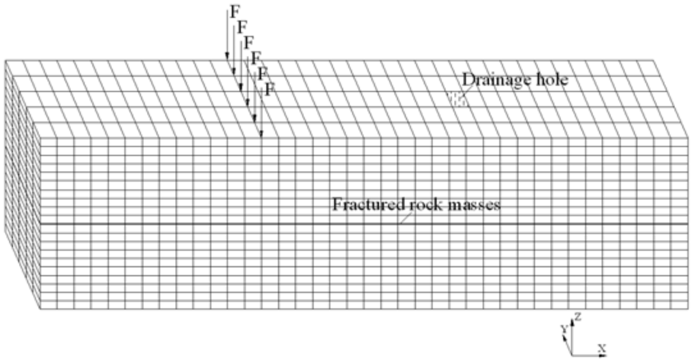

(b) Mesh of finite element method (FEM)

Fig.4.4 Mesh of numerical models

4.3.1.1 Computation conditions

The two models have the same computation parameters of rock mass, given in the Tab.4.1. The computation parameters of fractures and drainage holes for the two models are given respectively in the Tabs.4.2~ 4.4.

Tab.4.1 Parameters of rock mass

Young's modulus E/MPa	Poisson's ration μ	Volumetric weight γ /(kN·m^{-3})	k_{rl}/(m·s^{-1})
5 000	0.32	24	1.0×10^{-4}

Tab.4.2 Parameters of fractures for the CEM

φ_j /(°)	θ_j /(°)	e_0 /m	k_n /(MPa·m^{-1})	k_s /(MPa·m^{-1})	ξ	$k_{j_{rl,rm}}$ /(m·s^{-1})
0	0	0.001	5 000	3 000	changeable	0.5382

Tab.4.3 Parameters of fractures for the FEM

φ_j /(°)	θ_j /(°)	e_0 /m	b/m	Normal stiffness k_n/(MPa·m^{-1})	Shear stiffness k_s/(MPa·m^{-1})	ξ
0	0	0.001	0.001	5 000	3 000	changeable

Tab.4.4 Parameters of drainage holes

φ_j /(°)	θ_j /(°)	diameter/m	k_d /(m·s^{-1})
0	90	0.02	10.0

4.3.1.2 Computation results

Both the FEM and CEM are used in the study, and the computation results obtained by the two methods are contrasted with each other. Two computational cases are considered as follows.

Case 1 Without considering the seepage and stress coupling, that is $\xi = 0$;

Case 2 Consider the coupling, with the concentrated force F=-0.04MN;

Rock mass and fractures are regarded as elastic media, and the convergence precision of hydraulic potential is 0.01m, mechanics parameters of rock mass and the "filled" medium in the fractures keep constant.

Fig.4.5 shows the hydraulic potential contour at the vertical section *x-o-z*. The hydraulic potential obtained from the CEM agrees exactly with those from the FEM. The hydraulic potential contour lines concentrate to the region where the concentrated force acts, and the uneven characteristics caused by the stress can be seen obviously here.

Fig.4.6 shows the hydraulic potential along the fracture as a function of concentrated force. The change rule of the hydraulic potential along the fracture is consistent with that of the Fig.4.5. In the Fig.4.6, the change of the seepage gradient along the fracture can be indicated by the change of the curve slope, and it can be seen that, the seepage gradient of the field where the concentrated forces act increase as the increase of concentrated force.

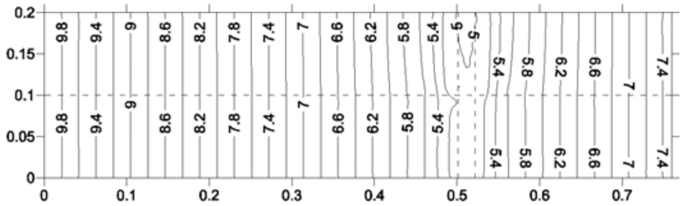

By CEM

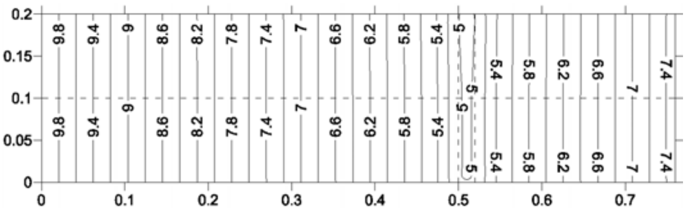

By FEM

(a)$\xi = 0$

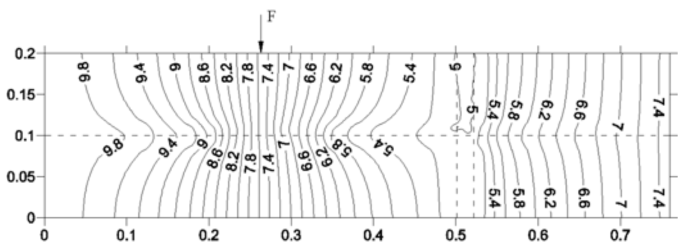

By CEM

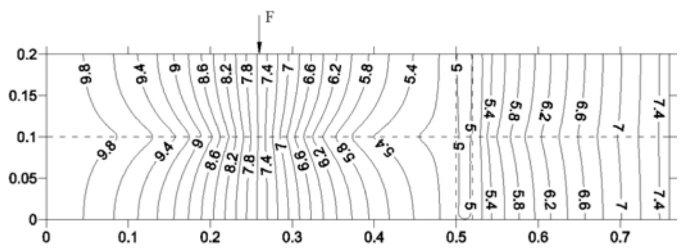

By FEM

(b)F= -0.04MN

Fig.4.5 Hydraulic potential contour

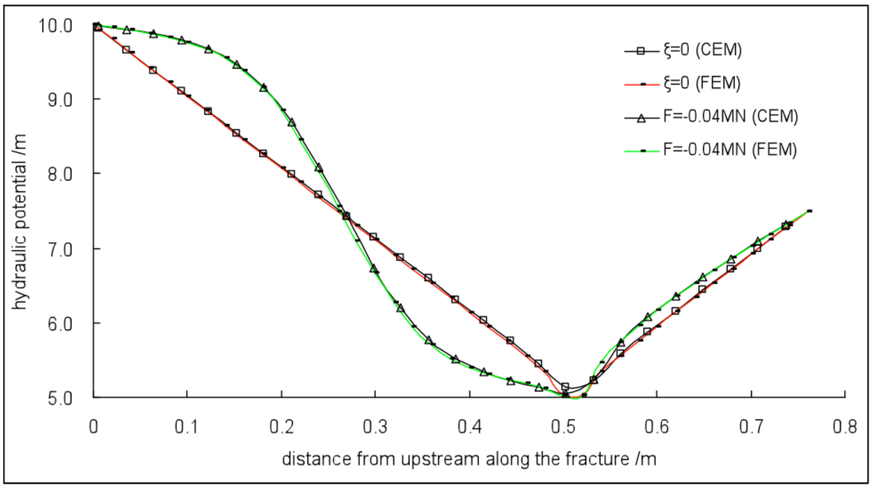

Fig.4.6 Hydraulic potential along the fracture as a function of concentrated force

Fig.4.7 shows the seepage velocity vector by the two methods, and Fig.4.8 shows the seepage velocity along the fracture as a function of concentrated force. From the Figs.4.7~ 4.8, it can be seen that, the seepage velocity by the CEM is almost the same with that by the FEM, and the seepage velocity along the fracture increases in the region where the concentrated force acts, as the increase of the concentrated force.

The flow rate per unit width along *y*-direction as a function of concentrated force is shown in the Fig.4.9. Again, it can be seen that, the results obtained by the CEM close to those obtained by the FEM. As the increase of the concentrated force, the flow rate per unit width reduces with exponential decrease.

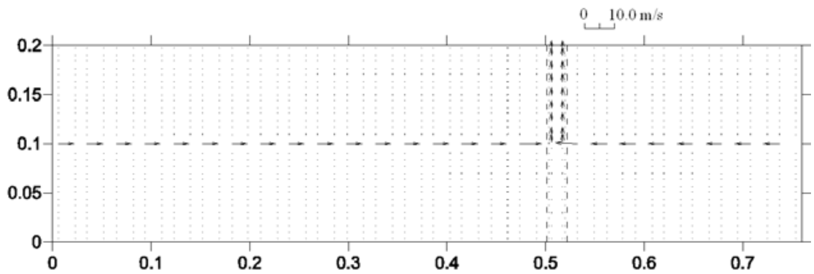

By CEM

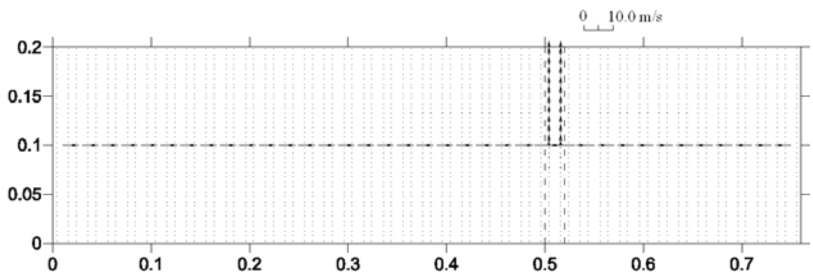

By FEM

(a) $\xi = 0$

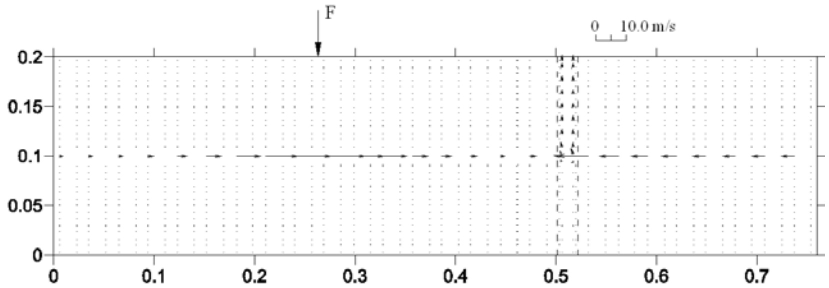

By CEM

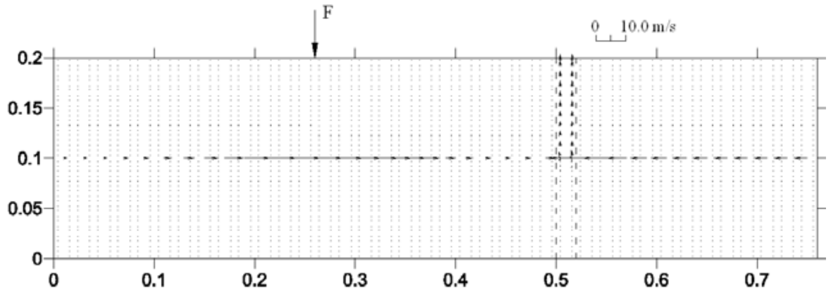

By FEM

(b) *F*= -0.04MN

Fig.4.7 Seepage velocity vector

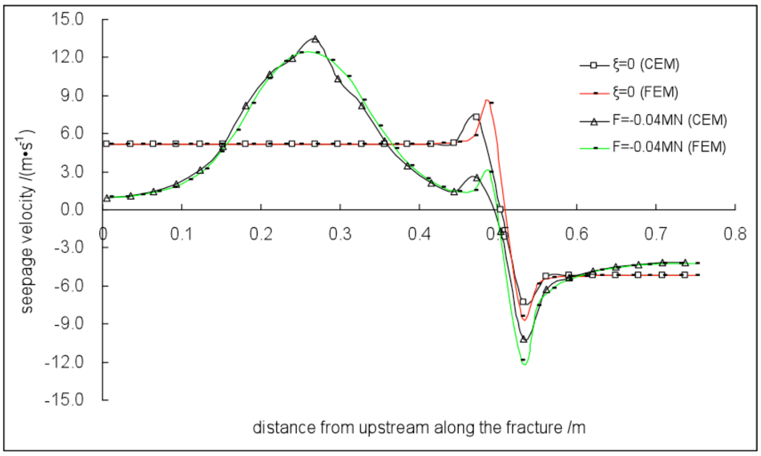

Fig.4.8 Seepage velocity along the fracture as a function of concentrated force

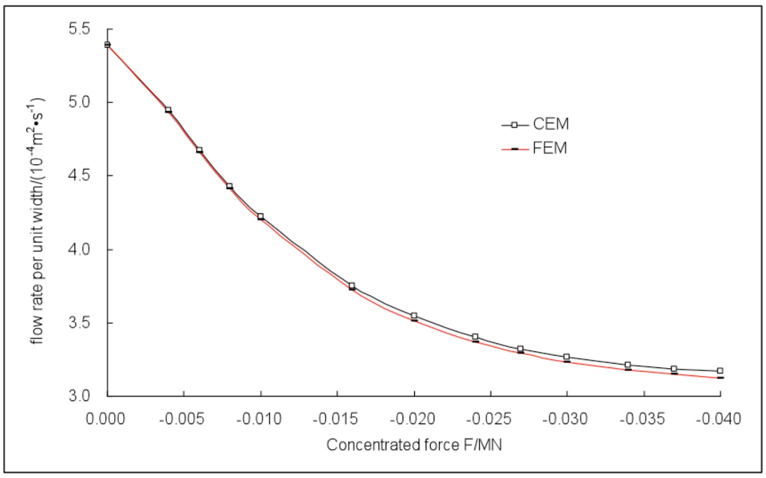

Fig.4.9 Flow rate per unit width as a function of concentrated force

4.3.2 Application in the completed non-pressure well

There is one completed non-pressure well, and the thickness of the impermeable layer H is fixed to be 10.0m, the influence radius R is 100.0m. The radius of the well r_0 is 0.1m, and the hydraulic potential in the well h_0 is 3.0m, and the underground water level at the infinite distance is fixed to be 10.0m. There is a horizontal fracture with aperture e=0.001m crossing the well at the position z=1.5m, see the dashed line in the Fig.4.10 (a). There are 3344 nodes and 2880 elements in the mesh of composite element method, of which 297 are composite elements. All the top nodes of the numerical model have been acted on the vertical concentrated force F, see Fig.4.10 (b). The permeability coefficients of the numerical model are shown in the Tab.4.5.

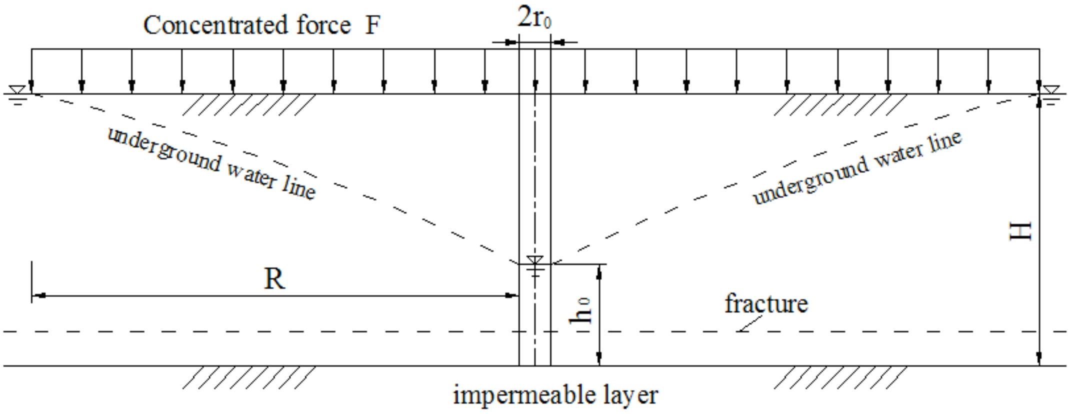

(a) Simplified Profile of completed non-pressure well

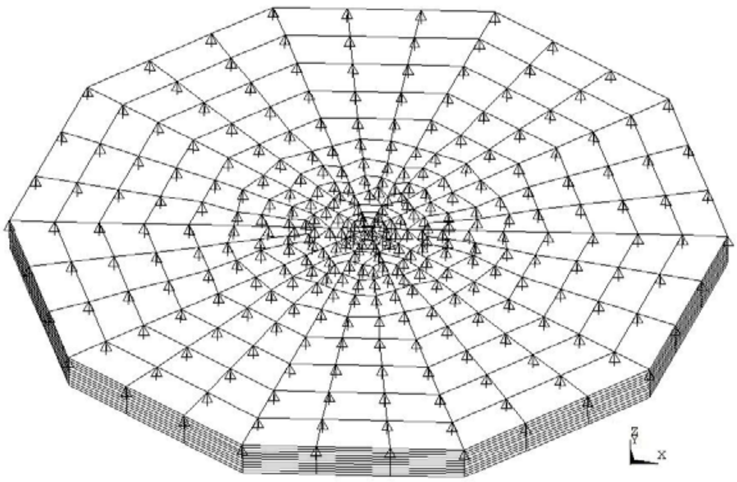

(b)Mesh of composite element method

Fig.4.10 Numerical model for completed non-pressure well

Tab.4.5 Permeability coefficients of the model k/m·s^{-1}

Rock mass	Fracture	Drainage holes
1.0E-05	0.5	50

Two computational cases are considered, with and without considering the coupling. This numerical analysis only focuses on showing the flow rate of the well as a function of the concentrated force.

Fig.4.11 shows the relationship between the flow rate and the concentrated force. It can be seen that, as the increase of the concentrated force, the flow rate decreases exponentially, from which the importance of seepage and stress coupling for fractured rock mass containing drainage holes is emphasized again.

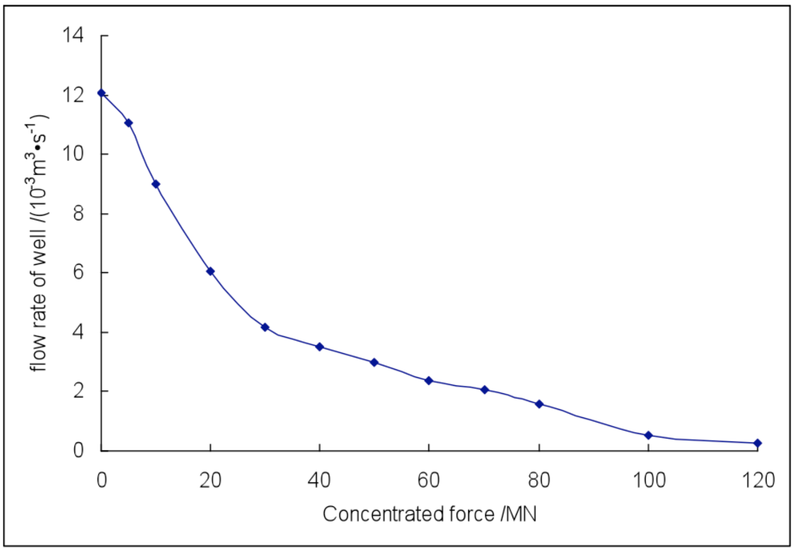

Fig.4.11 Flow rate of the well as a function of concentrated force

4.3.3 Application in the Baozhusi dam foundation

4.3.3.1 Computation conditions

The 131m high Baozhusi gravity dam is located in Bailongjiang River, China. The elevation of the river-bed on the upstream side of dam is 464m. The width of the dam's base is 92m (excluding the powerhouse). The rock mass under the foundation is Ordovician sand stone and at the downstream of the dam is Silurian shale (S_1). There are faults F_4, F_2 and intercalated layers D_5, $D_{7,8}$, D_1, D_3, D_6 located under foundation (Fig.4.12).

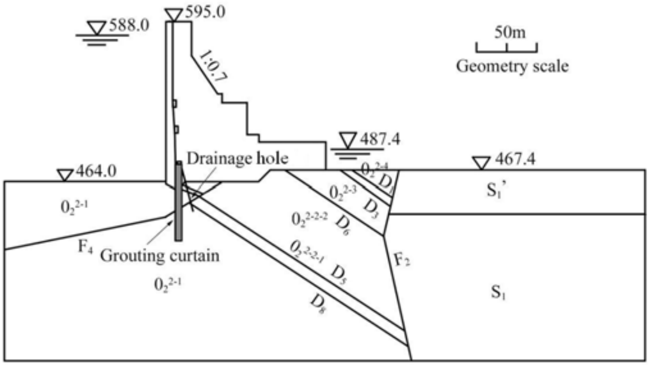

Fig.4.12 Simplified Profile of Baozhusi dam

To facilitate the understanding of the calculated results, a local coordinate system of the fractures is defined in the Fig.4.13. Take $O\_F_4\_Down$ and $O\_F_4\_Up$ for example, O means the origin for measuring along the fracture, $\_F_4$ denotes the fracture, $\_Down$ or $\_Up$ means the lower or upper part.

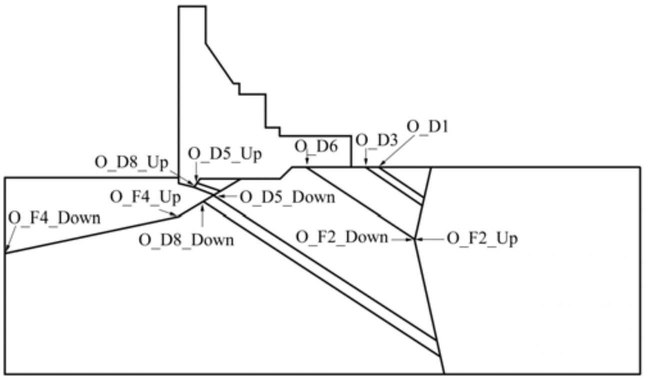

Fig.4.13 Origins of Discontinuities

The computation makes use of the CEM and the FEM, which are implemented in the same program. Based on the finite element method, there are two models, one is discrete simulation model for drainage holes (FEM1), and another one is equivalent simulation model for drainage holes by special elements in the mesh of finite element method, based on the method of drainage holes replaced by drainage curtain (FEM2). For the composite element model, the drainage holes have been simulated explicitly through the special elements, which are embedded into the mapped composite elements automatically by the preprocess programs of CEM. The computation provides detailed contrast between the three numerical models.

To control the seepage and to improve the stability of the dam foundation, grouting curtain and drainage curtain are deployed near the heel of the foundation (Fig.4.12). The grouting curtain is a continuous cement wall constructed by grouting, which is simulated by solid elements with small permeability coefficient (Tab.4.6). The drainage curtain is actually composed of an array of drainage holes, whose diameter and spacing are 15cm and 3m respectively.

A dam section of 3m thick along the dam axis is considered in the computation. Fig.4.14 is the composite element mesh projected at the $x-z$ plane, which includes 7596 nodes, 4710 elements, of which 508 are composite elements. Fig.4.15 is the finite element mesh (FEM1) projected at the $x-z$ plane, which includes 22307 nodes and 17552 elements. Fig.4.16 is the finite element mesh (FEM2) projected at the $x-z$ plane, which includes 19415 nodes and 15064 elements. It is obvious that since the faults and drainage holes are embedded within the composite element, the mesh used for CEM is much simpler than that used in FEM, and the equivalent model (FEM1) is simpler than the model simulated discretely by FEM (FEM2).

The permeability coefficients used in the study are listed in the Tab.4.6 and Tab.4.7.

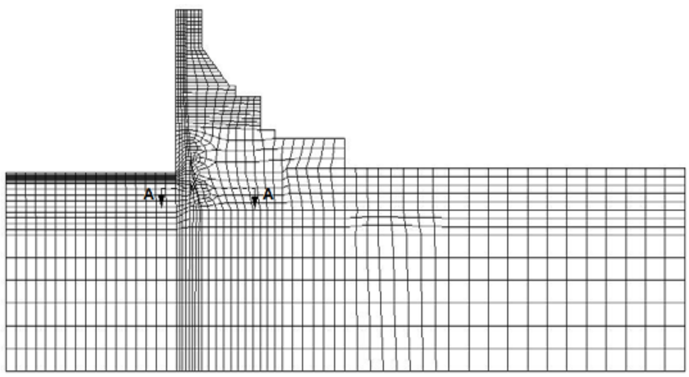

(a) Mesh of CEM model

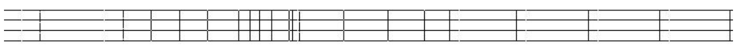

(b) Mesh of profile A-A

Fig.4.14 Mesh used for the analysis of the Baozhusi dam by CEM

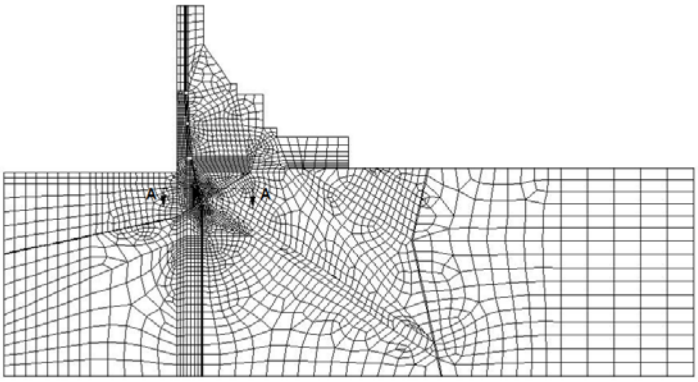

(a) Mesh of FEM model (FEM1)

(b) Mesh of profile A-A

Fig.4.15 Mesh by FEM with drainage holes of explicit simulation

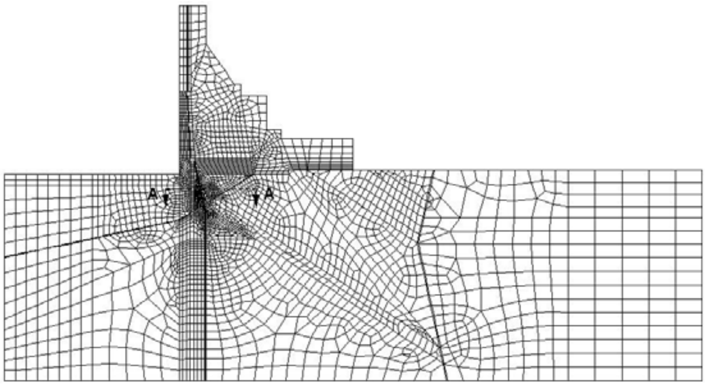

(a) Mesh of FEM model (FEM2)

(b) Mesh of profile A-A

Fig.4.16 Mesh by FEM with drainage holes of implicit simulation

Tab.4.6 Permeability coefficients of the rock mass and concrete

Material	Concrete	Grouting curtain	O_2^{2-1}	O_2^{2-2-1}	O_2^{2-2-2}, O_2^{2-3}	O_2^{2-4}	S_1'	S_1
Permeability / $m \cdot d^{-1}$	10^{-6}	10^{-5}	10^{-3}	10^{-3}	10^{-3}	10^{-3}	10^{-3}	10^{-3}

Tab.4.7 Permeability coefficients and thickness of the fractures

Fracture	$D_{1,3}$	D_6	$D_{7,8}$ (Upside of F_4)	$D_{7,8}$ (Downside of F_4)	D_5 (Upside of F_4)	D_5 (Downside of F_4)	F_4	F_2
Thickness /m	0.01	0.01	0.01	0.01	0.015	0.01	0.5	1.0
Permeability / m·d^{-1}	10^{-1}	10^{-1}	10^{-1}	10^{-1}	10^{-1}	10^{-1}	10^{-1}	10^{-1}

For the FEM2, based on the air element method, considering the drainage holes curtain as a homogenous medium, the permeability coefficient k_1 for drainage holes (air element) keeps about 1000 times with the permeability coefficient k_2 of around materials (Hu, Chen, 2003). Diameter of drainage hole is denoted as D_1, holes distance is L_1, as shown in Fig.4.17, and then the equivalent permeability coefficient k for elements in the drainage holes curtain field can be calculated by the equivalent flow rate principle. Then the mesh generation does not depend strongly on the size of drainage holes than the discrete simulation, and the mesh generation becomes much simpler than that of the FEM1.

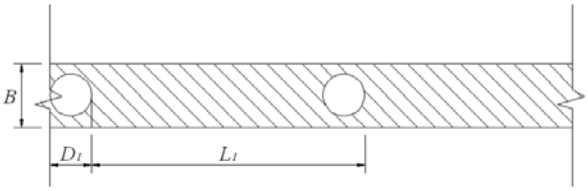

Fig.4.17 Sketch for drainage holes

$$kB = k_1 \frac{\pi D_1^2}{4} / L_1 + k_2 (B - \frac{\pi D_1^2}{4} / L_1) \tag{4-31}$$

That is

$$k = \frac{k_1 \frac{\pi D_1^2}{4} / L_1 + k_2 (B - \frac{\pi D_1^2}{4} / L_1)}{B} \tag{4-32}$$

4.3.3.2 Computation results

Fig.4.18 shows the hydraulic potential contour. Fig.4.19 shows the flow velocity distribution in the foundation. It can be seen that the FEM and the CEM give nearly identical results for the hydraulic and flow velocity distributions, and the equivalent drainage holes model almost has the identical results to the model simulated discretely.

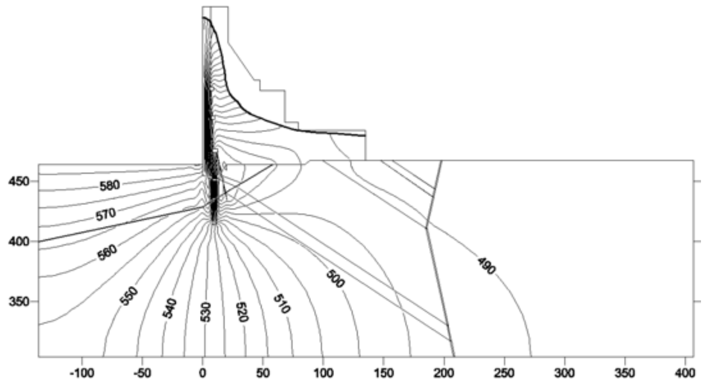

(a) CEM, $y = 1.5m$

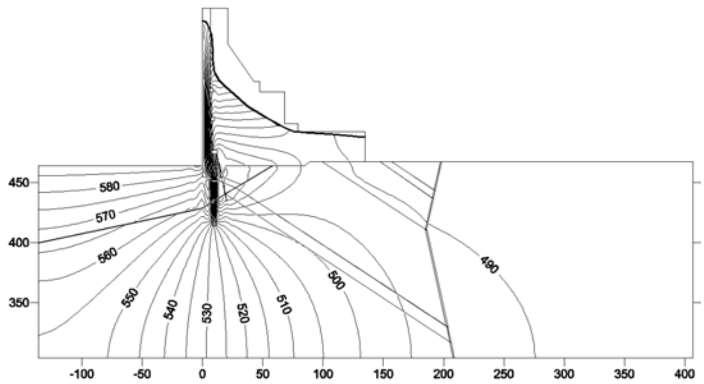

(b) FEM1, $y = 1.5m$

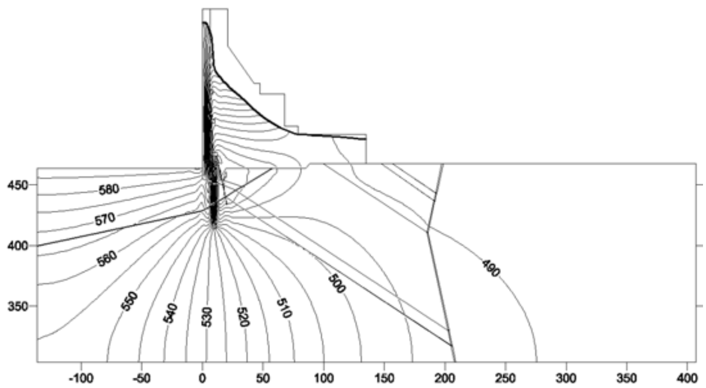

(c) FEM2, $y = 1.5m$

Fig.4.18 Hydraulic potential contour

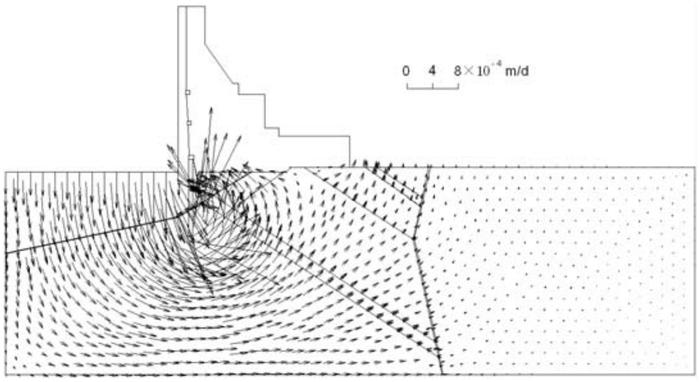

(a) CEM, $y = 1.5m$

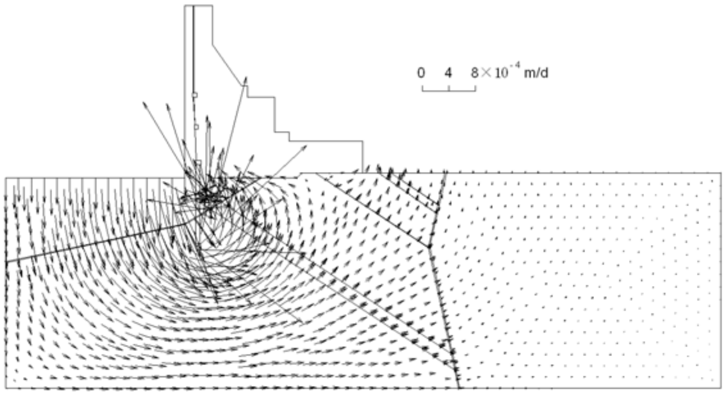

(b) FEM1, $y = 1.5m$

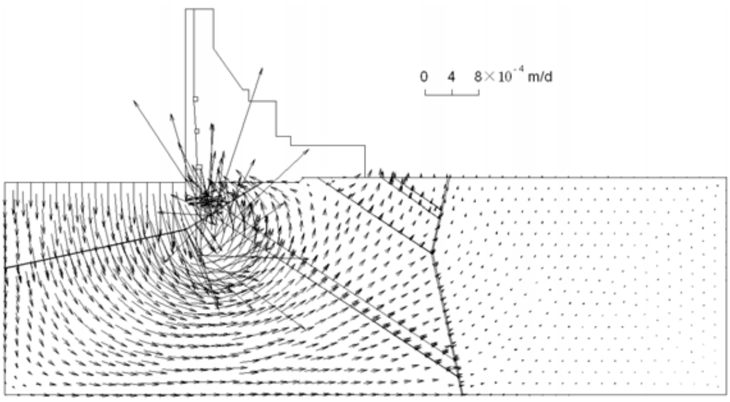

(c) FEM2, $y = 1.5m$

Fig.4.19 Flow velocity at the section *x-o-z*

Figs.4.21~4.22 show the hydraulic potential distribution along the fracture F8 respectively upside and downside F4, the results of the three models agree to each other. From Fig.4.22 to Fig.4.23, the tangential flow velocities along the typical fracture F8 are contrasted, in these figures the origins for measuring the distance at fractures are shown in Fig.4.12. It can be seen that:

- The flow velocity in the dam/foundation obtained by the FEM and the CEM are close. However, the difference is larger compared to the hydraulic potentials, because the flow velocity is “local ” and dependent strongly on the mesh density.

- The flow velocity in the fractures obtained by the FEM and the CEM is also close. It is found that at the intercross points of different fractures and fracture/seepage control system, the flow velocity undergo sudden change because of the complicated flow patterns in these areas.

- The results obtained by the equivalent model for drainage holes (FEM2) almost have the identical values compared with those obtained by the discrete model for the drainage holes (FEM1). And it is indicated that the FEM2 can satisfy the precision request when without fixing on the detailed results of the drainage holes, and the preprocess work for the drainage holes is much simpler.

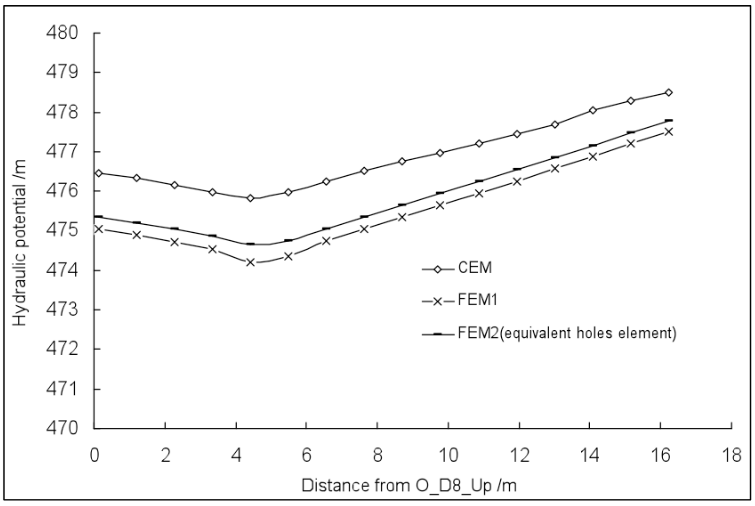

Fig.4.20 Hydraulic potential distribution along the fracture D_8 (upside of F_4)

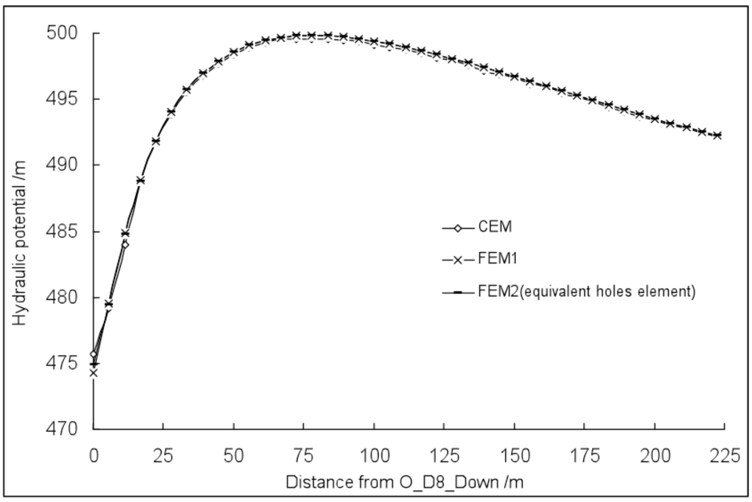

Fig.4.21 Hydraulic potential distribution along the fracture D_8 (downside of F_4)

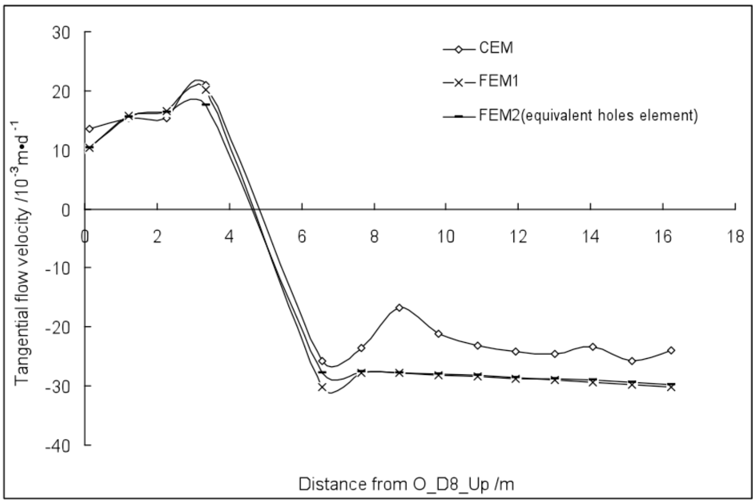

Fig.4.22 Flow velocity distribution along the fracture D_8 (upside of F_4)

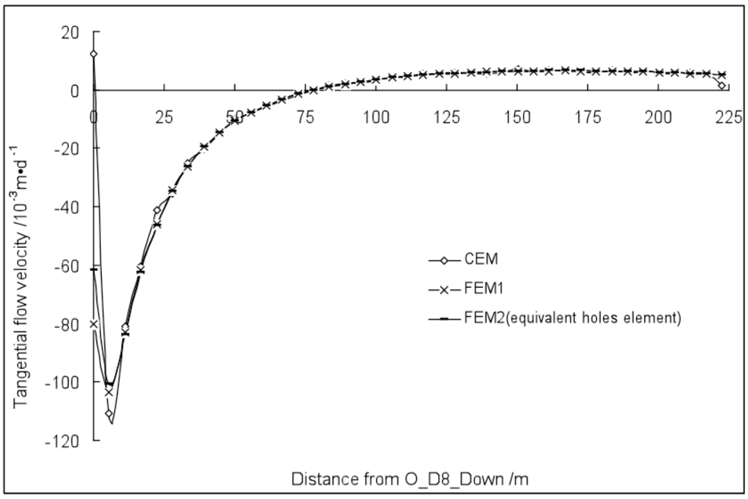

Fig.4.23 Flow velocity distribution along the fracture D_8 (downside of F_4)

Fig.4.24 shows the uplift distribution at the dam/foundation interface. It can be seen that, the uplifts at the dam/foundation interface by the FEM and the CEM are close. The seepage control system has obvious effects on the control of the uplift at the dam/foundation interface, in this way the stability of the dam can be improved.

The computer used in this study is：Microsoft Windows XP, Intel(R) Core(TM)2 Duo CPU E7200, 2.53 GHz，memory 1.95G RAM. The freedom and the computation time by FEM and CEM are shown in the Tab.4.8. It can be seen that the CEM uses extra calculation to replace a part of the pre-process works in FEM.

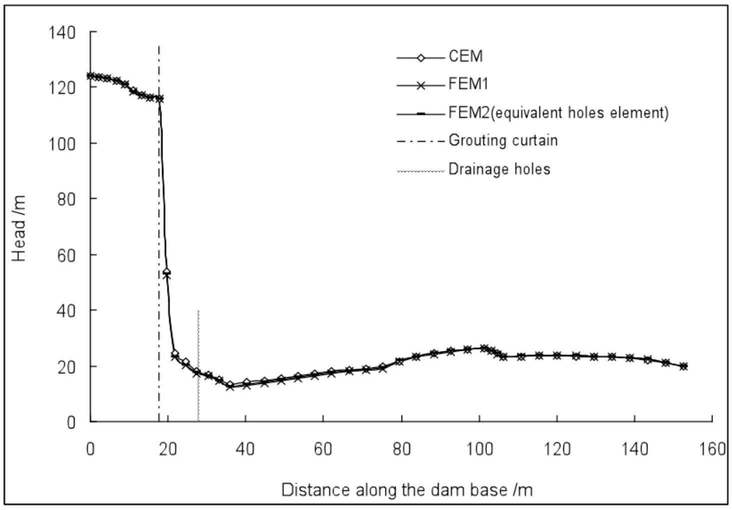

Fig.4.24 Uplift distribution at the dam/foundation interface

Tab.4.8 Computation time and freedom degree of the Baozhusi dam

	Freedom degree	Calculation time(s)
FEM	22307	807.05
CEM	9951	943.23

4.4 Summary of the chapter

This chapter includes the formulation of a composite element model for the fractured rock mass which are drained by hole array. If a composite element containing fracture and drainage hole segments simultaneously, the sub-elements of rock, drainage holes, fractures and interfaces will be defined. The hydraulic potentials within these sub-elements can be calculated by the corresponding nodal hydraulic potentials mapped on the composite element. By the variational principle, the governing equation for the mapped nodal hydraulic potentials can be established and integrated into conventional FEM algorithm.

The proposed algorithm in this chapter allows analysis of rock mass containing both fractures and drainage holes with more regular meshes. Theoretically, if the fractures, drainage holes as well as interfaces are properly discretized in the FEM, and the mesh density is adequate, it should provide results identical to that of CEM, because they have the same mechanics and mathematics basis. However, the main advantage of CEM compared to FEM is the simplicity in pre-processing: since the fractures and drainage holes are embedded within the composite elements, the mesh construction would not be limited them strongly, and the main attention in the pre-processing can be paid to the structure configuration and hydraulic potential gradient. Nevertheless, the disadvantages of the CEM are also obvious: the mathematics procedure and the software programming are more complicated, and more calculation time would be required because it uses extra calculation to replace a part of the pre-process works of FEM.

Chapter 5 Application to Xiaowan arch dam foundation

Composite element method (CEM) has its unique advantage on treating fractures, bolts, drainage holes and so on. The composite elements can cover the medium which has its own characteristics, and the variables of the sub-elements can be interpolated from the mapped elements through the shape function, that is, the fractures, bolts, and drainage holes have been simulated explicitly. The CEM also has notable advantages on simplifying the preprocess work, especially for the project with complicated configuration.

Xiaowan powerstation is located in the middle reaches of Lancang River, the west part of Yunnan province in China. Xiaowan dam is a concrete hyperbolic arch dam with variable thickness by parabola. Top elevation of the dam is 1245.0m, the lowest elevation of foundation is 950.5m, and the maximal height is 294.5 m. The upstream normal water level is 1240.0m, and the downstream water level is 1004.0m.

There are four important fractures across the foundation rock mass, named F7, F11, F10 and F5 respectively. Some fractures with small size are also well developed, especially for the two sets of steep fractures and one set of gentle fractures. The seepage control system has been deployed near the heel of the dam foundation, such as grouting curtain, main drainage holes curtain, subsidiary drainage holes curtain, and so on. Therefore, the numerical model of Xiaowan arch dam foundation system is much more complicated. In virtue of the simplified preprocess work of CEM, the 3-D numerical model is built firstly, then the seepage and stress coupling analysis can be carried out, and all the results are compared with those done by the finite element method (FEM), which can prove the efficiency and credibility of the CEM.

5.1 Application for the four important fractures

5.1.1 Computation conditions

Two 3-D meshes for Xiaowan arch dam-foundation system have been built: for the CEM model (Fig.5.1(a)), there are 90740 nodes and 100200 elements, of which 4788 are composite elements; for the FEM model (Fig.5.1(b)), there are 188600 nodes and 206062 elements. Fig.5.1(c)~(d) show the horizontal profile (z=1050.0m) based on the two meshes respectively, from which it can be seen that, the mesh for the FEM is more complicated, because all the fractures have been simulated explicitly by using specific elements.

Fig.5.2 shows the meshes of fractures based on the two methods. The CEM mesh is much simpler than that of the FEM, and the element size based on the FEM is much smaller than that based on the CEM, then the mesh generation by the FEM has been limited strongly. The main reason is that, the composite elements can cover the fractures explicitly (see Fig.5.2(a)), which will be embedded into the mapped elements automatically by the preprocess programs, but the finite elements need simulate the fractures explicitly through the specific elements, whose size must approach to the actual size of fractures (see Fig.5.2(b).

Fig.5.3 shows the layout of seepage control system, the fractures, rock zones M $^{-1}$, M $^{-2}$, M $^{-1}$, M $^{-3}$, P, and the main fractures F7, F11, F10, F5.

The global coordinate system is defined as: the axis x is across the river pointing at left bank, the axis y is along the river directing at upstream, and the axis z is vertical upwards.

The computation parameters of fractures and rock mass are given in the Tabs.5.1~5.3.

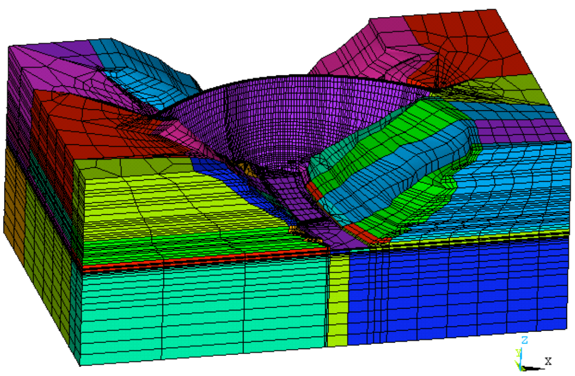

(a) Mesh based on CEM

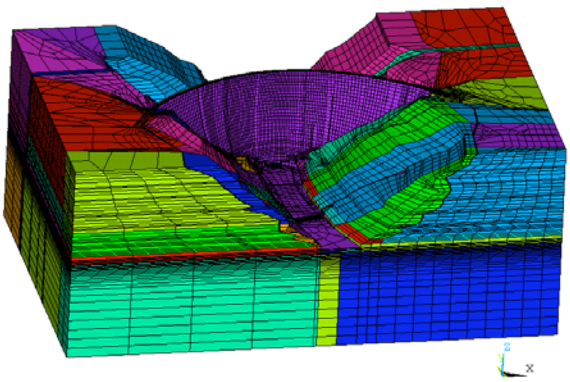

(b) Mesh based on FEM

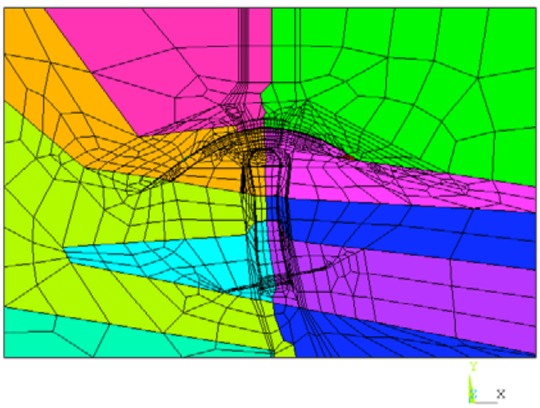

(c) Horizontal profile by CEM (z=1050m)

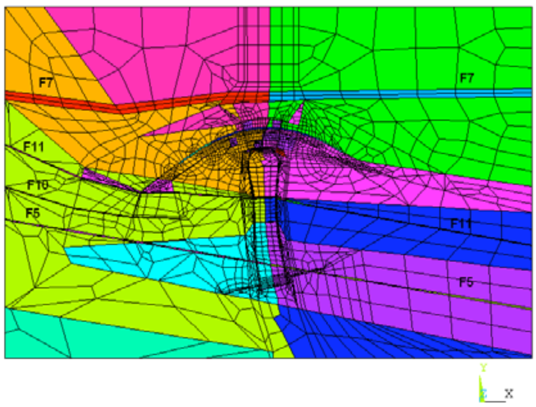

(d) Horizontal profile by FEM (z=1050m)

Fig.5.1 Computation meshes

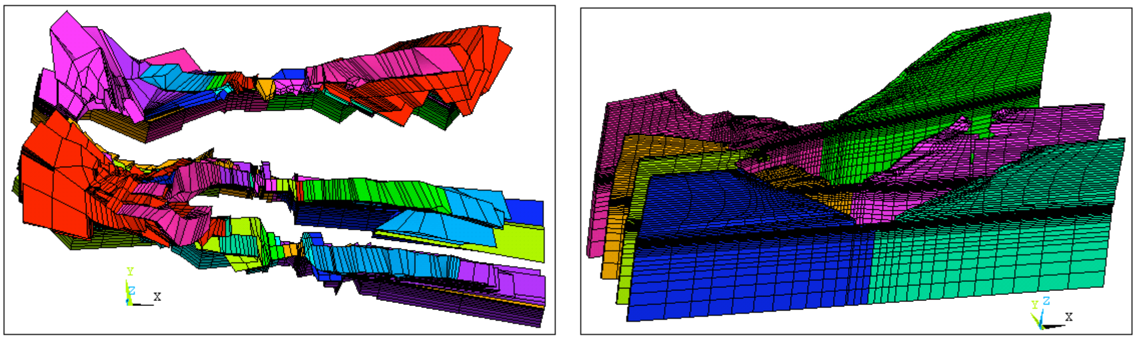

(a) Composite elements containing fractures (b) Mesh of fractures by FEM

Fig.5.2 Mesh of fractures

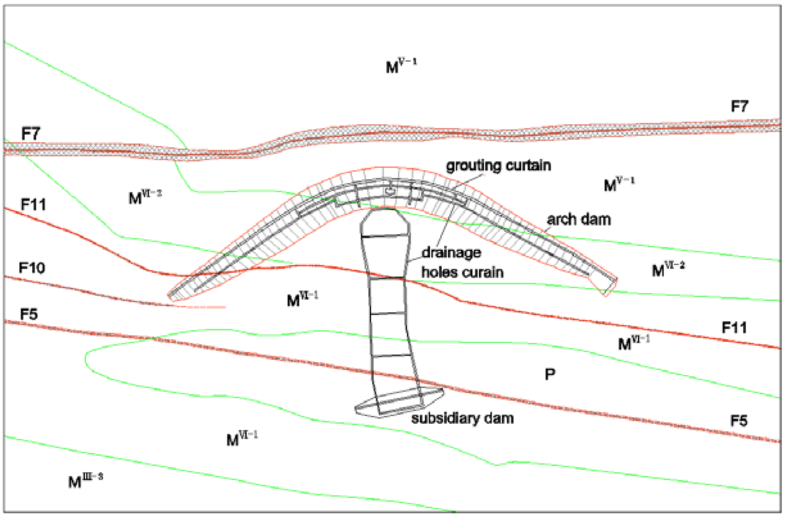

Fig.5.3 Layout of seepage control system and geology characteristics

Tab.5.1 Computation parameters of fractures

	ξ	φ_j /°	θ_j /°	CEM $k_{x_{jrlrm}}$ /(m·d^{-1})	CEM $k_{y_{jrlrm}}$ /(m·d^{-1})	CEM $k_{z_{jrlrm}}$ /(m·d^{-1})	CEM e /m	FEM k_{xx} /(m·d^{-1})	FEM k_{yy} /(m·d^{-1})	FEM k_{zz} /(m·d^{-1})	FEM e /m	FEM b /m
F7	0.6	357.95	90	3.3E-02	1.05E-02	2.85 E-02	4.0	5.5E-03	1.75E-03	4.75 E-03	4.0	24.0
F11	0.6	10.86	90	1.51E-02	4.80E-03	1.30 E-02	1.0	5.5E-03	1.75E-03	4.75 E-03	1.0	2.74
F10	0.6	9.26	90	1.00E-02	3.0E-03	9.00 E-03	1.0	5.0E-03	1.5E-03	4.5 E-03	1.0	2.0
F5	0.6	10.52	90	1.66E-02	5.27E-03	1.43 E-02	1.0	5.5E-03	1.75E-03	4.75 E-03	1.0	3.01

Tab.5.2 Mechanical parameters of foundation rock and dam concrete

	Young's modulus E/MPa	Poisson's ration μ	Coherence c /MPa	Angle of friction φ /(°)	Tensile strength σ_T /MPa	Volumetric weight γ /(kN·m^{-3})
concrete	23100	0.189	3.372	61.953	2.45	24
M^{V-1}	22000	0.26	2.0	56.31	1.6	25
M^{IV-2}	20000	0.27	1.8	54.462	1.44	25
M^{IV-1}	22000	0.26	2.0	56.31	1.6	25
M^{III-3}	20000	0.27	1.8	54.462	1.44	25
P	18000	0.28	1.6	54.462	1.28	25

Tab.5.3 Mechanical parameters of fractures

	Normal stiffness k_n/(MPa·m^{-1})	Shear stiffness k_s/(MPa·m^{-1})	Coherence c /MPa	Angle of friction φ /(°)	Tensile strength σ_T /MPa
F7	2000	870	0.1	26.5	0.01
F11	2000	870	0.1	26.5	0.01
F10	2000	870	0.1	26.5	0.01
F5	2000	870	0.1	26.5	0.01

5.1.2 Computation results

There are two computation cases, with and without considering the seepage and stress coupling respectively, and the comparative study using CEM and FEM has been carried out.

5.1.2.1 Permeability

Hydraulic potential contour at the section of crown cantilever arch dam (*x*=16.0m) is shown in the Fig.5.4, the distribution of the hydraulic potential contour by CEM and FEM are well agreed with each other. It is found that the contour lines are concentrated in the dam foundation region after considering the coupling. The main reason is that: on the one hand, the fracture F7 has a tendency to be opened by the *y*-component of tension, and the permeability of the fracture F7 increases; on the other hand, the fractures F11 and F5 are pressed by the *y*-component of compressive stress, and the permeability of the fractures decreases.

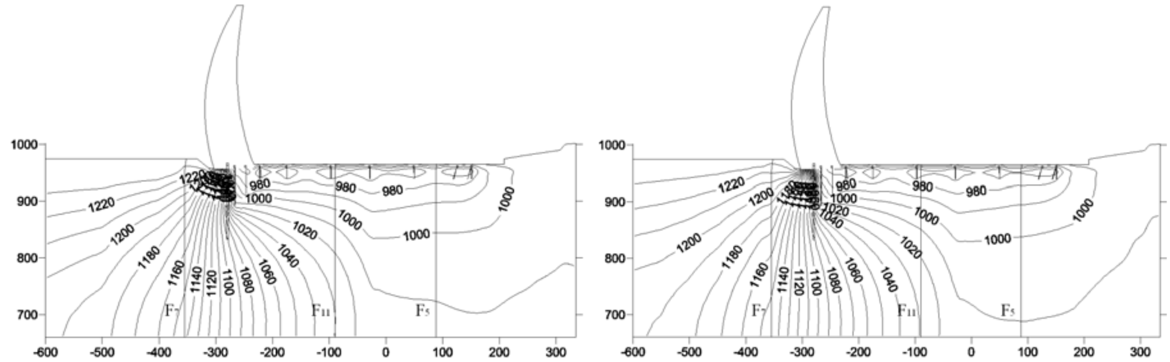

By CEM By FEM

(a) Hydraulic potential contour without coupling

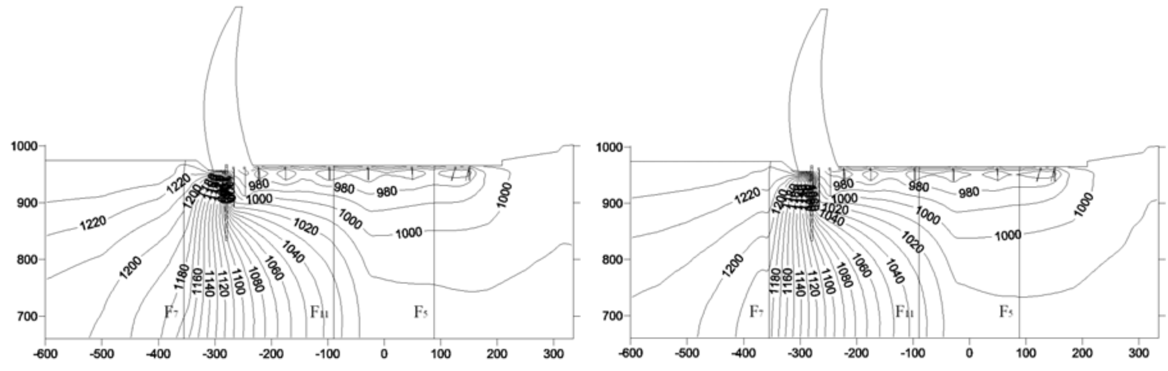

By CEM By FEM

(b) Hydraulic potential contour with coupling

Fig.5.4 Hydraulic potential contour at the section of crown cantilever arch dam (*x*=16.0m)

Fig.5.5 shows the seepage velocity vector of rock mass at the section of crown cantilever arch dam (*x*=16.0m), the results by the CEM close to those by the FEM. It can be seen that, the velocities of the upstream part decrease after considering the coupling, but the velocities of the downstream part increase after considering the coupling. The main reason is that, when considering the coupling, the fracture F7 is opened, leading to the decrease of seepage gradient, and the seepage velocity decreases accordingly; while the downstream fractures tend to be closed by the *y*-component of compressive stress, and the permeability characteristics decrease, leading to the increase of the seepage gradient, as well as the seepage velocity.

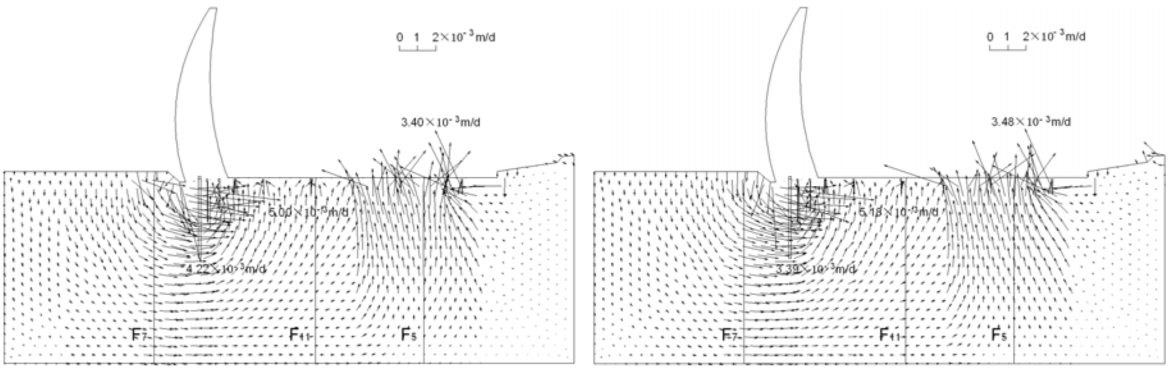

By CEM By FEM

(a) Seepage velocity without coupling

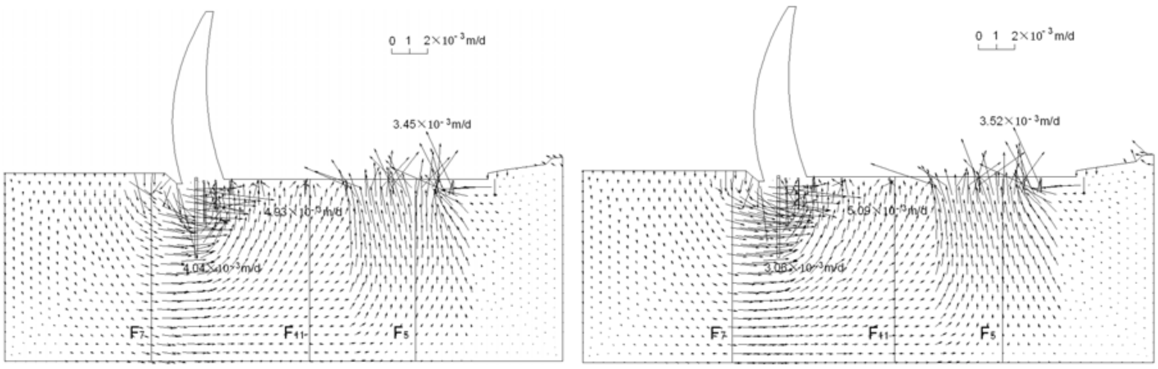

By CEM By FEM

(b) Seepage velocity with coupling

Fig.5.5 Seepage velocity of rock mass at the crown cantilever section (*x*=16.0m)

In the Figs.5.6~5.7, the hydraulic potential and seepage velocity along the fractures by the CEM are contrasted with those by the FEM at the crown cantilever section (*x*=16.0m). The results obtained by the CEM agree well with those obtained by the FEM.

From the Fig.5.6, it also can be seen that, when considering the coupling, the hydraulic potential along the fractures increases, especially at the low elevation. Because of the open tendency of the fracture F7 and the close tendency of the fractures F11 and F5, it makes the hydraulic potential contour shift to the downstream field.

The curve slope of hydraulic potential lines can show the value of seepage gradient. Therefore, the Fig.5.6 indicates that the seepage gradient along the fracture F7 decreases after the coupling, which can lead to the decrease of seepage velocity along the fracture F7 accordingly. It also indicates that the seepage gradient along the other fractures increase after the coupling, which can lead to the increase of seepage velocities accordingly, see the Fig.5.7.

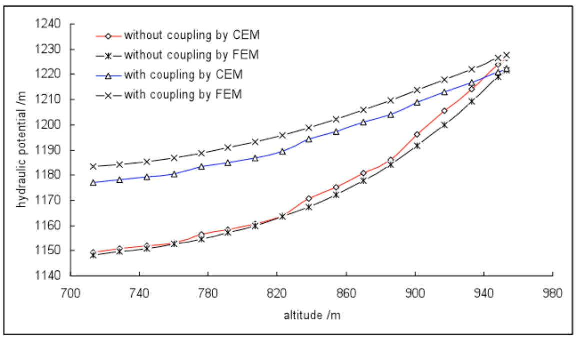

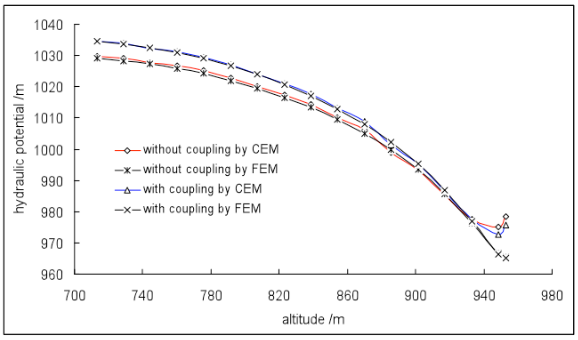

(a) Hydraulic potential along fracture F7 (b) Hydraulic potential along fracture F11

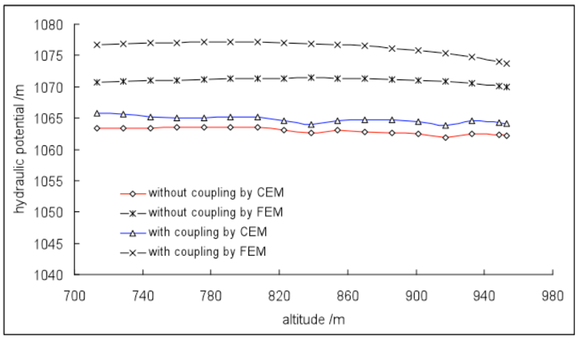

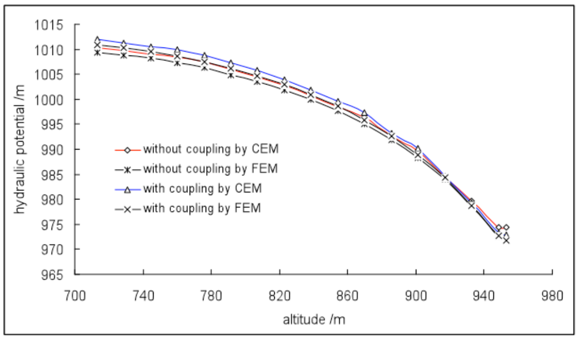

(c) Hydraulic potential along fracture F10 (d) Hydraulic potential along fracture F5

Fig.5.6 Hydraulic potential along the fractures at the crown cantilever section

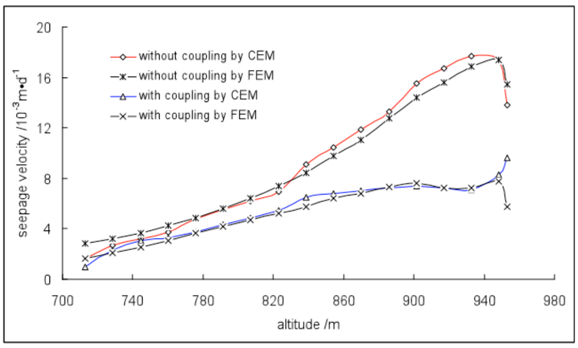

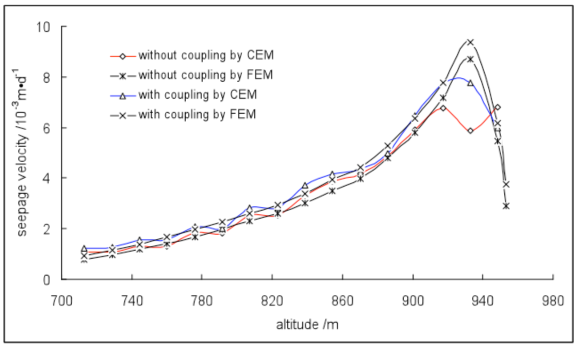

(a) Seepage velocity along fracture F7 (b) Seepage velocity along fracture F11

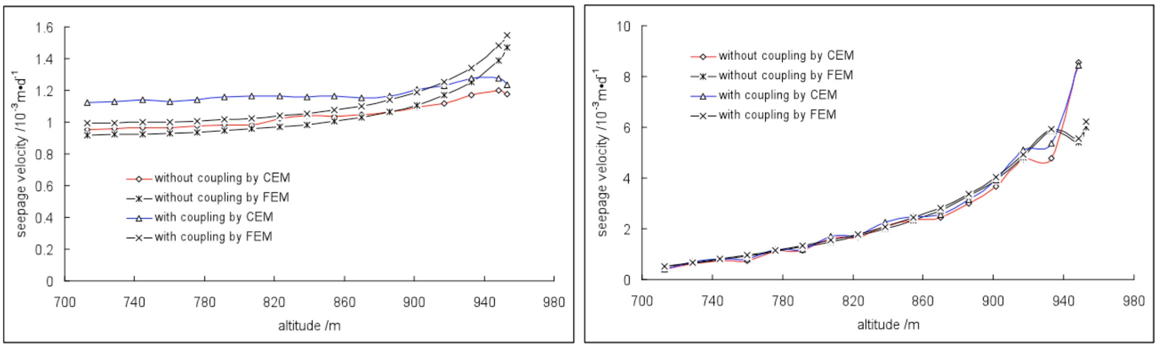

(c) Seepage velocity along fracture F10 (d) Seepage velocity along fracture F5

Fig.5.7 Seepage velocity along the fractures at the crown cantilever section

5.1.2.2 Stress

Contour of stress σ_y at the crown cantilever section (x=16.0m) is shown in the Fig.5.8, the results by the CEM are close to those by the FEM. Compared with the results without considering the coupling, there is almost no difference on the stress σ_y when considering the coupling, which indicates that the effect of stress on the seepage is more obvious than the effect of seepage on the stress.

The results of normal stress on the fractures by the CEM and FEM are compared with each other at the crown cantilever section (x=16.0m), shown in the Fig.5.9, the results are almost close to each other. The minor difference between the CEM and the FEM is because the precision of stress is dependent on the mesh density. From the Fig.5.9, it can be seen that, the normal stress σ_y on the fracture F7 increases after the coupling, and those on other fractures nearly do not change.

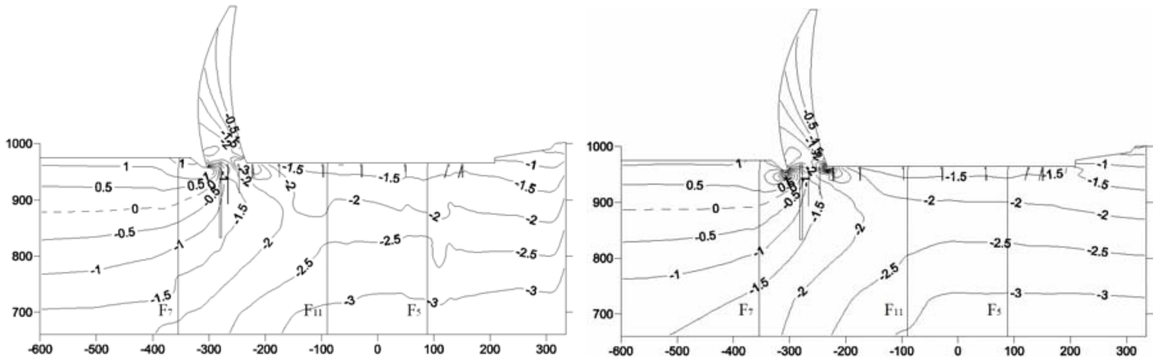

By CEM By FEM

(a) Contour of stress σ_y without coupling

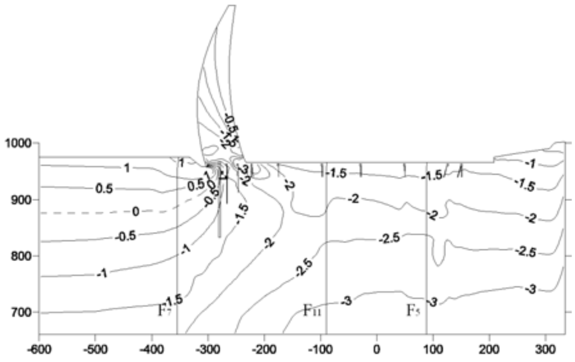

By CEM

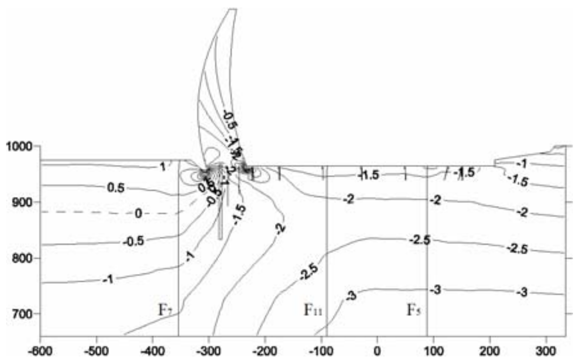

By FEM

(b) Contour of stress σ_y with coupling

Fig.5.8 Contour of stress σ_y at the crown cantilever section (positive for tension)

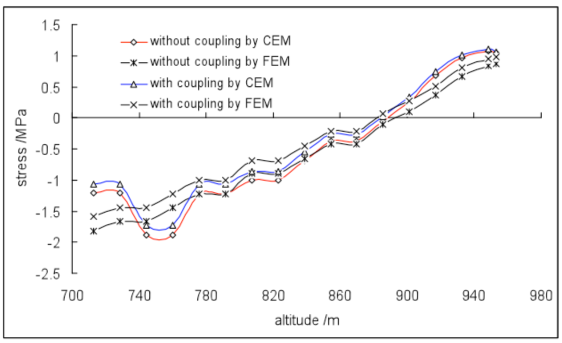

(a) Normal stress on the fracture F7

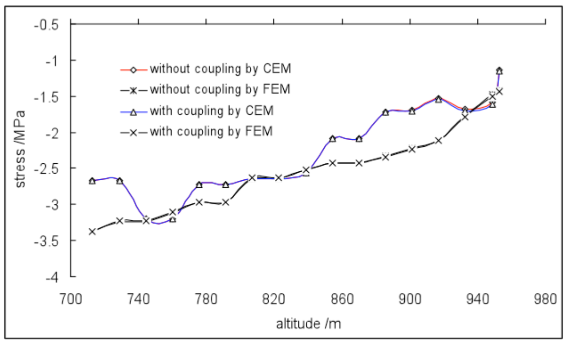

(b) Normal stress on the fracture F11

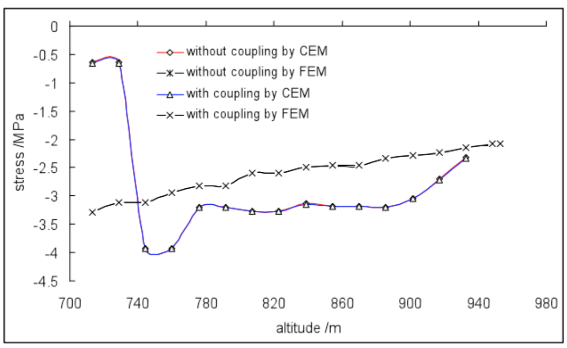

(c) Normal stress on the fracture F10

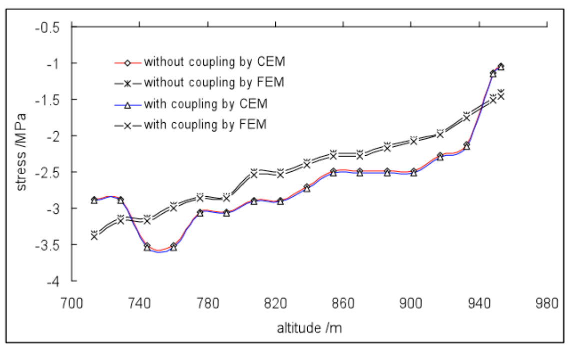

(d) Normal stress on the fracture F5

Fig.5.9 Normal stress distribution on the fractures at the crown cantilever section (positive for tension)

5.2 Application for fractured rock mass containing 3 sets of fractures

There are many visible fractures in the Xiaowan arch dam foundation rock mass, and they weaken the strength of foundation markedly, especially the two sets of steep fractures across and along the river, as well as one set of gentle fracture. Due to the tremendous water thrust at the upstream dam surface and the well developed fractures in the fractured rock mass, the steep fractures might be separated, and the water flows into the fractures. The uplift of upstream dam foundation increases, which can lead to the instability of the whole arch dam, and then the analysis on the seepage and stress coupling for fractured rock mass containing the three sets of fractures is also an important work.

5.2.1 Computation conditions

The three sets of fractures, grouting curtain, and the drainage holes are all simulated equivalently in the two numerical models, which are shown in the Figs.5.1~5.2.

5.2.1.1 Parameters of fractured rock mass

The statistical results for the fractured rock mass are shown in the Tabs.5.4~5.5.

Tab.5.4 Computation parameters for steep fractures

location	left bank					right bank				
	inclined direction /°	inclined angle /°	distance /m	aperture /mm	Connectivity / %	inclined direction /°	inclined angle /°	distance /m	aperture /mm	Connectivity / %
shallow	90	88	0.30	0.20	68.0	95	88	0.30	0.20	68.0
	10	80	0.35		78.2	10	80	0.35		78.2
middle	90	88	0.40	0.06	68.0	95	88	0.40	0.06	68.0
	10	80	0.45		78.2	10	80	0.45		78.2
deep	90	88	0.50	0.02	68.0	95	88	0.50	0.02	68.0
	10	80	0.45		78.2	10	80	0.55		78.2

Tab.5.5 Computation parameters for gentle fractures

Location	Elevation /m	Inclined direction /°	Inclined angel /°	Space /m			Aperture /mm			Connectivity / %
				Shallow	Middle	Deep	Shallow	Middle	Deep	
Left bank	1245~990	275	30	0.93	1.34	1.84	0.20	0.06	0.02	63.14
	990~975	270	19							
	975~950.5	270	16							
	Under 950.5	90	0							
Right bank	1245~1050	83	31	1.02	1.94	2.14				
	1050~975	79	25							
	975~950.5	90	19							
	Under 950.5	90	0							

5.2.1.2 Parameters of grouting curtain

Thickness of grouting curtain is dependent on its permeability stabilization, and it is related to the row quantity of grouting holes, rows space, and holes space. In the Xiaowan project, for the upstream grouting curtain, there are three kinds of grouting holes, single row holes, double-row holes and three rows holes, see in the Fig.5.10. The holes space is 2m, rows space is 1.5m. Both of the subsidiary dam and water cushion pool have only one single row of grouting holes, and holes space is 3.0m.

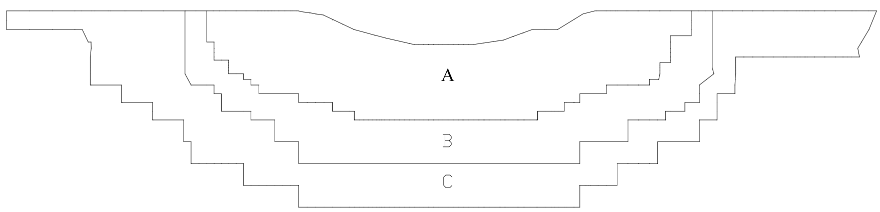

Fig.5.10 Sketch for upriver grouting curtain

(A—three rows holes region; B—double-row holes region; C—single row holes region)

According to the experimental tests and the required seepage gradient, the permeability coefficient of grouting curtain is adopted as k_w=1.5E-04m/d. In order to simplify the mesh generation, the thickness of grouting curtain in the numerical model is defined uniformly as L=4.0m. Based on the equivalent flow rate principle, head loss across the grouting curtain is denoted as ΔH, the equivalent permeability coefficient k for grouting curtain elements can be obtained as the following equations.

$$k_w \frac{\Delta H}{l} = k \frac{\Delta H}{L} \tag{5-1}$$

Where l is actual thickness of grouting curtain, L is the numerical thickness of grouting curtain. Thus the equivalent permeability coefficient for grouting curtain in numerical model is given by:

$$k = k_w L / l \tag{5-2}$$

Permeability coefficients of grouting curtain are shown in the Tab.5.6.

Tab.5.6 Permeability coefficients of grouting curtain

Location	True thickness l /m			Numerical thickness L /m	Single row /m·d	Double-row /m·d	Three rows /m·d
	Single row	Double-row	Three rows				
upstream	1.5	2.8	4.3	4.0	4.000E-4	2.143E-4	1.395E-4
Water cushion pool	2.25	/	/	2.0	1.333E-4	/	/
Subsidiary dam	2.25	/	/	2.0	1.333E-4	/	/

5.2.1.3 Parameters of drainage holes curtain

Based on the theory of drainage holes replaced by the drainage holes curtain, the drainage holes are simulated equivalently in the two models, considered as drainage holes curtain. Like the grouting curtain, thickness of drainage holes curtain is defined as B=0.5m uniformly in the numerical model, then according to the Eq.(4-48), the equivalent permeability coefficients of drainage holes curtain can be obtained.

5.2.2 Computation results

Boundaries of the left-right banks and the bottom surface are insulated, that is to say, the research field for the arch dam-foundation system has no flow exchange with the around mountain body. Both the upstream and downstream boundary surface are the specified hydraulic potential boundary, at the upstream surface it is fixed to be equal to the normal water level 1240m, and at the downstream surface it is fixed to be equal to the downstream water level 1005m. As well as the gallery boundary surface, it is also specified hydraulic potential boundary, which is dependent by the z coordinate. The downstream reservoir and dam surface above downstream water level is supposed as overflow boundary condition firstly, and the actual overflow surface can be obtained through the iterative calculation.

There are two kinds of loads taken into account, gravity and water load. At the arch dam surface, the water load is considered as surface load, but at the foundation, it is considered as volumetric load.

There are also two calculation cases. One does not consider the seepage and stress coupling, and the other considers the coupling. All the obtained results are compared between the CEM and the FEM. The coupling analysis of Xiaowan arch dam-foundation system is mainly projected at the crown cantilever section (x=16.0m).

Fig.5.11 shows the hydraulic potential contour after the coupling, at the crown cantilever section (x=16.0m). It can be seen that, the results obtained by the two methods are almost the same. By comparison of the Fig.5.4 and the Fig.5.11, it also can be seen that, when considering the coupling with the three sets of fractures, the coupling effect is more remarkable, and the upstream hydraulic potential increases remarkably, because the steep fractures are open under the great water thrust, and more water flows into the fractures.

Fig.5.12 shows the uplift of the dam base surface, and the results of the two methods almost have the identical values. It can be seen that, when the coupling is taken into consideration, the uplift of the dam heel has the tendency to equal to the design value, that is, approach to the full head. The uplift of the subsidiary dam is much smaller than the design value, because the hydraulic head loss is not considered in the design value, but actually there is a hydraulic head loss, due to the big distance from the subsidiary dam base to the downstream reservoir surface.

It is also indicated that, the uneven permeability characteristics resulting from the stress is remarkable, and the seepage and stress coupling plays an important role in the stability of dam foundation. If the coupling is not taken into account, the safety of the whole arch dam foundation system might be misled.

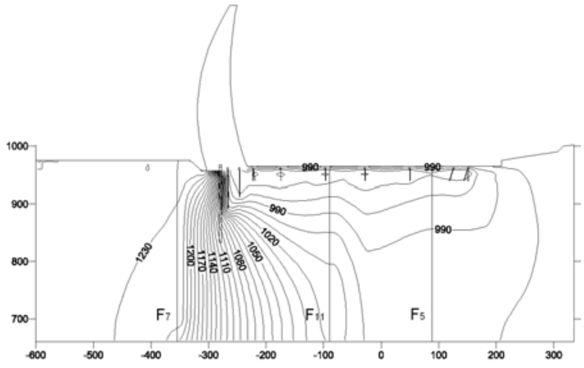

(a)By CEM

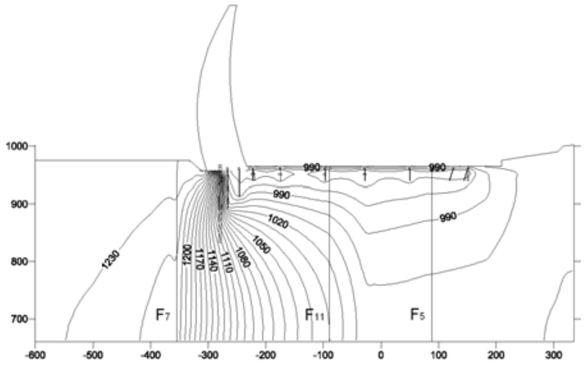

(b)By FEM

Fig.5.11 Hydraulic potential contour with coupling (*x*=16.0m)

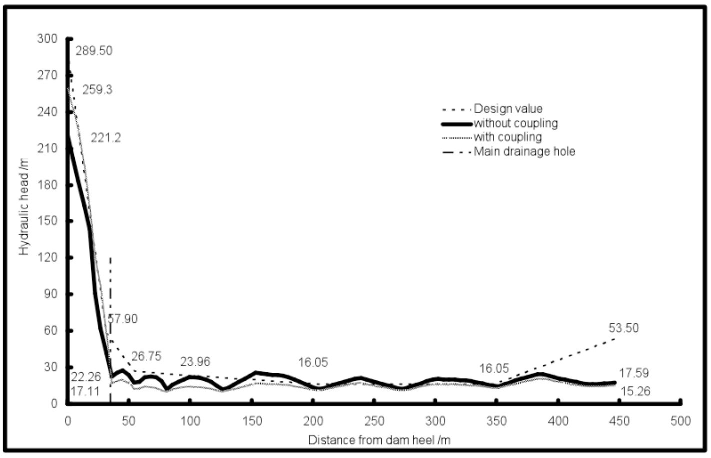

(a)By CEM

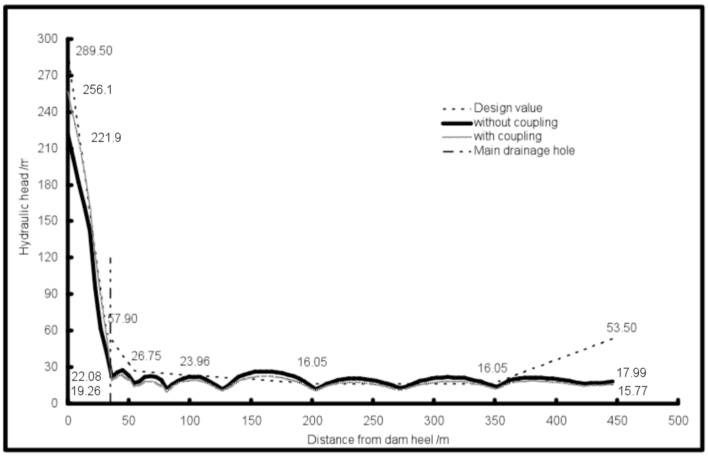

(b)By FEM

Fig.5.12 Uplift of the dam base surface (*z*=950.5m, *x*=16.0m)

Fig.5.13 shows the seepage gradient vector at the crown cantilever section (x=16.0m), the results of the two methods are close to each other. It can be seen that, when consider the coupling, the seepage gradient before the upstream grouting curtain increases, the maximum value from 3.34 to 5.01 by the CEM, from 3.36 to 4.97 by the FEM. But the seepage gradients of the upstream field are almost equal to zero, because the upstream steep fractures are open by the great water thrust, and the water flows into the fractures, then the hydraulic potential of the upstream field has a tendency to approach the upstream water level, and the hydraulic potential contour lines are concentrated to the upstream dam foundation field after the coupling.

The seepage gradient of deeper dam foundation area increases as well, mainly because the steep fractures are closed by the *y*-component compressive pressure, as well as the gentle fracture closed by *z*-component compressive pressure, and then it is difficult for the water flow through the foundation, and the permeability characteristics decrease.

From the Fig.5.13, it also can be seen that, when consider the coupling, the maximum seepage gradient of grouting curtain decreases from 16.04 to 11.78 by the CEM, and from 15.69 to 11.16 by the FEM, and the seepage gradient behind the grouting curtain also decreases. Because the fractures behind the grouting curtain are closed by the *y*-component pressures, and the fractured rock mass can be regarded as a great impermeability curtain, then the impermeability role of the grouting curtain has been shared by the downstream fractured rock mass.

Fig.5.14 shows the seepage gradient contour of grouting curtain, the results obtained from the two methods agree with each other. It can be seen that, the seepage gradient of grouting curtain decreases after the coupling, the rule is consistent with that of seepage gradient at the crown cantilever section (see Fig.5.13). The main reason is that, the fractures behind the grouting curtain are closed, and the downstream fractured rock mass becomes to be one great impermeability curtain, which weakens the impermeability role of the grouting curtain.

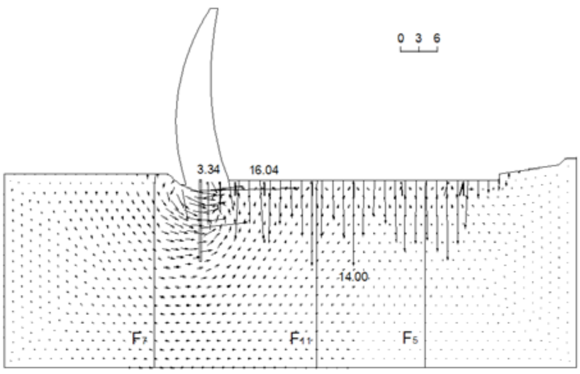

By CEM

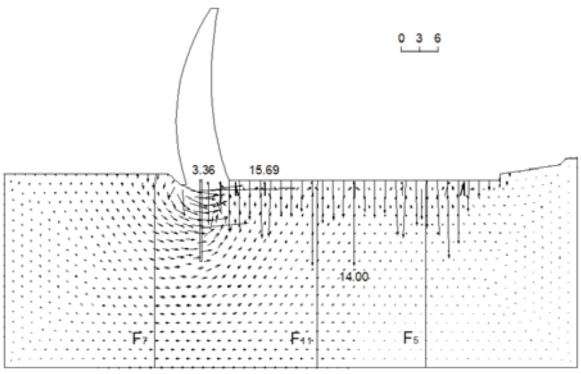

By FEM

(a) seepage gradient vector without coupling

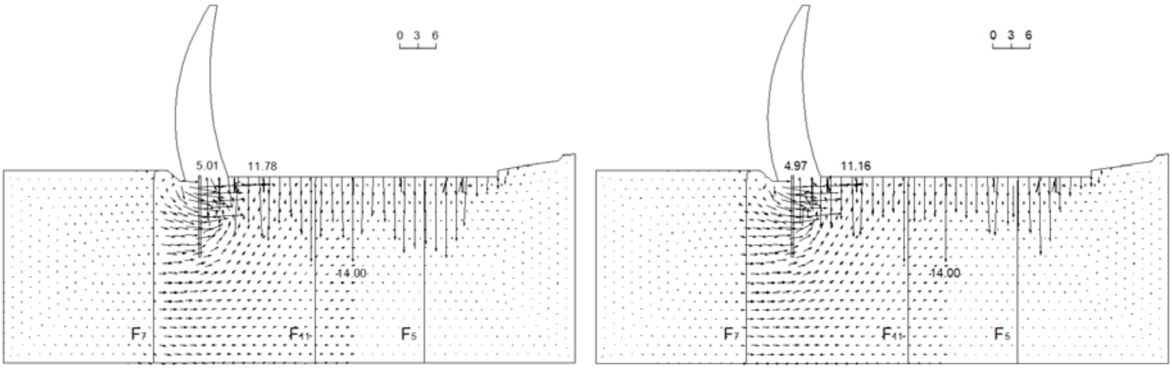

By CEM By FEM

(b) seepage gradient vector with coupling

Fig.5.13 Seepage gradient vector (*x*=16.0m)

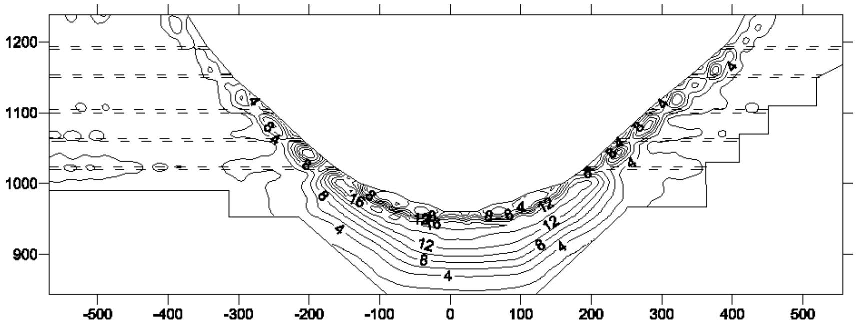

By CEM

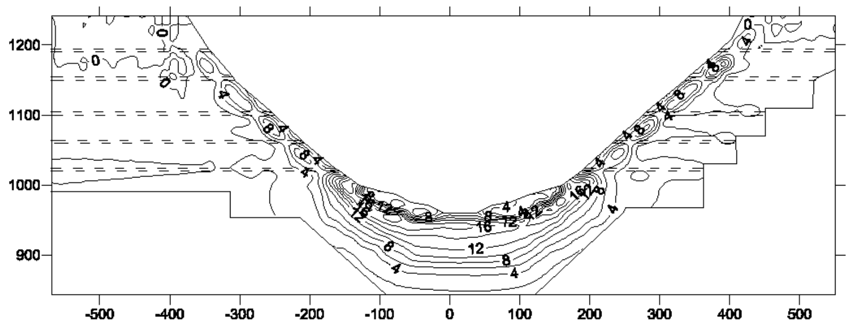

By FEM

(a) seepage gradient contour of grouting curtain without coupling

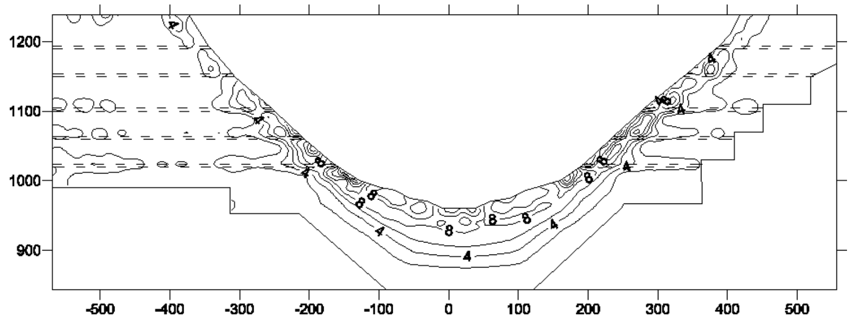

By CEM

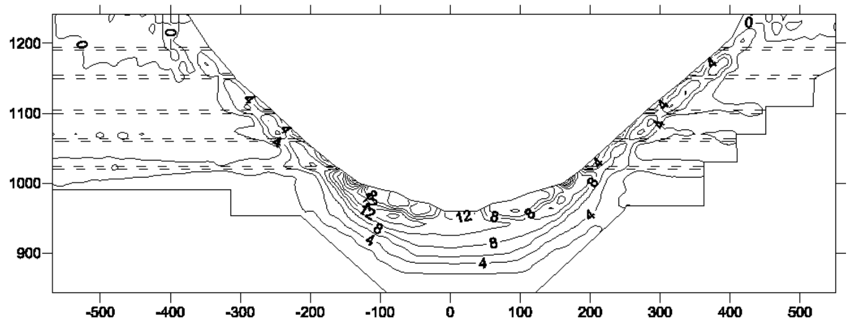

By FEM

(b) seepage gradient contour of grouting curtain with coupling

Fig.5.14 Seepage gradient contour of grouting curtain

Fig.5.15 shows the seepage velocity at the crown cantilever section (x=16.0m), the results obtained by the CEM agree exactly with those obtained by the FEM. Compared with the Fig.5.5, it can be seen that, when consider the coupling effect of the three sets of fractures, the seepage velocities of dam foundation area increase. It is mainly because the permeability coefficients of the fractured rock mass containing the three sets of fractures increase markedly after the coupling, although the seepage gradients decrease, the seepage velocities of the dam foundation field still increase. It also can be seen that, the seepage velocities of upstream field decrease almost equal to zero, because the water flows easily into the open fractures in the upstream foundation field, and the hydraulic head approaches to the full head, and the seepage gradients are almost equal to zero.

Fig.5.16 shows the overflow surface contour, the results of the two methods are close to each other. By comparison between with and without the coupling, it can be found that, the hydraulic potential of the upstream foundation increases obviously, and the overflow surface has a tendency to move towards to the downstream, it indicates that the water flows into the upstream foundation, where the hydraulic potential approaches to the upstream water level.

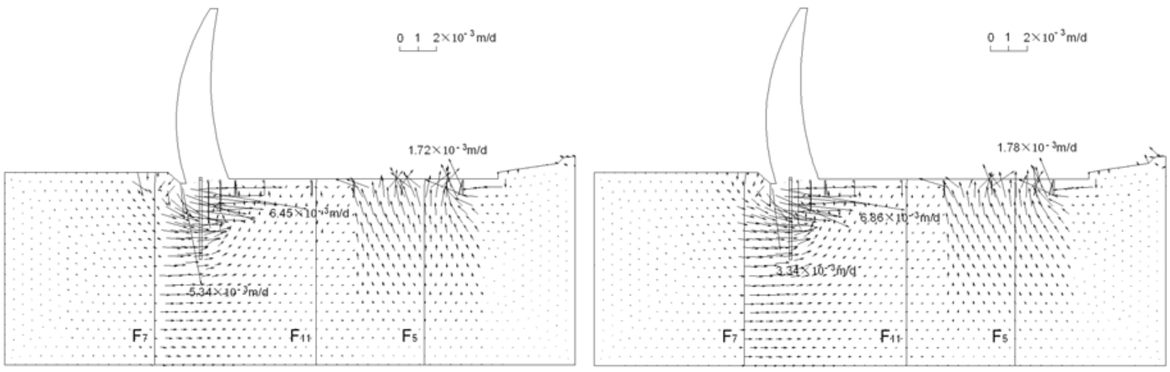

(a)By CEM (b)By FEM

Fig.5.15 Seepage velocity vector with coupling (x=16.0m)

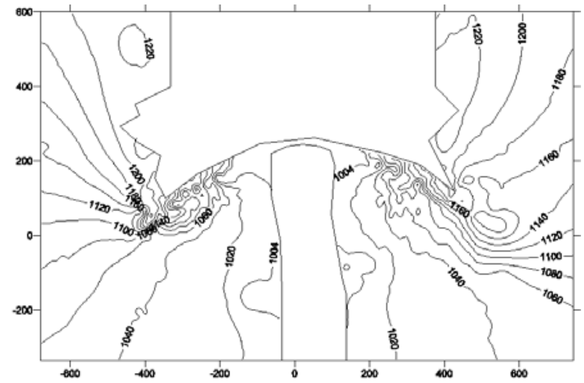

By CEM

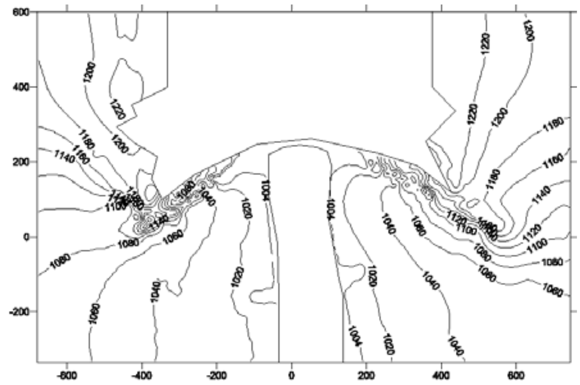

By FEM

(a) overflow surface contour without coupling

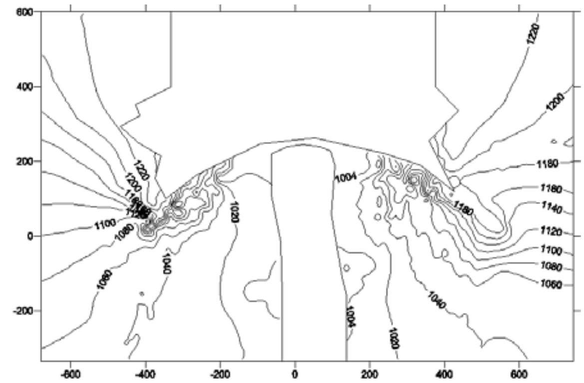

By CEM

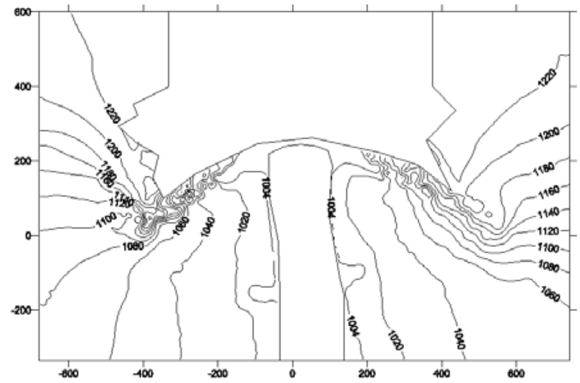

By FEM

(b) overflow surface contour with coupling

Fig.5.16 Overflow surface contour

5.3 Application for fractured rock mass containing drainage holes

5.3.1 Computation conditions

Xiaowan arch dam foundation has one complicated drainage control system, including main drainage holes, sub drainage holes, drainage holes for bank slope, drainage holes for water cushion pool, drainage holes for subsidiary dam, and so on (see Fig.5.3).

Because the size of drainage holes is very small, it is very difficult to be simulated explicitly, especially for the mesh generation. Even if the mesh generation is finished constrainedly, it might be with bad topological configuration. However, the drainage holes can be embedded within the elements based on the CEM, without considering the exact position and direction.

Only the main drainage holes at the river bed dam section are simulated by the CEM (see Fig.5.17), because these drainage holes are the most important ones, and its detailed results need to approach the actual solution as close as possible. The diameter of the drainage holes D=0.15m, the space distance l=3.0m, and there are 108 composite elements containing 264 holes sub elements (see Fig.5.17(b)). The central axis position of the holes sub-element is shown in the Fig.5.18. According to the results in the chapter 4.3.3.2, the equivalent simulation for the drainage holes can satisfy the request engineering precision, therefore, the drainage holes of other research field are simulated equivalently.

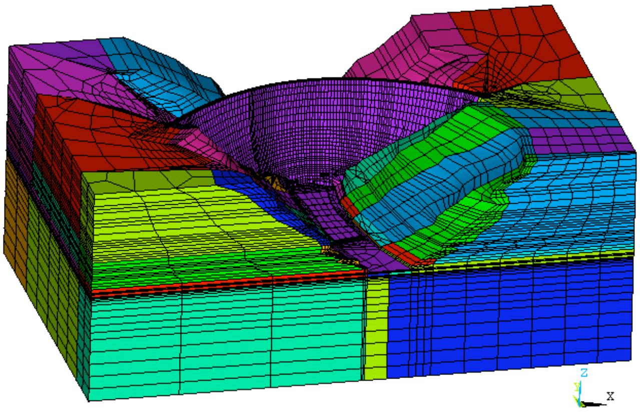

(a) Mesh of the whole model

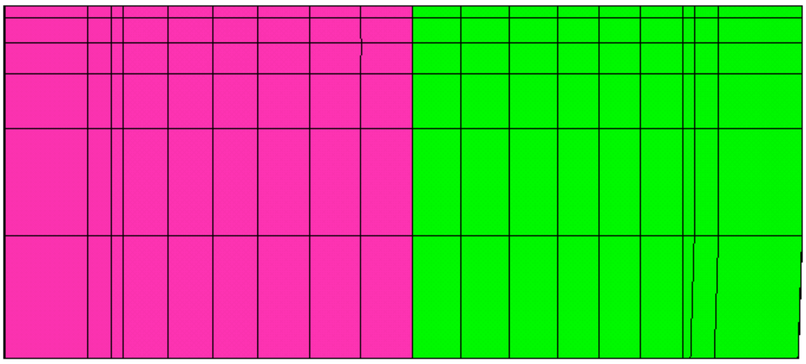

(b) Mesh of composite elements containing holes

Fig.5.17 Mesh of composite element method

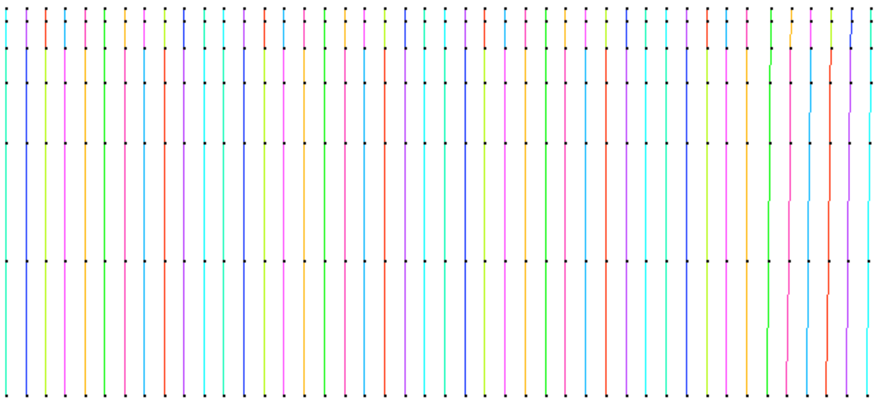

Fig.5.18 Central axis position of holes sub elements

5.3.2 Computation results

The calculation parameters are the same with the former models. The seepage and stress coupling is taken into account, with considering the four important fractures and the three sets of fractures, and the comparative study between the CEM and the FEM is carried out.

Fig.5.19 shows the hydraulic potential contour at the crown cantilever section (x=16.0m) by the CEM. Compared with the Fig.5.4(a), Fig.5.11(b), it can be seen that, the results obtained by the two methods agree with each other, and the hydraulic potential contour lines are concentrated to the dam foundation field.

Fig.5.20 shows the uplift of the dam base surface, compared with the Fig.5.12(b), it is found that, the uplifts of the two methods almost have the identical values.

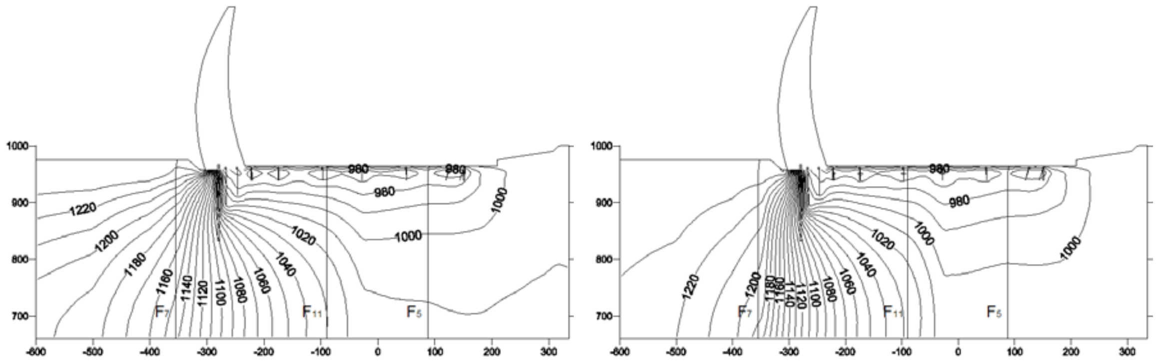

(a)without coupling (b)with coupling

Fig.5.19 Hydraulic potential contour of crown cantilever section (*x*=16.0m)

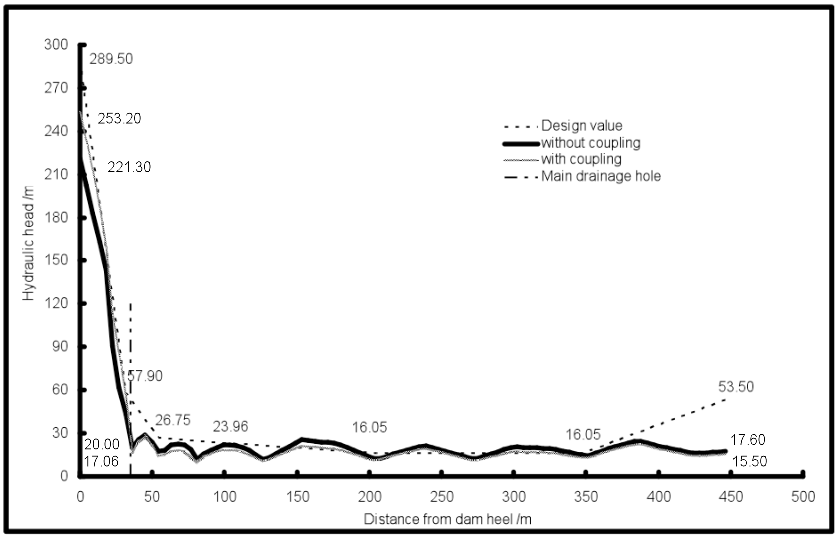

Fig.5.20 Uplift of the dam base surface (*z*=950.5m, *x*=16.0m)

Fig.5.21 shows the seepage velocity vector by the CEM, compared with the Fig.5.5(a), Fig.5.15(b), it can be seen that, the results obtained by the CEM are close to those obtained by the FEM.

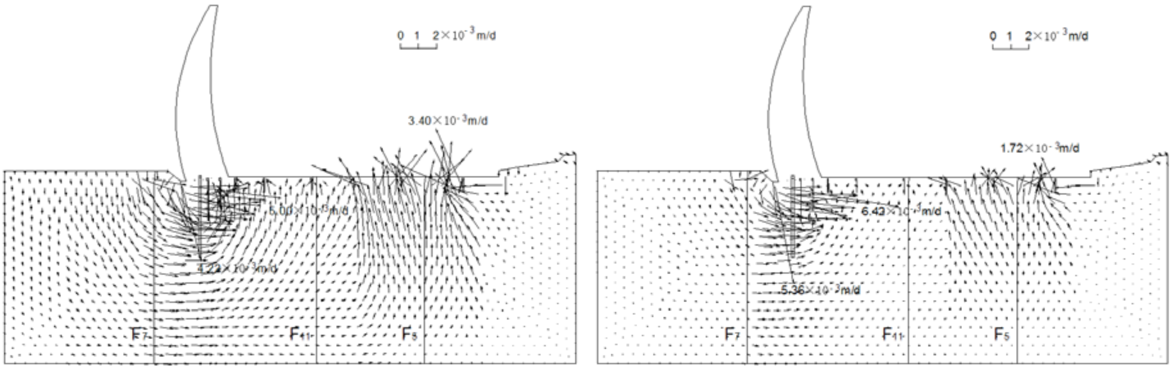

(a)without coupling (b)with coupling

Fig.5.21 Seepage velocity vector of crown cantilever section(*x*=16.0m)

5.4 Summary of the chapter

In this chapter, the applications to Xiaowan arch dam-foundation system have been carried out in turn respectively, for the four important fractures, fractured rock mass containing 3 sets of fractures, and fractured rock mass containing drainage holes. A careful comparison is made between the CEM and the FEM.

Firstly, the numerical models based on the CEM and FEM have been built. In the CEM model, the four main important fractures and the main drainage holes at the river bed dam section have been simulated implicitly, embedded into the composite elements. In the FEM model, the four main important fractures are simulated discretely, and the drainage holes are considered as drainage holes curtain. But the FEM mesh is more complicated and more difficult to be generated.

According to the comparative study among the computation results, it can be seen that, the results obtained by the two methods agree with each other. The seepage and stress coupling algorithms of fractured rock mass and fractured rock mass containing drainage holes by the CEM have been well verified by the complicated application, from which the efficiency and credibility of the proposed coupling algorithms have been shown obviously.

Chapter 6 Conclusion

There is an important coupling relationship between seepage field and stress field for fractured rock mass, as the two fields take interaction with each other, and influence each other inversely. So far, there have been some numerical models on the seepage and stress coupling for fractured rock mass, such as conventional equivalent continuum model, fracture network model, fracture and porous media model, and so on, and each model has its own advantages and disadvantages. The equivalent continuum model is very simple, but the detailed simulation is too simple to put into application (such as REV limit), and the simulation for the flow exchange between the fracture and adjacent rock block is also too much simplified. The fracture network model can simulate the fracture network more detailed, but it neglects the flow exchange between the fracture and rock block. The fracture and porous media model makes further development in the simulation of flow exchange between the fracture and adjacent rock block, but there are still some shortcomings in simulating specific fracture network, and the flow exchange rule between the fracture and rock block is difficult to be confirmed. The CEM is a new numerical method, which does not have the advantages of the former three models, but also has overcome some their shortcomings. This dissertation has taken some researches on the seepage and stress coupling algorithm of fractured rock mass based on the CEM, in which the advantages and the developed prospect can be well shown.

The research results of the dissertation can be briefly summarized as follows:

(1)Based on the filled model, the seepage and normal stress coupling algorithm of fractured rock mass has been proposed by the CEM, which is an important extension of CEM. The newly proposed coupling algorithm can be used for both the filled and unfilled fractures, and the flow exchange between the fracture and adjacent rock block has been taken into account.

(2)Based on the CEM, the seepage and stress coupling algorithm of fractured rock mass during the shear process has been established. The shear process has been divided into three phases: shear shrink phase, shear dilation up to peak value phase, and residual shear strength phase.

(3)Based on the CEM, the seepage and stress coupling algorithm of fractured rock mass containing drainage holes has been proposed, in which both the fractures and drainage holes are simulated explicitly, embedded into the composite elements with considering the deformation and permeability characteristics.

(4)The FORTRAN programs have been written for all the proposed algorithms.

(5)By comparison with the FEM, all the proposed coupling algorithms have been verified by the simple numerical examples firstly, in which the reliability and advantages of the algorithms have been well shown. There is adequate attention paid to the detailed simulation for the fractures and drainage holes, and the deformation and permeability characteristics of the fractures can be shown actually, especially for the seepage velocity, which is much closer to the actual solutions compared with the results obtained by the FEM.

(6)All the proposed coupling algorithms have been applied to Xiaowan arch dam foundation system with complicated configuration, from which the reliability, efficiency and advantages have been well shown.

Indeed, the seepage and stress coupling algorithm of fractured rock mass is still one hot and complicated problem in the rock hydraulics. Although some accomplished researches on the fractured rock mass have been presented in this dissertation, there is still room for further development, such as:

(1)If there is enough financial aid and advanced experimental technology, the experiment on the fractured rock mass should be carried out, with taking the seepage and stress coupling effect into account. Then the reliability of the proposed algorithm for fractured rock mass can be strongly verified.

(2)The seepage and stress coupling algorithm during the shear process should be further improved, especially for the residual shear strength phase, which is a plastic phase. Whether the big deformation method should be applied in this phase needs to be discussed as well.

(3)The mathematics procedure and the software programming are more complicated, and more calculation time would be required because it uses extra calculation to replace a part of the pre-process works of FEM.

(4)The P-version self-adaptive can be applied to improve the calculation precision of the proposed coupling algorithms, especially at the crossing part of fractures.

(5)The seepage, stress and thermal coupling algorithm of fractured rock mass can be established based on the proposed algorithm in this dissertation. Also, the proposed coupling algorithm can be further extended to nuclear waste deposit project, because how to simulate the permeability and deformation characteristics for the nuclear waste deposit configuration as actual as possible is still a problem.

(6)The proposed coupling algorithm also can be further developed to research on the fracture propagation, due to the actual simulation on the deformation and permeability characteristics of fractures.

The seepage and stress coupling algorithm of fractured rock mass by the CEM has a brilliant prospect, because the preprocess work is very simple and convenient, which can take the deformation and permeability characteristics into account without considering the shape and exact position of fractures, and the obtained results are quite satisfactory. Still there is much more to do to be better.

References

[1] Andersson J, Dverstorp B. Conditional simulation of fluid flow in three-dimensional networks of discrete fractures. *Water Resources Research.* 1987;23(10):1876-1886

[2] Aoki K, Shiogama Y, Tezuka Y, Kobuchi T, Masumoto K. Evaluation of hydraulic conductivity of jointed rock mass by cross hole permeability test. *In: Proceeding. 7th Int. Cong. ISRM*. 1992; 423-426

[3] Bai M, Elsworth D. Modeling of subsidence and stress-dependent hydraulic conductivity for intact and fractured porous rock. *Rock Mechanics and Rock Engineering*. 1994;27(4):209-234

[4] Bandis S, Lumsden A C, Barton N R. Experimental studies of scale effects on the shear behavior of rock joints. *International Journal of Rock Mechanics and Mining Sciences and Geomechanics Abstracts*. 1981;18(1):1-21

[5] Barenblatt G I, Zheltov I P, Kochina I N. Basic Concepts in the Theory of Seepage of Homogenous Liquids in Fissured Rocks. *Journal of Applied Mathematics and Mechanics.* 1960; 24(5): 1286-1303

[6] Barton N R. The shear strength of rock and rock joints. *International Journal of Rock Mechanics and Mining Sciences and Geomechanics Abstracts*. 1976; 13(9):255-279

[7] Barton N, Choubey V. The shear strength of rock joints in theory and practice. *Rock Mechanics*. 1977;10(1/2):1-54

[8] Barton N, Bandis S. Effects of block size on the shear behavior of jointed rock. *Proc. of the 23rd US Symposium on Rock Mechanics*. Rotterdam：A. A. Balkema. 1982: 739-760

[9] Barton N, Bandis S, Bakhtar K. Strength, deformation and conductivity coupling of rock joints. *International Journal of Rock Mechanics and Mining Sciences and Geomechanics Abstracts,* 1985;22(3): 121-140

[10] Cacas M C, Ledoux B, Marsity G De, Tillie B, Barbreau A, Durand E, Feuga B, Peaudecerf P. Modeling fracture flow with a stochastic discrete fracture network: calibration and validation, 1. The flow model. *Water Resources Research.* 1990; 26 (3), 479-489

[11] Chadwick W L. Failure of Teton Dam. 1976

[12] Chang Z X, Zhao Y Sh, Hu Y Q, Yang D. Theoretic and experimental studies on

seepage law of single fracture under 3D stresses. *Chinese Journal of Rock Mechanics and Engineering.* 2004; 23(4):620-624

[13] Chen P, Zhang Y T. Coupling Analysis of Seepage/Stress for Jointed Rock. *Chinese Journal of Rock Mechanics and Engineering.* 1994; 13(4):299-308

[14] Chen Sh H, Egger P, Migliazza R, Giani G P. Three dimensional composite element modeling of hollow bolt in rock masses. In: Proceedings of ISRM Int. Symp. On Rock Eng. For Mountainous Regions-Eurock'2002, Madeira, Portugal, 2002

[15] Chen Sh H, Feng X M. Composite element model for rock mass seepage flow. *J. of Hydrodynamics (Ser. B).* 2006;18(2):219-224

[16] Chen Sh H, Feng X M, Shahrour I. Numerical estimation of REV and permeability tensor for fractured rock masses by composite element method. *International Journal for Numerical and Analytical Methods in Geomechanics.* 2008;32:1459-1477

[17] Chen Sh H, Qiang Sh. Composite element model for discontinuous rock masses. *International Journal of Rock Mechanics and Mining Sciences. & Geomech. Abstr*. 2004;41(7):865-870

[18] Chen Sh H, Qiang Sh, Chen Sh F. Study on the three-dimensional composite element model of bolted rock masses. *Chinese Journal of Rock Mechanics and Engineering*. 2003; 22(1):1-8

[19] Chen Sh H, Qiang Sh, Chen Sh F, Egger P. Composite element model of the fully grouted rock bolt. *Rock Mechanics and Rock Engineering*. 2004;37(3):193-212

[20] Chen Sh H, Qiang Sh, Shahrour I, Egger P. Composite element analysis of gravity dam on a complicated rock foundation. *ASCE International Journal of Geomechanics, 2008 (Science direct on line)*

[21] Chen Sh H, Shahrour I. Composite element method for the bolted discontinuous rock masses and its application. *International Journal of Rock Mechanics and Mining Sciences, 2008 (Science direct on line)*

[22] Chen Sh H, Xu Q, Hu J. Composite element method for seepage analysis of geo-technical structures with drainage hole array. *Journal of Hydrodynamics (Ser. B).* 2004; 16(3):260－266

[23] Chen Sh H, Wang H R, Xiong W L. Study of the Seepage Characteristics of Joint Surface. *Journal of Wuhan University of Hydraulic and Electric Engineering.* 1989, 22(1):53- 60

[24] Chen Z, Narayan S P, Yang Z, Rahma S S. An experimental investigation of hydraulic

behaviour of fractures and joints in granitic rock. *International Journal of Rock Mechanics and Mining Sciences*. 2000;1061-1071

[25] Cooley R L. Incorporation of prior information on parameters into nonlinear regression groundwater flow models.1. Theory. *Water Resources Research*. 1982; 18 (4), 956-976

[26] Cooley R L. Incorporation of prior information on parameters into nonlinear regression groundwater flow models.2. Applications. *Water Resources Research*. 1983; 19 (3), 662-676

[27] Cooley R L. A comparison of several methods of solving nonlinear regression groundwater flow problems. *Water Resources Research*. 1985; 21 (10), 1525-1538

[28] Dershowitz W S, et al. A New Three-dimensional Model for Flow in Fractured Rock. Mem. *Int. Assoc.Hydrogelo*. 1985;17:28-32

[29] Dershowitz W S, Einstein H H. Three dimensional flow modeling in jointed rock masses. *In: Proc. 6th Int. Cong, ISRM*, 1987, 87-92

[30] Desai C S. Finite element residual schemes for unconfined flow. *International Journal for Numerical Methods in Engineering*. 1976;10(6): 1415-1418

[31] Du Y L, Xu G A, Huang Y H. The study of three-dimensional seepage analysis for the complex rock foundation. *Journal of Hydraulic Engineering*. 1984; (3):1-9

[32] Du Y L, Xu G A, Han L B. Study on applicability of three dimensional method for analysis of seepage in complex rock foundation. *Water Resources and Hydropower Engineering*.1991; (1):2-9

[33] Duiguid J O, Lee P C Y. Flow in Fractured Porous Medin. *Water Resource Research.* 1977;13(3):25-28

[34] Esaki T, Du S, Mitani Y, et al. Development of a shear-flow test apparatus and determination of coupled properties for a single rock joint. *International Journal of Rock Mechanics and Mining Sciences*. 1999; 36(5):641-650

[35] Esaki T, Hojo H, Kimura T, Kameda N. Shear-flow coupling test on rock joints. *In: Proc. 7th Int. Cong. ISRM*. 1992;389-392

[36] Feng X M, Chen S H. Preliminary research on composite element method for seepage problems in discontinuous rock masses. *Chinese Journal of Rock Mechanics and Engineering*. 2006; 25(1):93-99

[37] Feng X M, Chen S H. Composite element method for seepage characteristics study on rock masses with complicated fracture network. *Chinese Journal of Rock Mechanics*

and Engineering. 2006; 25(5):918-924

[38] Fipps G, Skaggs RW, Nieber JL. Drains as a boundary condition in finite elements. *Water Resources Research*. 1986;22(11), 1613-1621

[39] Gale J E. The effects of fracture type (Induced VS. Natural) on the stress-fracture closure permeability relationships. *In: Proc. 23th Symp. On Rock Mech.*, Berkeley, California, 1982

[40] Gale J. Hydraulic behaviour of rock joints. In: Barton N, Stephansson O, editors. *Proc Int Symp Rock Joints*. Rotterdam: Balkema; 1990:351-62

[41] Geng K Q. Research and application of the mechanic-percolating interaction of complex rock head [Ph. D. Thesis]. Beijing:Tsinghua University. 1994

[42] Geng K Q, Chen F X, Liu G Y, Chen X H. Experimental Research of Hydraulic Properties of Seepage Flow in Fracture. *Journal of Tsinghua University (Sci & Tech)*. 1996;36(1):102-106

[43] Goodman R E, Taylor R, Brekke T L. A model for the mechanics of jointed rock. *ASCE Journal of the Soil Mechanics and Foundation Division.* 1968;14：637-659

[44] Guan J H, Liu J X, Zhu Y X. Finite element analysis for an array of wells replaced by a drainage ditch. *Journal of Hydraulic Engineering*. 1984 ;(3):10-18

[45] Gureghian A B, Young E C. The calcultion of steady state water heights in drained soils by means of finite element method. *Journal of Hydrology*. 1975; 27(1):15-32

[46] Guvanasen V, Chan T. A three-dimensional numerical model for thermo- hydro-mechanical deformation with hysteresis in a fractured rock mass. *International Journal of Rock Mechanics and Mining Sciences*. 2000:89-106

[47] Hendron A J, Patton F D. The Vajont slide. US Corps of Engineering Report GL85-8. 1985

[48] Hsieh P A, Neuman S P. Field determination of the three dimensional hydraulic conductivity tensor of anisotropic media.1.Theory. *Water Resources Research*. 1985;21(11): 1655-1665

[49] Hsieh P A, Neuman S P, Simpson E S. Pressure testing of fractured rocks-A methodology employing three dimensional cross-hole tests. *In: Top. Rep. NUREG/CR-3213, U. S. Nucl. Regul. Comm*. Washington, D. C. 1983

[50] Hsieh P A, Neuman S P, Stiles G K, Simpson E S. Field determination of the three dimensional hydraulic conductivity tensor of anisotropic media. 2. methodology and application to fractured rocks. *Water Resources Research*. 1985;21(11): 1667-1676

[51] Hu J, Chen S H. Air element method for modeling the drainage hole in seepage analysis. *Rock and Soil Mechanics*. 2003;24(2):281-287

[52] Iwano M, Einstein H H. Laboratory experiments on geometric and hydro- mechanical characteristic of three different fractures in granodiorite. *In: Proceedings of the 8th int. cong. on rock mechanism* Tokyo, Japan, 1995:743-750

[53] Jaeger C. Rock Mechanics and Engineering. 2nd Edition. Cambridge University Press, 1979

[54] Koyama T, Fardin N, Jing L, Stephansson O. Numerical simulation of shear-induced flow anisotropy and scale-dependent aperture and transmissivity evolution of rock fracture replicas. *International Journal of Rock Mechanics and Mining Sciences*. 2006;89- 106

[55] Lee HS, Cho TF. Hydraulic characteristics of rough fractures in linear flow under normal and shear load. *Rock Mechanics and Rock Engineering*. 2002;35:299-318

[56] Li B, Jiang Y J, Koyama T, etc. Experimental study of the hydro-mechanical behavior of rock joints using a parallel-plate model containing contact areas and artificial fractures. *International Journal of Rock Mechanics and Mining Sciences*. 2007:1-14

[57] Liu C H, Chen C X, Fu Sh L. Testing study on seepage characteristic of a single rock fracture under two-dimensional stresses. *Chinese Journal of Rock Mechanics and Engineering.* 2002;21(8):1194-1198

[58] Liu C H, Chen C X, Fu Sh L. Testing study on seepage characteristics of single fracture with sand under shearing displacement. *Chinese Journal of Rock Mechanics and Engineering.* 2002;21(10):1457-1461

[59] Liu J S. The Seepage Formulations in a Single Fracture under Normal Stress. *Hydrogeology and Engineering Geology.* 1987;14(2):32-33

[60] Liu J S. The coupled relationship between mechanical and hydraulic parameters of a structural surface and their applications. *Hydrogeology and Engineering Geology.* 1988; 15(2):7-12

[61] Londe P. The Malpasset dam failure. *Engineering Geology*. 1987 (24):295-329

[62] Long J C S, Remer J S, Wilson C R, Witherspoon P A. Porous media equivalents for networks of discontinuous fractures. *Water Resources Research*. 1982;18(3): 645-658

[63] Long J C S, Gilmour P, Witherspoon P A. A Method for Steady Fluid Flow in Random Three-dimensional Networks of Dice-shanped fractures. *Water Resources Research.* 1985,21(8):35-40

[64] Louis C. Rock Hydraulics. In: Rock Mechanics. Edited by Muller L. New York: Verlay Wien, 1974, 299-387

[65] Louis C, Maini T. Determination of in situ hydraulic parameters in jointed rock. *In: Proc. 2nd Cong. ISRM*. 1970;235-245

[66] Makurat A, Barton N, Rad N S, Bandis S. Joint conductivity variation due to normal and shear deformation. In: Barton N, Stephansson O, editors. *Proc Int Symp Rock Joints*. Rotterdam: Balkema; 1990:535-540

[67] Malama B, Kulatilake P.H.S.W. Models for normal fracture deformation under compressive loading. *International Journal of Rock Mechanics and Mining Sciences*. 2003;893- 901

[68] Mao Ch X, Chen P, Li Z Y, Li D F. Study on Computation Methods of Seepage Flow in Fractured Rock Masses. *Chinese Jounal of Geotechnical Engineering*. 1991; 13(6):1-10

[69] Matsuki K, Kimura Y, Sakaguchi K, Kizaki A, Giwelli A A. Effect of shear displacement on the hydraulic conductivity of a fracture. *International Journal of Rock Mechanics & Mining Sciences*. 2009

[70] Mitani Y, Esaki T, Sharifzadeh M, Vallier F. Shear-flow coupling properties of a rock joint and its modeling by Geographic Information System (GIS). *In: Proc. of the 10th int. cong. on rock mechanics*, Johannesburg, South Africa, 2003:829-32

[71] Oda M. Permeability tensor for discontinuous rock masses. *Geotechnique*. 1985; 35(4): 483-495

[72] Oda M. An equivalent continuum model for coupled stress and fluid analysis in jointed rock masses. *Water Resources Research*. 1986; 22(13): 1845-1856

[73] Olsson R, Barton N. An improved model for hydromechanical coupling during shearing of rock joints. *International Journal of Rock Mechanics and Mining Sciences*. 2001;38(3):317-329

[74] Olsson W A, Brown S R. Hydraulic response of a fracture undergoing compression and shear. *International Journal of Rock Mechanics and Mining Sciences and Geomechanics Abstracts*. 1993;30:845-51

[75] Qiang S, Chen S H. Three-dimensional elasto-viscoplastic composite element model of discontinuous rock masses. *Chinese Journal of Rock Mechanics and Engineering*.

2004;23(20):3390-3396

[76] Raven K G, Gale J E. Water flow in a natural rock fracture as a function of stress and sample size. *International Journal of Rock Mechanics and Mining Sciences and Geomechanics Abstracts.* 1985, 22(4): 251-261

[77] Ru N H, Jiang Zh Sh. Arch dams. Accident and safety of large dams. Beijing: China Water Power Press, 1995

[78] Seed H B, Duncan J. M. The failure of Teton Dam. Engineering Geology. 1987(24): 173-205

[79] Snow D. Rock-fracture spacing, openings and porosities. *Journal of the Soil Mechanics and Foundations Division. ASCE*. 1968;94:73-91

[80] Snow D. Anisotropic permeability of fractured media. *Water Resources Research.* 1969; 5(6):1273-1289

[81] Streltsova T D. Hydrodynamics of Groundwater Flow in a Fractured Formation. *Water Resources Research*. 1976; 12(3): 405-414

[82] Schwartz F W, Smith W L, Crowe AS. A stochastic analysis of microscopic dispersion in fractured media. *Water Resources Research*. 1983; 19(5): 1253-1265

[83] Su B Y, Zhan M L, Wang Y. Experimental research of seepage and stress coupling characteristic for fracture. *Chinese journal of geotechnical engineering.* 1997; 19(4):73-77

[84] Sun N Zh. Numerical model and numerical method for groundwater. Beijing: Science Press,1981

[85] Tao Zh Y, Shen X Y. The coupled analysis of the reservoir stress field. *Journal of Wuhan University of Hydraulic and Electric Engineering.* 1988(1):8-14

[86] Teufel L W. Permeability changes during shear deformation of fracture rock. *In: Proc. 28th US Symp. Rock Mechanics*. 1987;473-480

[87] Tian K M. Hydraulic properties of crossing-flow in an intersected fracture. *Proc. of the 2nd Asian Congress of Fluid Mechanics*. 1984, 571-576

[88] Tsang Y W, Witherspoon P A. Hydromechanical behavior of a deformable rock fracture subject to normal stress. *Journal of Geophysical Research*. 1981, 86(B10): 9287-9298

[89] Tsang C F. Coupled behavior of rock joints. In: Rock joints, Edited by Barton & Stephansson, Balkema, 1990:505-518

[90] Wang L, Liu Z, Zhang YT. Analysis of seepage field near a drainage holes curtain.

Chinese Journal of Hydraulic Engineering. 1992;(4):15-20

[91] Wang E Zh, Yang Ch T. Numerical model of groundwater flow in fracture networks and water flow in disconnected fracture networks. *Hydrogeology and Engineering Geology*. 1992; 19(1):12-14

[92] Wang E Z, Wang H T, Deng X D. "Pipe to represent hole"---numerical method for simulating single drainage hole in rock masses. *Chinese Journal of Rock Mechanics and Engineering*. 2001;20(3),346-349

[93] Wang J S Y. Flow and transport in fractured rocks. *Reviews of Geophysics*. 1991, Supp. 254-262

[94] Wang Y. Coupling Characteristic of Stress and Fluid Flow within a Single Fracture. *Chinese Journal of Rock Mechanics and Engineering*. 2002;21(1):83-87

[95] Wang Y, Xu Zh Y, Su B Y. Four freedom complete method for the seepage stress coupled analysis in fissured rock masses. *Journal of Hydraulic Engineering.* 1998; (7):55-59

[96] Wang Y, Xu Zh Y, Su B Y. Complete Coupled Analysis of Fluid Flow and Elastoplastic Stress in Complicated Fracture Rock Masses. *Chinese Journal of Rock Mechanics and Engineering*. 2000;19(2):177-181

[97] Wittke W, Leonhards G A. Modified hypothesis for failure of Malpasset Dam. *Engineering Geology.* 1987;(24):367-394

[98] Wu Y Q, Zhang Zh Y. An Introduction to Rock Mass Hydraulics. Chengdu: Southwest Jiaotong University Press. 1995

[99] Wu Y Q, Zhang Zh Y. An application of generalized double porosity media model for coupled stress and ground water flow analysis in fractured rock mass. *Journal of Engineering Geology*. 1996; 4(3):40-46

[100] Wu Y Q, Zhang Zh Y. Double porosity media model of coupled ground water flow and stress in fractured rock mass. *Hydrogeology and Engineering Geology*. 1998; 25(1):43-46

[101] Yeo I W, De Freitas M H, Zimmerman R W. Effect of shear displacement on the aperture and permeability of rock. *International Journal of Rock Mechanics and Mining Sciences*. 1998;35:1051-1070

[102] Zhu B F. The analysis of the effect of drainage holes in the seepage field by means of hybrid elements. *Journal of Hydraulic Engineering.* 1982; (9):32-41

[103] Zhang Y T. Calculate the seepage field with drainage holes by boundary element

method. *Journal of Hydraulic Engineering*. 1982; (7):36-40

[104] Zhang Y T. Rock hydraulics and engineering. Beijing: China Water Power Press, 2005

[105] Zhang Y Zh, Zhang J C. Experimental study of the seepage flow-stress coupling in fractured rock masses. *Rock and Soil Mechanics*. 1997;18(4):59-62

[106] Zhang Y T, Zhang W G.. Permeability characteristics, numerical model and parameters test for fractured rock mass. *Rock Mechanics*. 1982(8):41-52

[107] Zienkiewicz O C. The finite element method third edition. McGraw-Hill, Inc., 1977

[108] Zienkiewicz O C, Mayer P, Cheung Y K. Solution of anisotropic seepage by finite elements. *Journal of the Engineering Mechanics Division*. *ASCE*. 1966;92, 111-120

[109] Zimmerman R W, Hadgu T, Bodvarsson G S. A new lumped-parameter model for flow in unsaturated dual-porosity media. *Advances in Water Resources*. 1996; 19(5): 317-327